For Reference

NOT TO BE TAKEN FROM THIS ROOM

Ex libris
Universitatis
Albertaensis

QUAECUMQUE VERA

BRUCE PEEL SPECIAL COLLECTIONS LIBRARY
UNIVERSITY OF ALBERTA LIBRARY

REQUEST FOR DUPLICATION

I wish a photocopy of the thesis by

Zehari, A. (author)

entitled A β-particle Detector for the study—

The copy is for the sole purpose of private scholarly or scientific study and research. I will not reproduce, sell or distribute the copy I request, and I will not copy any substantial part of it in my own work without permission of the copyright owner. I understand that the Library performs the service of copying at my request, and I assume all copyright responsibility for the item requested.

Digitized by the Internet Archive
in 2021 with funding from
University of Alberta Libraries

https://archive.org/details/Zenari1978

THE UNIVERSITY OF ALBERTA

RELEASE FORM

NAME OF AUTHOR ADRIANO ZENARI

TITLE OF THESIS A β-PARTICLE DETECTOR FOR THE STUDY OF AXOPLASMIC TRANSPORT

DEGREE FOR WHICH THESIS WAS PRESENTED MASTER OF SCIENCE

YEAR THIS DEGREE GRANTED 1978

Permission is hereby granted to THE UNIVERSITY OF ALBERTA LIBRARY to reproduce single copies of this thesis and to lend or sell such copies for private, scholarly or scientific research purposes only.

The author reserves other publication rights, and neither the thesis nor extensive extracts from it may be printed or otherwise reproduced without the author's written permission.

THE UNIVERSITY OF ALBERTA

A β-PARTICLE DETECTOR FOR THE STUDY OF AXOPLASMIC TRANSPORT

by

© ADRIANO ZENARI

A THESIS

SUBMITTED TO THE FACULTY OF GRADUATE STUDIES AND RESEARCH
IN PARTIAL FULFILMENT OF THE REQUIREMENTS FOR THE DEGREE
OF MASTER OF SCIENCE
IN
PHYSICS

DEPARTMENT OF PHYSICS

EDMONTON, ALBERTA
SPRING, 1978

THE UNIVERSITY OF ALBERTA

FACULTY OF GRADUATE STUDIES AND RESEARCH

The undersigned certify that they have read, and recommend to the Faculty of Graduate Studies and Research, for acceptance, a thesis entitled A β-PARTICLE DETECTOR FOR THE STUDY OF AXOPLASMIC TRANSPORT

submitted by ADRIANO ZENARI

in partial fulfilment of the requirements for the degree of MASTER OF SCIENCE IN PHYSICS.

To my Mother and Father

ABSTRACT

The design and construction of a position sensitive detector, specifically for use in physiological studies, are detailed. Such a detector composed of a row of rectangular proportional counters, is constructed for studies of the movement of β-labelled material along nerve axons. The principle of operation of proportional counters, in general, is reviewed.

It is shown that it is possible to optimize operating characteristics of a small counter with respect to its dimensions. Details of a 16-channel prototype multiwire chamber are included, together with the circuitry employed in the read-out.

The application of a multiwire proportional chamber to axoplasmic transport studies is discussed. Results of this are compared to those obtained from similar studies using liquid scintillation counting techniques. It is demonstrated that the system is readily applicable in thin layer chromatography.

ACKNOWLEDGEMENTS

I extend grateful thanks to a number of people who assisted and helped me in this work.

First I would like to thank my supervisor Dr. R. E. Snyder, for the many hours of review, conversation and suggestions both during the experimental work and in preparation of this thesis. I am also grateful to Dr. D. Menon for the time he devoted to me in discussion and reviewing the manuscript.

A particular thanks to Mr. R. A. Reynolds who helped me to understand many different aspects of the counter operation. I wish to forward my appreciation to Dr. G. Blinston for many stimulating discussion about electronics and to Mr. N. Ouellette for constructing the interface to the Ortec 6240 multichannel analyser. I am indebted also to Mr. I. Yamamoto for his precise machine work in constructing the multiple counter.

A final thanks to Mrs. S. Elliott for the prompt and excellent work in typing and formatting this thesis for computer.

TABLE OF CONTENTS

CHAPTER	PAGE
1 INTRODUCTION	1
1.1 Introduction	1
1.2 Radioisotope tracers in axoplasmic transport	1
1.3 An alternative technique for the study of axoplasmic transport	4
2 PROPORTIONAL COUNTER	10
2.1 Gas filled detectors	10
2.2.1 Proportional counter: Introduction	14
2.2.2 Operation	17
2.3 Parameters affecting the counter operation	28
3 SINGLE COUNTER DESIGN	37
3.1 General consideration	37
3.2 Centred anode:single counter design	37
3.2.1 Detection efficiency to -rays	39
3.3 Electrostatics of the counter	47
3.4 Off-set anode: single counter	53
3.5 Background	56
3.6 Gas amplification	58
3.7 Discussion	65
4 MULTIPLE DETECTOR	66
4.1 Description of the system	66
4.2 Counter construction	67
4.2.1 Fin characteristics	72
4.2.2 Gas flow	73

4.3 Read-out system 79
4.3.1 The amplifier 80
4.3.2 Encoding 83
4.3.3 Data collection 85
5 RESULTS AND DISCUSSION 87
5.1 Experimental results 87
5.2 Discussion 91
BIBLIOGRAPHY 94
APPENDIX A 99
A.1 Introduction 99
A.2 Method 99
A.3 Results 103
A.4 Program "MAT" 106

LIST OF TABLES

Table	Description	Page
TABLE I	Range of common β-emitters in different metals	74

LIST OF FIGURES

Figure		Page
1.1	Simple rapresentation for the fast transport system of the site of synthesis of proteins in nerve soma and their transfer into the axon	3
1.2	Exploded view of multiwire proportional chamber with ancillary electronics	6
2.1	Operation characteristic of gas filled detectors	12
2.2	Coaxial cylindrical counter:a) cross section b) anode pulse shape	18
2.3	Differentiating network	25
3.1	High voltage network	38
3.2	Detection efficiency of ^{14}C for a 4 mm wide counter	42
3.3	Detection efficiency of ^{14}C for a 3 mm wide counter	43
3.4	Detection efficiency of ^{14}C across the counter window for a 4 mm wide counter	45
3.5	Detection efficiency for a 3 mm wide and 6 mm deep counter in the longitudinal direction	45
3.6	Square counter with central anode	49
3.7	Rectangular counter with central anode and 2:1 lenth:width ratio	49
3.8	Rectangular counter with central anode and 4:1 lenth:width ratio	51
3.9	Rectangular counter with off-set anode	52
3.10	Rectangular counter with off-set anode and 4:1 lenth:width ratio	54
3.11	Detection efficiency of ^{14}C for a 3 mm by 20 mm counter with off-set anode	55
3.12	Detection efficiency of ^{14}C across the counter window	57

LIST OF FIGURES continued

3.13 Typical ^{14}C β-spectrum 57

3.14 Background spectrum for a 3 mm by 20 mm counter 59

3.15 Gas amplification for a) 3 mm and b) 4 mm wide counters 63

3.16 Gas amplification for 6 mm deep counters 64

4.1 Multiple detector:interior planes 68

4.2 Multiple detector: metallic frame 70

4.3 High voltage network for the multiple detector 71

4.4 Dependence of count rate with rate of gas flow 76

4.5 Longitudinal variation in count rate 78

4.6 Response of the 16 counters to a ^{14}C source 78

4.7 Amplifier, trigger and memory 82

4.8 Encoder with strobe, reset and start memory signals 84

4.9 Timing sequence of events 84

5.1 Activity distribution obtained with a) β-detector, b) liquid scintillation counter 89

5.2 Activity distribution in the chromatographic strip 92

A.1 Rectangular counter with anode at (α,β) 102

A.2 Square counter 104

A.3 Rectangular counter. 105

CHAPTER 1

INTRODUCTION

1.1 Introduction

The development and rapid expansion of nuclear reactors in recent years has made available a large number of radioactive isotopes which are regularly used in many branches of science, either as tracers or as sources of radiation. The tracer application is by far the more important and is possible because the chemical properties of the radioactive isotopes are identical to their stable counterparts. One important use of radioactive tracers is as radiopharmaceuticals which find wide application in medicine and other sciences. In medicine, for instance, they are employed to trace metabolic processes, yielding the amount of labelled substances present and the rates at which these radiolabelled compounds enter and leave the various compartments of the body. Another aspect of the isotope tracer technique, of particular interest to this work, is its application to physiological studies. Our specific interest is in the study of the movement of material along nerve fibers, known as axoplasmic transport.

1.2 Radioisotope tracers in axoplasmic transport

One active area of research in the neurological sciences is involved with examining the mechanisms associated with the delivery of essential material (e.g.

proteins) to the axon. It is generally accepted that the bulk of protein synthesis takes place in the nerve cell body (soma), after which the proteins are transported down the axon (see Fig. 1.1). Initially, the study of transport phenomenon was performed by damming the nerve, for example, by constriction and observing the accumulation of axoplasm proximal to the site of constriction[1] . Definite proof that proteins were synthesized in the cell body and then transported into the axon was obtained by Droz and LeBlond[2]. Their experiments, performed using [^{3}H]-Leucine, constituted one of the earliest applications of a labelled organic compound to the study of axoplasmic transport. To date, the radioactive isotopes used include ^{3}H, ^{14}C, ^{35}S, ^{45}Ca and ^{32}P. The radioisotope tracer technique is now widely applied to the detection of both the fast and slow transport systems (see below). Detailed descriptions have been given by Lubinska[3] and Lasek[4].

Measurements of the movement of radioactivity along nerves have produced estimates of the velocity of transport. For the fast component, which is of specific interest to us, the velocity varies from 100 to 2000 mm/day. The slow component is limited to a few mm/day. The large variation in the fast transport rate may be due in part to the different nerve species analyzed and to the methods used to determine the transport velocity.

A typical experimental procedure using radiolabelled proteins involves injecting or incubating the nerve cell

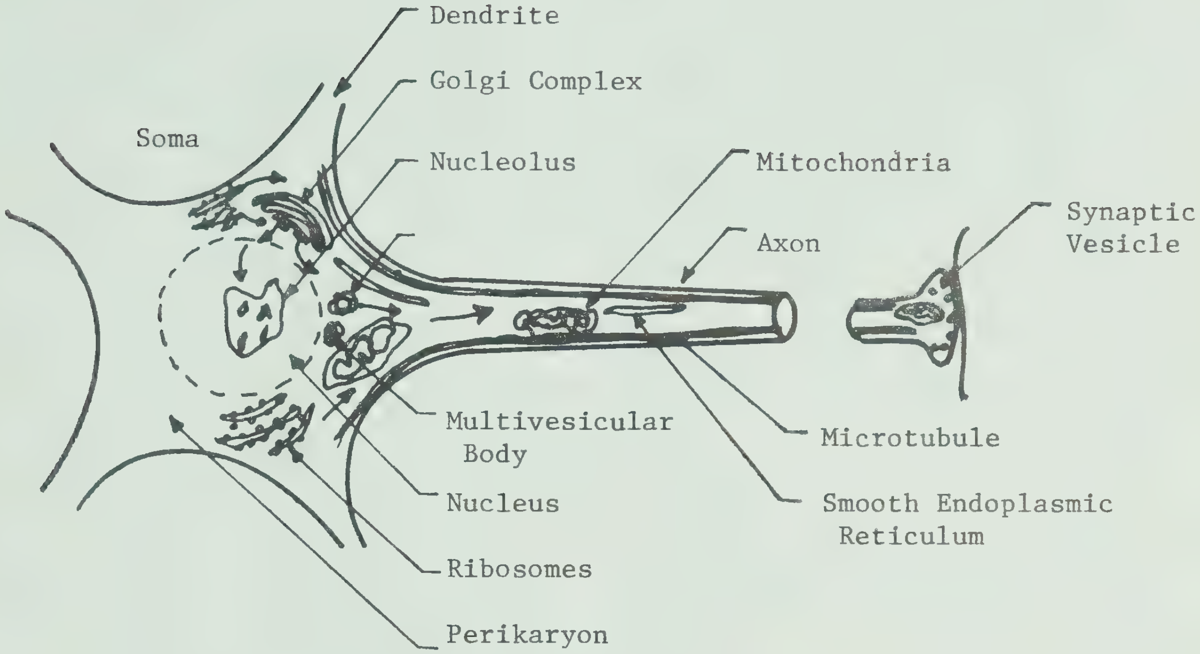

FIG. 1.1 Simple representation for the fast transport system of the site of synthesis of proteins in the nerve soma and their transfer into the axon. Protein synthesis occurs primarily in the ribosomes of the perikarion. The protein produced in the ribosomes is transferred into the Golgi complex which loads the protein into the fast transport system. The various proteins either travel to the nerve endings or are deposited along the axon. (After Droz and Koenig, Protein Metabolism of the Nervous System 1970. Edited by A. Lajtha)

bodies with a radiolabelled amino acid precursor[5-7]. The amino acid may be administered either prior to or after isolation of the nerve preparation. Following the treatment, lasting for a predetermined period of time, the distribution of the radioactive protein within the nerve is determined. The longer the incubation period, the further the front of the distribution moves down the nerve fibers. The rate at which the front moves can be determined by locating the front of the activity for various nerve preparations incubated over varying time intervals. The distribution of the radiolabelled material is normally obtained by liquid scintillation counting. Because each preparation yields the distribution of the radiolabelled proteins at one particular time, several nerves and therefore several animals are required. This is in order to obtain a distance-to-time relation. The interpretation of the data rests upon two major assumptions: 1) that axonal transport is linear in time and 2) that all of the preparations are similar, even though the nerves originate from different animals.

1.3 An alternative technique for the study of axoplasmic transport

Recently, a new method of studying the axonal transport of β-labelled material was developed by Snyder *et al.*[8] . The major point of interest arising from their technique is that measurements can be obtained from a nerve preparation during its incubation using a position sensitive detector, viz. a

multiwire proportional chamber (MWPC).

The nerve preparation is placed in a two compartment tray and immersed in a Ringer's solution. In the smaller compartment (Fig. 1.2), the spinal cord, roots and ganglia (of the sciatic nerve of the amphibian Xenopus laevis) are incubated together with a β-labelled amino acid precursor; this compartment is lead shielded. The peripheral nerve, after passing through an aperture in the inner wall, is accommodated in the larger compartment. Following proper placement of the preparation in the tray, the aperture is sealed with silicon grease to prevent leakage of the radioactive material into the axon (large) compartment. The tray is placed on the detector entrance window and the transport of labelled proteins monitored for an extended period of time via the β-particles which escape the nerve and enter the detector.

The basic detector components are shown in Fig. 1.2. They consist of a collimating system (CS), two drift planes (XP and YP), and an anode plane (ZP). The collimator, provided with four equal voltage steps, confines the ionizing particles originating in the nerve to a well defined region in space. The electric drift field produced by the voltage steps causes the secondary electrons liberated between the collimator fins to move towards the anode region where each electron gives rise to an avalanche, which induces a negative pulse on the corresponding Z-plane wire and positive pulses on the X- and Y-plane wires. The

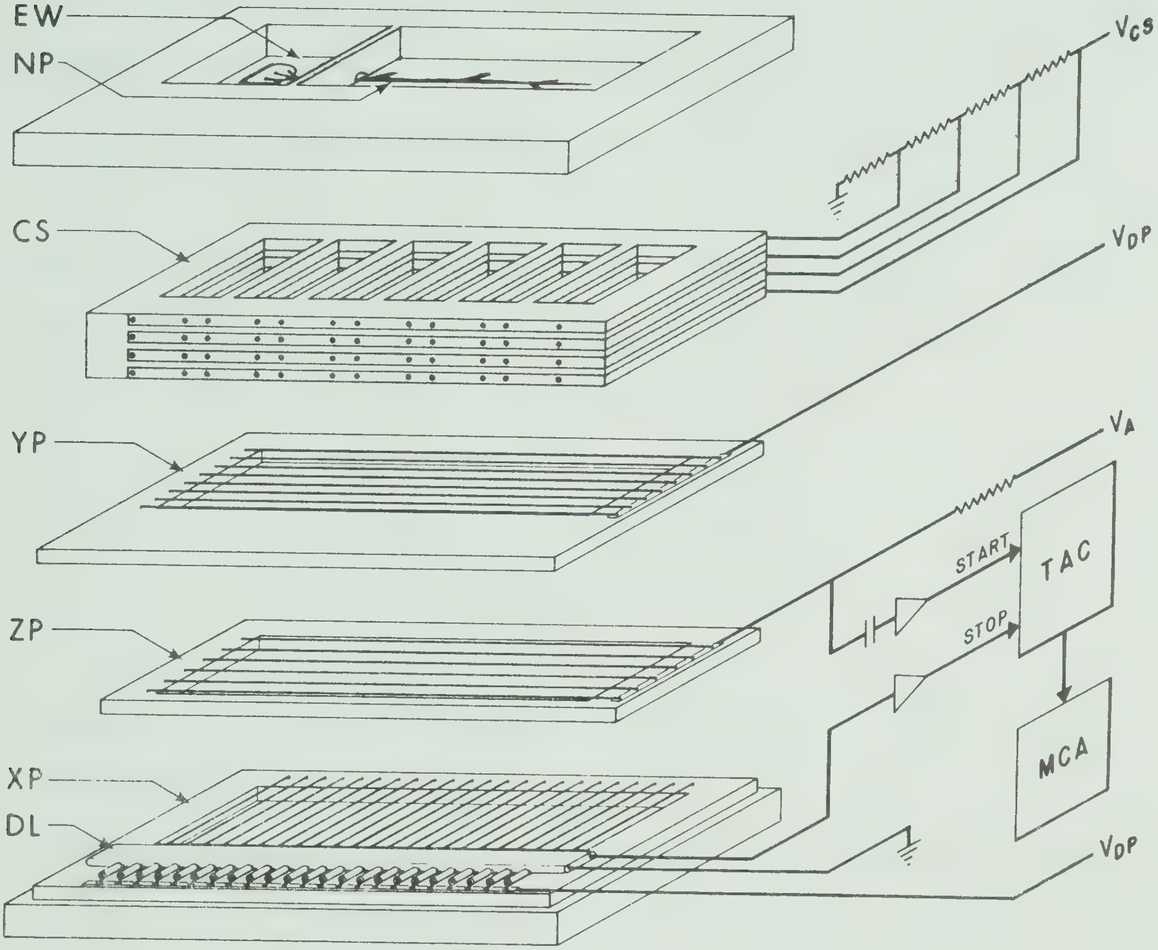

FIG. 1.2 Exploded view of multiwire proportional chamber with ancillary electronics. CS, collimator system; DL, electromagnetic delay line; EW, aluminized mylar entrance window; MCA, multichannel analyser; NP, nerve preparation; TCA, time-to-amplitude converter; V_A, anode potential; V_{DP}, drift plane potential; XP; X-(drift) plane; YP, Y-(drift) plane; ZP, Z-(anode) plane. (From Snyder *et al*.[8]; used with author's permission).

charge pulse collected at the anode wire is differentiated and the voltage pulse so obtained used to start a time-to-amplitude converter (TAC). A summed positive pulse, extracted through an electromagnetic delay line (DL) which is capacitively coupled to wires of the X-plane, is used to produce a TAC stop signal. The delay in arrival of the stop signal provides information about the avalanche location. The system is one dimensional and uses only the X-plane to locate the origin of an event along the nerve. The transport velocity of the labelled protein along the nerve fibers is determined by locating the radioactive front at regular time intervals following administration of the radioisotope.

This new experimental approach to the detection of axonal transport has one obvious advantage over the more established methods described in an earlier section: it yields a distance-time relationship of transport from a single nerve preparation. This procedure reduces errors arising from changes in ambient condition and, more important, it eliminates errors due to physiological differences between animals.

The negative aspects of the detection system just described are associated with the special configuration of the MWPC required by the axoplasmic transport experiments. For example, the need for a collimator, which in the experimental set up described above has a centre-to-centre spacing of 6 mm, reduces considerably the spatial resolution of the detector. An additional disadvantage is the counting

loss due to the thickness of the collimator fins. Snyder et al.[8] had to accept a loss of about 25%. The collimator dimensions could be modified to reduce these adverse effects. There are, however, restrictions on the collimator size due to the efficient drifting action obtainable.

Jeavons et al.[9] observed for a collimator with circular holes that count rate saturation, and therefore efficient drifting action, was achieved when the ratio of the hole diameter to the voltage plate thickness was in the neighbourhood of two. The rectangular collimator used by Snyder et al.[8] had four voltage zones and a total thickness of about 16 mm. This would bring the width to voltage zone ratio to slightly greater than one, resulting in poor collection efficiency of the secondary electrons.

An additional disadvantage of the MWPC system is its background counting rate (15-30 cpm/cm). As reported by the authors, the count rate due to the activity present in the nerve may be of the same order of magnitude as the background, thus necessitating long data collection times which degrade the position-time sensitivity of the system.

The disadvantages just described have been largely responsible for the development of a new β-ray detector for axoplasmic transport studies. The detector we propose here consists of a series of small proportional counters arranged side by side in a linear array. Proportional counters are gas filled devices; their principles of operation and some general aspects of the counter characteristics will be dealt

with in Chapter 2.

In our particular case each individual counter has a rectangular cross section. The dimensions were optimized to achieve high counting efficiency to most β-sources used in axonal transport experiments and to minimize the background counting rate. These and other aspects of the single counter will be presented in Chapter 3.

The final counter arrangement tested consists of sixteen individual counters arranged as a linear array. The read-out system employs one amplifier per wire. This provides an easy and precise method of identifying the nerve region from which ionizing radiation has originated. The read-out system and other features particular to the combined counter will be discussed in Chapter 4.

Chapter 5 will contain some experimental results and general remarks about the advantages of the detector, and also some of its shortcomings.

CHAPTER 2

PROPORTIONAL COUNTER

2.1 Gas filled detectors

The phenomenon of ionization is basic to the detection of various types of radiation. When an ionizing particle traverses a gas, energy is lost to the medium due to ionization or excitation of the gas atoms or molecules. Of interest to us is ionization, which occurs when the energy transferred to the medium is sufficient to produce a positive ion-electron pair. The energy, W, required to create an ion pair for many gases and gas mixtures is in the neighbourhood of 30 eV. Experimental values and methods of measurements of the average energy expended by various ionizing radiations in a gas medium have been summarized in review articles by Valentine and Curran[10], and Whyte[11]. Gas filled detectors respond to the ion pairs liberated in their active volume by producing an electric signal. Ionization chambers measure the number of ion pairs produced per unit time, or alternatively the total charge for a fixed period of time. Proportional and Geiger devices count the number of pulses produced in the counter due to the passage of ionizing radiation.

Gas filled detectors consist, in principle, of two electrodes, separated by a potential difference, in a gas filled volume. Consider the case of an anode wire lying along the axis of a cylindrical cathode which contains the

gas medium[12]. At the lower voltages the magnitude of the potential difference is an important factor in determining the operating characteristic of the counter . The ion pairs resulting from the passage of ionizing radiation can recombine, in which case the molecules will revert to their original electrically neutral state. However, for sufficiently large applied voltages, the positive ions will drift towards the cathode where they are reinstated to their original neutral state, and the electrons will reach the anode causing a current signal to flow in the external circuit through the power supply. The dependence of the number of electrons produced in the medium on the potential difference between the electrodes is demonstrated in Fig. 2.1. As the voltage between the electrodes is increased, the recombination loss decreases until all the pairs produced are collected. At V_1, a small additional increase of the voltage will not affect the collection efficiency. The device has at this stage reached the ionization saturation plateau. This is the region in which ionization chambers are operated. If the voltage is increased beyond V_2, the electrons produced by the ionizing radiation, under the influence of the electric field, acquire enough energy to cause secondary ionization in the region near the anode. This process repeats itself until an avalanche of electrons reaches the positive electrode. In this region, all of the primary electrons will produce an avalanche, giving a charge pulse at the anode which is

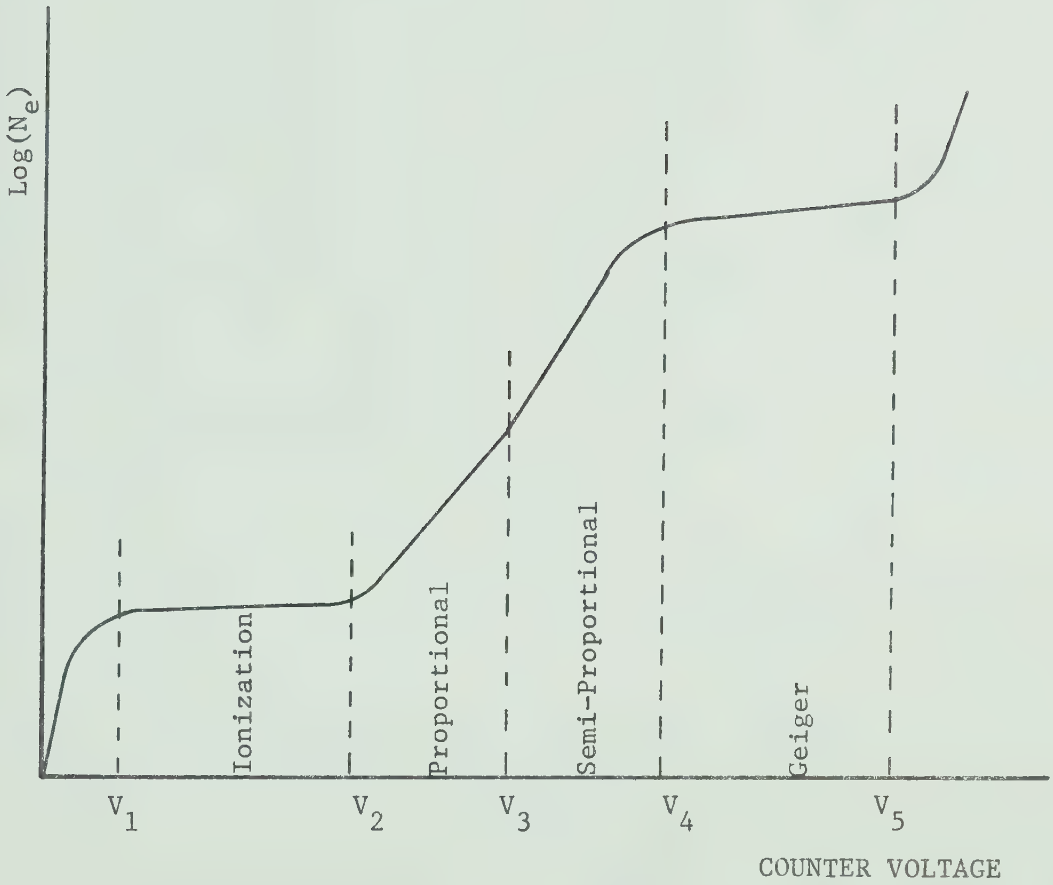

Fig 2.1 Operation characteristic of gas filled detectors.

proportional to the number of avalanches occuring simultaneously. For potential differences greater than V3, the electrons acquire enough energy to cause radiative collisions with the gas atoms or molecules. This produces a continuum of low energy photons which can interact with the medium, liberating new avalanches by photo-ionization. The number of avalanches produced will exceed the number of ion pairs due to the primary ionizing radiation, and proportionality will be lost. At V_4, a single avalanche will breed more avalanches until the entire gas volume along the anode wire becomes ionized. The cloud of positive ions counteracts the potential gradient created by the applied voltage and ultimately stops the avalanche.

Beyond V_4 follows a plateau which is the region of operation of the Geiger-Mueller (G.M.) counter. The pulse size obtained in this plateau does not depend any longer on the initial ionization, but is a function only of the counter characteristics. After the G.M. region (beyond V_5) the counter enters into a continuous discharge region.

From the processes just described, it is evident that differences exist between the various detectors. Ionization chambers, for example, detect the total number of ion pairs produced in the gas volume for any given time. One important feature of such detectors is their ability to distinguish between different types of ionizing radiation. They are frequently used for measurement of radiation dose or dose rate. Proportional and Geiger-Mueller detectors, because

they respond to individual charge pulses, are often referred to as counting devices. However, since the pulse in the proportional region depends upon the number of avalanches simultaneously reaching the anode, the proportional counter discriminates between the different ionizing radiation, as does the ionization chamber.

2.2.1 Proportional counter: Introduction

The proportional counter occupies an intermediate position between the ionization chamber and the Geiger-Mueller counter with respect to principles of operation and construction. It operates in the proportional region of the gas amplification curve. The counter consists of a central electrode (anode) enclosed in a metallic frame of any geometry (cathode). The outer case is usually provided with an end window for the passage of ionizing radiation.

The principles of operation of the proportional counter were first utilized in 1908 by Rutherford and Geiger[13] to detect single α-particles. Geiger and Klemperer (1928)[14], using a ball counter, showed that with a suitably adjusted potential, the initial ionization produced by each particle was magnified linearly by collisions. In addition, they found that the amplification factor increased with increasing potential up to a critical voltage at which point the size of the pulse became independent of the ionizing radiation (Geiger Threshold). Early in its development the

proportional counter was restricted to the detection of highly ionizing particles such as protons and α-particles. The lack of electronics capable of resolving charges corresponding to a few ion pairs made it impossible to utilize proportional counters for the detection of more weakly ionizing forms of radiation (e.g. β and γ).

The development of the modern proportional counter began in the early 1940's and was directed towards the detection of β and γ radiation. This new application required a complete revision of the old proportional counter technology. Certain aspects regarding their operation such as gas mixtures and gas amplification became of increasing importance. The earliest complete theoretical and experimental investigation of the discharge mechanism in proportional counters was reported by Rose and Korff in 1941[15]. Their results were fundamental towards a better understanding of the counter behaviour and the processes associated with gas amplification, and stimulated further research in the field[16-19].

In recent years, the increased demand for proportional counters for special applications has posed stringent requirements on all aspects of the counter technology. Major effort has been directed towards exploiting parameters such as gas mixture, counter geometry and associated electronics, which directly affect counter operations. One innovative aspect of the modern proportional counter is the multiwire proportional counter (MWPC)[20]. Although multianode counters

had been used before, it was customary to separate their active regions by means of one or more shielding wires with a consequent reduction in spatial resolution[21]. It was believed that for closely spaced wires, their capacitative coupling would prevent the localization of an avalanche to a single wire. Charpak et al.[20], in their original paper, showed that for the detector operating in the proportional region, each wire acted as an independent counter.

The traditional cylindrical counter with a central anode is almost exclusively used for studies of gas amplification and phenomena associated with avalanche formation[22-27]. The advantage of using a cylindrical geometry over other configurations for such work is the well understood electrostatic problem. For applications where large sensitive areas are required, the MWPC and others multianode configurations have almost entirely replaced the cylindrical type. Multiwire proportional chambers find application in many areas of intermediate and high energy physics for the detection and localization of charged particles[28-35]. As position sensitive detectors, MWPC's are well suited to applications in the life sciences for the localization of radioactive tracers in biomedical studies[36-39]. Multianode counters are also used in health physics for the detection of low energy γ-rays (< 100 KeV)[40-42], in x-ray astronomy[43], and in radionuclide metrology[44].

2.2.2 Operation

The initial process in a proportional counter is the ion pair formation in the gas volume. For counter operation, the important step is the subsequent movement of the positive ions and electrons towards the oppositely charged electrodes. This movement of charges is of primary importance to the formation and shape of the pulse. The analysis that follows is a précis of the treatment given by Wilkinson[12] for a counter of cylindrical geometry, but is applicable to counters of other configuration.

Consider a cylindrical proportional counter (Fig.2.2a) with the anode and cathode separated by a potential difference. Next, assume the formation of an electron/ion pair within the counter volume. The pulse formed at the anode results from the collective movement of the positive and negative charges in the electric field. Following the formation of an ion pair, the potential induced on the anode at any time t resulting from the induced charges $-q_+(t)$ and $-q_-(t)$, due to the positive ion and electron respectively, is

$$P(t) = \frac{q_+(t) + q_-(t)}{C} \qquad \text{2-2.1a}$$

where c is the counter capacitance. At time t=0 the potential is zero because the positive and negative charge released in near proximity to one another induce on the anode signals of the same magnitude but of opposite

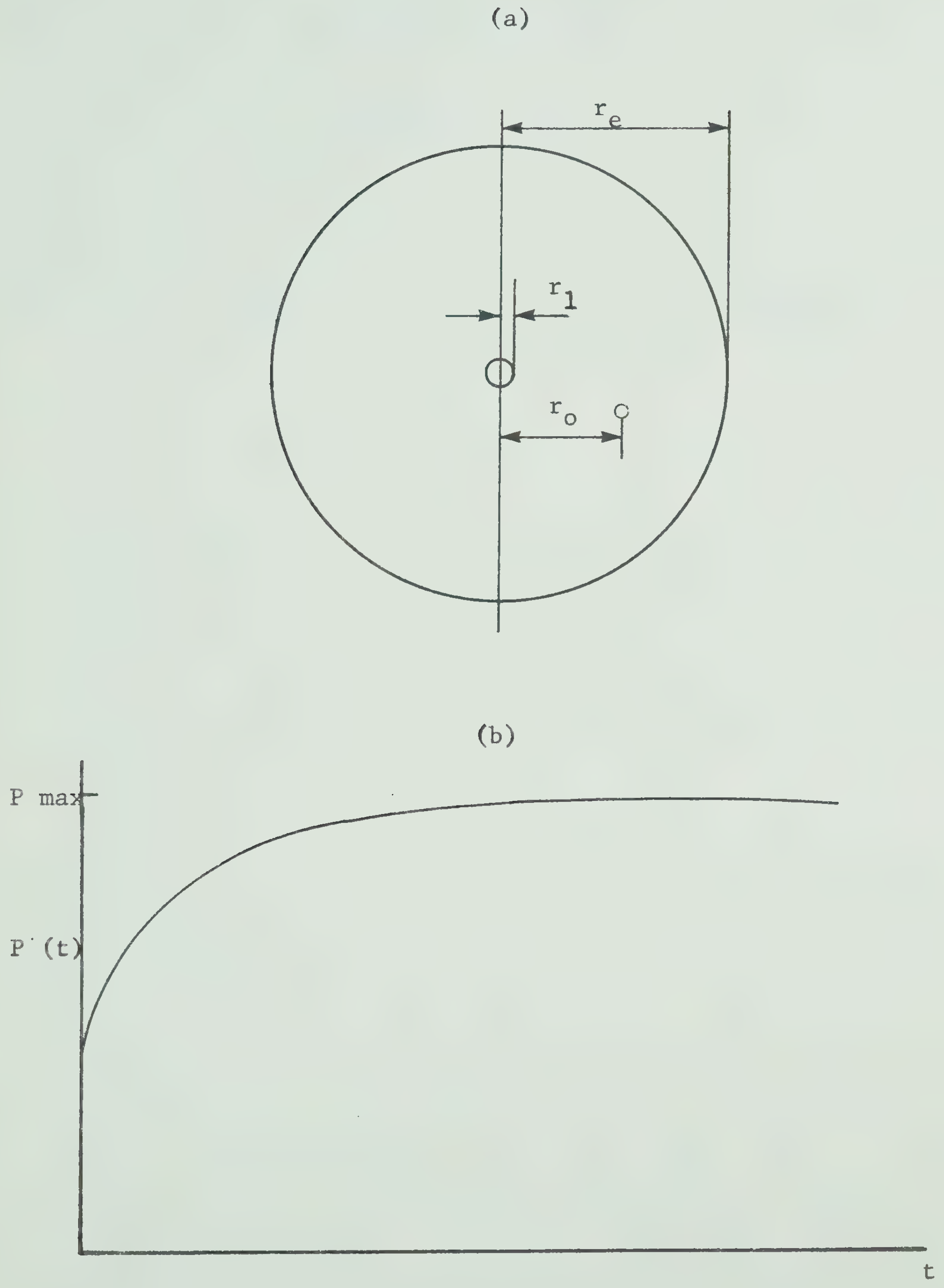

Fig. 2.2 Coaxial cylindrical counter: a) cross section b) anode pulse shape.

polarity. After collection of the electron at time t_1, $q_-(t_1)=-e$ and the potential becomes

$$P(t_1) = \frac{q_+(t_1) - e}{C} \tag{2-2.1b}$$

At a time $t_2 (t_2 >> t\ )$, when the positive ion reaches the cathode, $q_+(t_2) = 0$ and the potential reduces to

$$P(t_2) = \frac{-e}{C} \tag{2-2.1c}$$

In dealing with a large number of ion pairs the problem reduces to determining the induced charges $-q_+(t)$ and $-q_-(t)$ for the particular counter geometry and types of ions. The potential change at the anode results from the contribution of all the induced charges. There are some simplifying assumptions which are made in the derivation of the expression for the potential for the proportional counter. These assumptions are: a) all electrons created in the ionization track are collected at the central wire at the same time, b) all the positive ion-electron pairs are created at the central collecting wire, and c) recombination is negligible. The first assumption is reasonable for low energy electrons but degrades as the energy increases. The second assumption is valid for amplification factors above 10, since the avalanche occurs within a few diameters of the anode wire. The third assumption is valid for strong electric fields.

The calculation of $-q_+(t)$ and $-q_-(t)$ can be performed using Green's reciprocation theorem which states that for an isolated system of n conductors, the potentials P_i due to the corresponding charges q_i can be replaced by a second set of potentials P_i' due to the charges q_i', to yield the equality

$$\sum_{i=1}^{n} q_i P_i' = \sum_{i=1}^{n} q_i' P_i \qquad 2\text{-}2.2$$

We take P_i' and q_i' to be the potentials and charges respectively under normal operating conditions. Let charge e be placed on a very small electrode located between the main counter electrodes so that $q_3 = e$; then q_1 and q_2 are the induced charges to be determined. The corresponding set of potentials are taken to be $P_1 = P_2 = 0$, leaving P_3 unspecified. The second set of potentials P_i' is the one existing during normal operating conditions where $q_3' = 0$ and q_1' and q_2' are unspecified. Applying Green's theorem one obtains

$$q_1 P_1' + q_2 P_2' + eP_3' = 0 \qquad 2\text{-}2.3$$

where $q_1 + q_2 + e = 0$. Hence, solving for q_1 and q_2 it follows that

$$q_1' = -e \frac{(P_3' - P_2')}{(P_1' - P_2')} \qquad 2\text{-}2.4a$$

$$q_2' = -e \frac{(P_1' - P_3')}{(P_1' - P_2')} \qquad 2\text{-}2.4b$$

The induced charges q_1 and q_2 are determined by the potentials under normal operating conditions. In the cylindrical counter indicated in Fig. 2.2a, with a central electrode of radius r_1 and an outer electrode of radius r_2, the potential at the radial position r_o can be obtained from the field relation

$$E = \frac{V}{r_o \ln (r_2/r_1)} \qquad 2\text{-}2.5$$

where V is the applied voltage. If we assume that the electron is collected at t = 0, from equation 2-2.1a

$$P(t) = \frac{-e + q_+(t)}{C} \qquad 2\text{-}2.6$$

Because of the close proximity of the positive ion to the anode at time $t = 0$, $q_+(0) = e$ and $P(0) = 0$. Therefore, the rise time of the pulse is due primarily to the positive ion drifting away from the anode. From Green's theorem

$$q_+ = e \frac{P_3' - P_2'}{P_1' - P_2'} = \frac{e}{V} \int_{r_o}^{r_2} E \, dr \qquad 2\text{-}2.7a$$

hence

$$q_+ = e \frac{\ln(r_2/r_o)}{\ln(r_2/r_1)} \qquad 2\text{-}2.7b$$

Substituting into equation 2-2.6 gives

$$P(t) = \frac{-e + e \dfrac{\ln(r_2/r_o)}{\ln(r_2/r_1)}}{C} \qquad 2\text{-}2.8$$

where r_o is the position of the drifting positive ion at any time t.

In proportional counters operated near atmospheric pressure the drift velocity of the positive ion, u, is given by

$$U = \frac{dr}{dt} = KE = \frac{KV}{r \ln(r_2/r_1)} \qquad 2\text{-}2.9a$$

where K is the positive ion mobility. Thus, from

$$\int_{r_1}^{r_o} rdr = \int_{o}^{t} \frac{KV}{\ln(r_2/r_1)} dt, \qquad 2\text{-}2.9b$$

integrating and solving for r_o, one obtains

$$r_o = \sqrt{r_1^2 + \frac{2KV}{2 \ln(r_2/r_1)} t} \quad . \qquad 2\text{-}2.10$$

Substituting r_o in expression 2-2.8 yields

$$P(t) = \frac{e}{C}\left\{\frac{\ln\left[r_2\Big/\sqrt{r_1^2 + \frac{2KV}{\ln(r_2/r_1)}\,t}\,\right]}{\ln\,(r_2/r_1)} - 1\right\} \qquad \text{2-2.11a}$$

which reduces to

$$P(t) = -\frac{e}{C}\left\{\frac{\ln\left(1 + \frac{2KV}{r_1^2\ln(r_2/r_1)}\,t\right)}{2\ln\,(r_2/r_1)}\right\}. \qquad \text{2-2.11b}$$

At time t_2 the positive ion reaches the cathode and the potential becomes $P(t_2) = -(e/C)$. From equation 2-2.11b one can obtain the collection time t_2, namely

$$t_2 = \frac{\ln(r_2/r_1)}{2KV}\,(r_2^2 - r_1^2). \qquad \text{2-2.12}$$

If we let

$$t_o = \frac{r_1^2}{r_2^2 - r_1^2}\,t_2\ ,$$

P(t) reduces to

$$P(t) = -\frac{e}{C}\;\frac{\ln(1 + \frac{t}{t_o})}{2\ln(r_2/r_1)}\ . \qquad \text{2-2.13}$$

Fig. 2-2b shows the typical anode pulse obtained in a cylindrical counter.

The number of ion pairs produced in the avalanche, N, is

$$N = \frac{E}{W} \cdot M \qquad 2\text{-}2.14$$

where E is the energy of the primary radiation, W the energy required to produce an ion pair and M the gas amplification factor. The expression for the potential thus takes the form

$$P(t) = \frac{(E/W)\ M\ e}{C} \cdot \frac{\ln(1 + \frac{t}{t_o})}{2\ \ln(r_2/r_1)} \qquad 2\text{-}2.15$$

The fast rise time of the pulse obtained in a proportional counter is usually exploited by passing the signal through an RC differentiating network, thereby reducing the pulse length. To analyze the effect of the differentiating network, it is convenient to convert P(t) to its normalized form, namely

$$P(\tau) = \frac{1}{2\ \ln(r_2/r_1)} \ \ln\left(\frac{r_2^2}{r_1^2}\ \tau + 1\right) \qquad 2\text{-}2.16$$

where the maximum value that τ can take is $1-r_1^2/r_2^2$. Knowledge of the differentiated signal allows one to adjust the value of the RC time constant so as to yield the maximum pulse height while keeping the differentiated pulse to a reasonably low width.

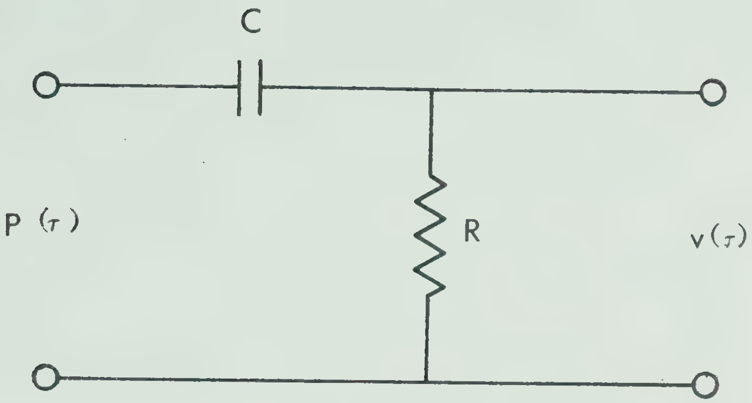

Fig. 2.3 Differentiating network.

Given the differentiating network indicated in Fig. 2.3, one has that $P(\tau) = q/c + v(\tau)$. Differentiating,

$$\frac{dP(\tau)}{d\tau} = \frac{i}{C} + \frac{dv(\tau)}{d\tau} \qquad \text{2-2.17a}$$

Letting $v(\tau) = iR$,

$$\frac{dP(\tau)}{d\tau} = \frac{v(\tau)}{RC} + \frac{dv(\tau)}{d\tau} \qquad \text{2-2.17b}$$

In Fig. 2.3, c is the capacitance of the counter. If the counter signal is decoupled through a capacitor, the differentiating capacitance becomes the series sum of the two. Substituting in 2-2.17b for $dP(\tau)/d\tau$ and setting $1/RC = S$, the first order linear differential equation reduces to

$$\frac{dv(\tau)}{d\tau} + SV(\tau) = \frac{1}{2\ \ln(r_2/r_1)} \cdot \frac{1}{(\tau + r_1^2/r_2^2)} \qquad \text{2-2.18}$$

$$0 < \tau < 1 - r_1^2/r_2^2$$

The solution for $v(\tau)$ is found in terms of the exponential integral, Ei , and has the form

$$V(\tau) = \frac{1}{2\ \ln(r_2/r_1)} \ \frac{\mathrm{Ei}\ [S(\frac{r_1^2}{r_2^2} + \tau)] - \mathrm{Ei}(S\ \frac{r_1^2}{r_2^2})}{\mathrm{Exp}\ [S(\frac{r_1^2}{r_2^2} + \tau)\ ]} \qquad 2\text{-}2.19$$

where

$$\mathrm{Ei}(x) = \fint_{-\infty}^{x} \frac{e^x}{x}\ dx\ , \quad x > 0\ .$$

In the limit of a long differentiating time constant RC (S small), the exponential integral becomes

$$\mathrm{Ei}(x) \xrightarrow[x \to 0]{} \gamma + \ln x$$

where γ is the Euler constant. Then, $v(\tau)$ reduces to

$$V(\tau) \xrightarrow[S \to 0]{} \frac{1}{2\ \ln(r_2/r_1)} \quad \ln(1 + \frac{r_2^2}{r_1^2}\ \tau\ ) \ = P(\tau)\ . \qquad 2\text{-}2.20$$

In particular, the maximum value of $v(\tau)$ corresponds to the maximum value of $P(\tau)$.

In the case of very strong differentiation of the

counter signal (S very large),

$$Ei(x) = \frac{e^{x}}{x}\left[1 + \frac{1}{x} + \frac{2!}{x^{2}} + \ldots\right]$$

and to a first approximation

$$V(\tau) \xrightarrow[S \to \infty]{} \frac{1}{2\ \ln(r_2/r_1)} \left[\frac{1}{S\left(\frac{r_1^2}{r_2^2} + \tau\right)} - \frac{e^{-S\tau}}{S\left(\frac{r_1^2}{r_2^2}\right)} \right] \qquad 2\text{-}2.21$$

As $S \to \infty$, the second term in brackets goes to zero, and equation 2-2.21 reduces to

$$V(\tau) \simeq \frac{1}{2\ \ln(r_2/r_1)} \ \frac{1}{S} \ \frac{1}{\left(\frac{r_1^2}{r_2^2} + \tau\right)} = \frac{1}{S} \ \frac{dP(\tau)}{d\tau} \qquad 2\text{-}2.22$$

Since S is positive, the term

$$\frac{e^{-S\tau}}{S\ (r_1^2/r_2^2)} \qquad 2\text{-}2.23$$

will always be >0 (Equation 2-2.21). Therefore, this term will tend to reduce the value of the term in square brackets. The maximum value of V( ) for $S \gg r_2^2/r_1^2$ thus occurs when the expression 2-2.23 vanishes. The exponential can then be expanded in a power series as follows:

$$\frac{e^{-S\tau}}{S(r_1^2/r_2^2)} = \frac{1}{S(r_1^2/r_2^2)} \sum_{K=1}^{\infty} (-1)^K \frac{(S\tau)^K}{K!} \quad . \qquad 2\text{-}2.24$$

Applying the ratio test on the infinite series one finds that it converges for $S\tau = 1$. In practice, since $S(r_1^2/r_2^2) >> 1$ the maximum value that $V(\tau)$ can take is obtained from equation 2-2.22 by letting $\tau = 0$ (recall that in $P(\tau)$, $\tau max = 1 - r_1^2/r_2^2$). For differentiation such that $1 << S << r_2^2/r_1^2$, equation 2-2.22 still holds, but in this case the time for which $V(\tau)$ is maximum is determined by[12]

$$\frac{1}{S\tau} = \ln(r_2^2/r_1^2)\,\tau \quad . \qquad 2\text{-}2.25$$

2.3 Parameters affecting the counter operation

In proportional counters, efficient detection of ionizing radiation depends largely on the gas amplification. In many applications the proportional counter is limited by fluctuations in avalanche size due to the probabilistic nature of the ionization processes. In general, fluctuation in size and shape of the output pulses are acceptable wherever the device is used to count events. The proportional counter, however, is employed in other types of

measurements such as energy resolution[25,50], particle discrimination[26], etc. In such applications gas gain fluctuations must be minimized and accounted for. For completeness, a brief analysis of the origin of such fluctuations will follow.

Statistical fluctuations occur in the number of primary ion pairs, N_i, produced by the ionizing radiation to be detected, and in the number of secondary electrons, n, produced in the avalanche initiated by each primary electron. The fluctuation in avalanche size becomes more serious as N decreases, as for example, in the detection of soft x-radiation and in ultraviolet radiation.

The statistics of electron multiplication phenomena have been considered both theoretically and experimentally by various authors[45-51]. Curran *et al.*[46] have determined the distribution of avalanche size in cylindrical counters by releasing single slow electrons at the cathode (photoelectrons). The authors found that the distribution in the output pulses due to single primary electrons was best fitted by a curve of the form

$$\tau(n) = n^{\frac{1}{2}} \exp(-n) \ . \qquad 2\text{-}3.1$$

The authors calculated the variance, σ_n^2, as follows:

$$\bar{n} = \int_0^\infty n \ P(n) \ dn \Bigg/ \int_0^\infty P(n) \ dn$$

$$\bar{n} = \Gamma \ (5/2) / \ \Gamma \ (3/2) = 3/2$$

$$\overline{n^2} = \int_0^\infty n^2 \, P(n) \, dn \Big/ \int_0^\infty P(n) \, dn$$

$$\overline{n^2} = \Gamma\,(7/2)/\,\Gamma\,(3/2) = 15/4$$

and

$$\sigma_n^2 = \overline{n^2} - (\bar{n})^2 = 3/2 \qquad 2\text{-}3.2$$

from which the relative variance is $(\sigma_n/n)^2 = 2/3$. To explain the experimental result of Curran et al. , Byrne[47] proposed a model in which the ionization probability is a decreasing function of the avalanche size and arrived at a Polya or negative binomial distribution of the form

$$P(n) = n^{(\frac{1}{b} - 1)} \exp\,(-n) \qquad 2\text{-}3.3$$

This particular distribution has a relative variance given by

$$\left(\frac{\sigma_n}{\bar{n}}\right)^2 = b + \frac{1}{\bar{n}} \simeq b \qquad 2\text{-}3.4$$

for reasonable gas gain in which case $\bar{n} \gg 1$. The Polya distribution reduces to that found by Curran et al.[46] when $b = 2/3$ and to the monotonic decreasing distribution, often referred to as the Furry distribution, derived by Snyder[45],

for b = 1. Byrne concluded that b should take values between 1 and 0.61, setting a lower limit to the relative variance. In addition to the fluctuation in the number of secondary electrons produced in the avalanche, there are fluctuations in the number of ion pairs N_i produced by the initial ionization. These fluctuations have been analyzed by Fano[52] who showed that the relative variance should be given by

$$\left(\frac{\sigma_N}{\bar{N}}\right)^2 = \frac{F}{\bar{N}} \qquad 2\text{-}3.5$$

where N is the mean number of ion pairs produced and F is the Fano factor, which is determined experimentally. Alkhazov *et al.*[53] have measured F values for various gases and gas mixtures.

Provided that there are no interactions between the ionization produced by the incident radiation and the secondary processes occurring during the avalanche formation, probability theory gives the energy resolution of the counter as

$$\left(\frac{\sigma_E}{E}\right)^2 = \left(\frac{\sigma_N}{\bar{N}}\right)^2 + \frac{1}{\bar{N}}\left(\frac{\sigma_n}{\bar{n}}\right)^2 \qquad 2\text{-}3.6$$

where σ_E^2 is the variance of the measured value of E due to fluctuations in the primary ionization and in gas amplification. The mean number of ion pairs $\bar{N}$ is related to E by W, the energy required to produce an ion pair, in the following way:

$$N = \frac{E}{W}$$

Hence,

$$\left(\frac{\sigma_E}{E}\right)^2 = \frac{WF}{E} + \frac{W}{E}\left(\frac{\sigma_n}{\bar{n}}\right)^2 \qquad 2\text{-}3.7a$$

and

$$\frac{\sigma_E}{E} = \left[\,WF + W\left(\frac{\sigma_n}{\bar{n}}\right)^2\right]^{\frac{1}{2}} E^{-\frac{1}{2}} \;. \qquad 2\text{-}3.7b$$

In equation 2-3.7, F and W are characteristic of the gas and $(\sigma\bar{n}/\bar{n})^2$ is the relative variance in the number of electrons in the avalanche, which can be replaced by the upper and lower limits of 1 and 0.61 found by Byrne[47].

The gas amplification, and therefore counter operation, depends to a great extent on the gas mixture to be used and on the physical characteristics of the counter. According to Wilkinson[12], any gas used as an ionizing medium will produce gas amplification in a region of high electric field. This is quite true, however, in a proportional counter, requirements such as gain stability, large amplification and low working voltage usually limit the choice of gas. Noble gases (Ne, Ar, Kr, Xe) are often preferred because they provide higher gain. Pure noble gases, however, are very seldom used as a gas filling: mixtures of noble and polyatomic gases in varying percentages are more frequently encountered. In ionizing collisions, noble gas atoms can be excited to metastable states of rather long life times (of

the order of 10^{-4}sec). The addition of small amounts of a polyatomic gas favours a faster de-excitation of the atoms to their ground levels through collisions with the added impurities[12, 54].

Other phenomena associated with avalanche formation which discourage the use of noble gases are processes which favour the production of secondary avalanches. These are photoelectric emission and positive ion bombardment of the cathode[22, 26]. Both effects are minimized by the addition of complex molecules. In fact, the more complex the molecule, the greater the stabilizing effect . Charpak *et al.*[26] suggested the use of gas mixtures of argon with various organic quenching agents. Such mixtures are particularly useful when the counter is operated in a rather dirty environment.

For well known gas mixtures in common use in proportional counters (argon-methane, argon-isobutane, argon-carbon dioxide), gas gains of 10^6 have been reported[26, 28] . Bemporad *et al.*[55] found that the addition of a small percentage of heptane to an argon-propane mixture resulted in the suppression of discharge, allowing higher operating voltages and consequently higher gain.

In general, the exponential growth of the avalanche is limited by the space charge effect. This occurs when the amount of charge liberated in the avalanche becomes comparable to the charge stored in the anode at the same location[56]. Bouchier *et al.*[28], adding 0.3-0.6% of Freon 13B1

to a standard argon-isobutane mixture (70% Ar - 30% isobutane), were able to overcome the limit of gas amplification set by the space charge phenomenon. The magic gas, as it is normally referred to, increases the gas gain by about 100, giving an overall gain of 10^8 without entering into the Geiger region. It has been suggested by various authors[28 57] that the attainment of such large amplification is due to the neutralization of the space charge effect by the electronegative Freon 13B1. This view has been challenged by Lacy et al.[58] who claim that rather than space charge neutralization, the avalanche beyond a certain limit becomes photo-aided without showing the Geiger mode behaviour. Gas mixtures containing electronegative gases are frequently employed with multiwire proportional chambers. These gases reduce the sensitive zone around each anode wire to a narrow cylinder[59].

The usefulness of a gas mixture is determined by the gas amplification and by the preservation of its chemical characteristics over an extended period of time. Gases containing hydrocarbons often necessitate regular cleaning of the counter because of the polymerization which can take place during the development of the avalanche and due to occasional sparking. The quality of the magic gas was shown to degrade with the age of the mixture, but could be restored with the addition of a fourth component, methylal or propylic alcohol[57]. Very often for long term operation, the inert mixtures such as argon-carbon dioxide are

preferred because they give the counter a longer operating life.

Important from the point of view of gas amplification are the requirements placed on the collecting electrode. This is so in view of the fact that gas amplification takes place near the anode where the field varies as $1/r_a$[54] (r_a = anode radius). A reduction in the anode size allows for a reduction in the working voltage while preserving the same field strength. In proportional counters the anode radius is usually kept as small as possible (few micrometres) in order to obtain high gas amplification. The minimum anode size is set by the tensile stregth needed to withstand the electrostatic forces[60]. Gas gain non-uniformity resulting from variations in the anode size along its length has been studied by Dimcovski[61]. According to the author, the main contribution to gain fluctuation arises from local variation of the anode wire and by accidental irregularities caused by either impurities attached to the anode or sparks. The conclusions were that for a fixed anode-cathode distance, the greater the anode radius, the higher the relative wire uniformity must be.

In multiwire proportional counters the anode wire spacing s and the electrode gap L play important roles in the counter operation. Charpak *et al.*[54] found that by decreasing s, the anode voltage must be increased in order to preserve the same charge per unit length and consequently the same amplification. This becomes clear from the

calculation of the capacitance per unit length c = q/v with respect to the electrodes.

For a cylindrical proportional counter, and for that matter any single anode counter, of interest is the effect of a reduction in L. Decreasing the gap between anode and cathode, the capacitance is increased thereby achieving the same gas gain with a somewhat reduced voltage. In cylindrical counters the capacitance per unit length is given by

$$C = \frac{1}{2\ \ln\left(\frac{r_c}{r_a}\right)} \quad . \qquad 2\text{-}3.8$$

For a fixed anode radius r , a reduction in gap length implies a reduction of r . The charge stored in the anode wire per unit length due to the applied voltage V is given by the simple relation

$$q = VC = \frac{V}{2\ \ln\left(\frac{r_c}{r_a}\right)} \quad . \qquad 2\text{-}3.9$$

CHAPTER 3

SINGLE COUNTER DESIGN

3.1 General considerations

Most proportional counters with a single central anode have cylindrical geometry. Such devices are preferentially used in experimental work concerning phenomena associated with their principle of operation. In constructing a detector for axoplasmic transport studies, however, the rectangular cross section has definite advantages over the cylindrical configuration. Although study of the rectangular multianode proportional counter of box-type geometry has been reported by other authors[40], little is known about the performance of rectangular proportional counters with a single anode.

In the construction of a position sensitive detector suitable for axoplasmic transport experiments, there were three underlying considerations:

(a) high counting efficiency for β-radiation,

(b) narrow field of view of the counter, and

(c) low background counting rate.

3.2 Centred anode: single counter design

In order to design a detector which meets the criteria previously mentioned, we first constructed and tested a number of single wire proportional counters. These devices were rectangular of length 5 cm and various widths and

depths. Each counter consisted of a main body machined from a single piece of aluminum, with one side an entrance window consisting of 10 micrometres aluminized mylar glued onto the counter with conductive adhesive (Eccobond 60-L). The detector's internal surfaces were made as smooth as possible to reduce possible discharge at sharp points. A 20 micrometre gold-plated tungsten wire properly tensioned (about 15 gms) was placed at the centre of the counter and supported at each end by glass-epoxy blocks.

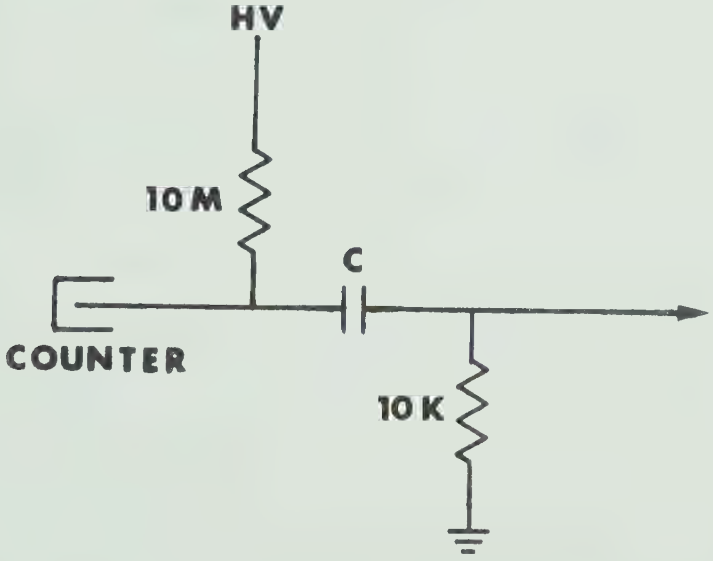

FIG. 3.1 High voltage network.

The dielectric fittings in the active region of the counter were coated with epoxy resin. One end of the anode wire was terminated in the dielectric support and the other end connected outside the chamber to the high voltage power supply via a 10 M-ohm resistor (see Fig. 3-1). The counter

signal was extracted across a decoupling capacitor and a D.C. path to ground provided by a 10 K-ohm resistor.

To allow for continuous gas flow during operation each end of the counter was equipped with a gas line connection. A steady flow of approximately 10 cc/min of 93% argon and 7% carbon dioxide was maintained by a single stage high pressure regulator. The rate was monitored with a Matheson flow meter (tube no. 600).

3-2.1 Detection efficiency to β-rays

Two types of tests were performed with the various counters to examine their detection efficiency for β-particles. In the first type, a small source of ^{14}C was placed inside the counter active volume in order that an estimate could be made of the absolute efficiency . In the second type of test a small source of ^{14}C was placed at various positions outside the mylar window in order to establish the dependence of the efficiency on position. In all studies, the counter pulses were fed via a NB-11 Hamner preamplifier into a Tennelec TC-205 linear amplifier. The amplified pulses were then passed through a Canberra SCA Model 1431 and the output counted with a digital rate meter. The SCA lower window was set just above noise level and the upper window open to accept the whole sprectrum. All values reported here were corrected for background.

In the first case, small ^{14}C sources were deposited on pieces of mylar which served as the entrance windows of the

counters, the sources being centred on the inside of the windows. This arrangement yielded, as closely as possible, 2π counting geometries. Counting rates versus high voltage were recorded up to the point of breakdown. To convert these rates to absolute efficiencies, the sources were then removed, dissolved and liquid scintillation counted.

The sources were prepared by depositing a drop of acetic acid, sodium salt (1, 2 - ^{14}C) on mylar glued to double sided tape. Following evaporation of the solvent, sources of about 1 mm in diameter were sectioned out and glued separately inside the counters as described above. The source thicknesses were estimated to be of the order of a few micrometres; this is small enough that self-absorption could be neglected. After establishing the HV-count rate dependence, the activity of each source was determined by liquid scintillation counting. Following removal, each source was dissolved in 2 ml of Protosol to which was then added 0.1 ml of glacial acetic acid to eliminate chemoluminescence . After addition of 10 ml of Econofluor, the samples were counted with a Nuclear Chicago Mark I liquid scintillation counter. To account for quenching, the counting was repeated with 5 microlitres of a standard ^{14}C-Toluene added to the sample yielding in such a way the counting efficiency. The activity of the source was then determined and compared to the count rate obtained with the proportional counter. The error associated with the total activity of the various sources was estimated at 10%. This

included the error in the standard source (^{14}C-Toluene) and the error resulting from dispensing the 5 microlitres used in the internal standard quench correction method.

Figs. 3.2 and 3.3 show the dependence of detection efficiencies on anode voltage for counters with depths of 6, 12, and 18 mm. Fig. 3.2 was obtained with 4 mm wide counters and Fig. 3.3 with counters 3 mm wide. (Measurements were also performed using 2 mm wide counters with varying depths, however, because of recurring discharge, these counter sizes had to be abandoned.) Both graphs show initially a fairly linear increase of efficiency with voltage until a plateau is reached (with the exception of the 18 mm counters), beyond which the counters quickly enter the discharge region, as indicated by the rapid increase of the efficiency. There are notable differences in plateau size depending on the counter width and depth. No plateaus are obtained with the 18 mm counters. This can be attributed to the recombination of the primary ion pairs due to the weak electric field in the region of the counter close to the window. (This is better demonstrated by the electric field plots for the various counter sizes shown later in the chapter.) There is a definite loss in plateau size in going from 4 to 3 mm wide counters (from 100 to 60 volts), and a decrease in efficiency with increasing counter depth. Efficiencies of about 75% were obtained with the 6 mm deep counters for either width. In both graphs, the error bars, due to counting statistics alone, associated with each data

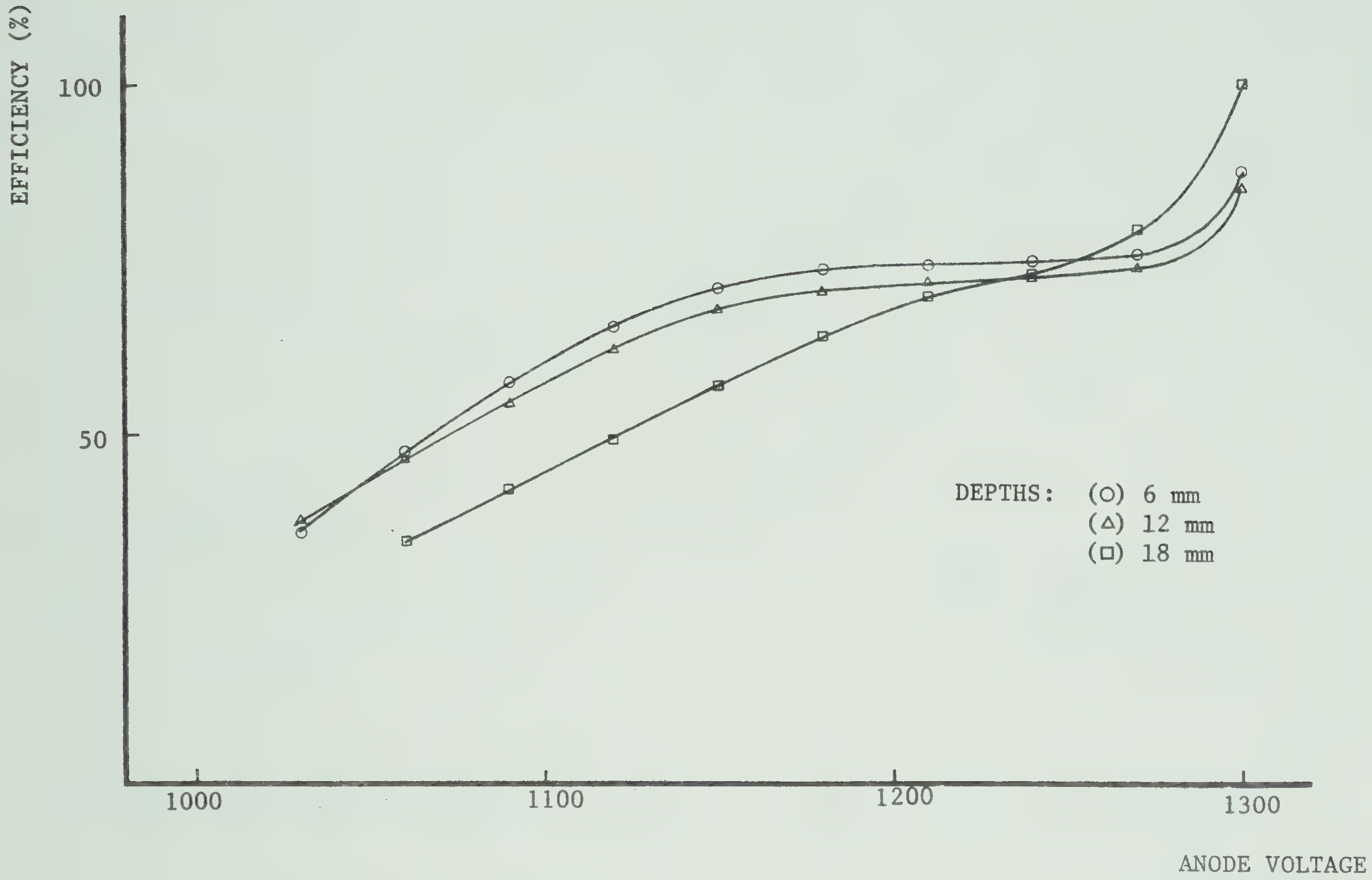

FIG. 3.2 Detection efficiency of ^{14}C for a 4 mm wide counter.

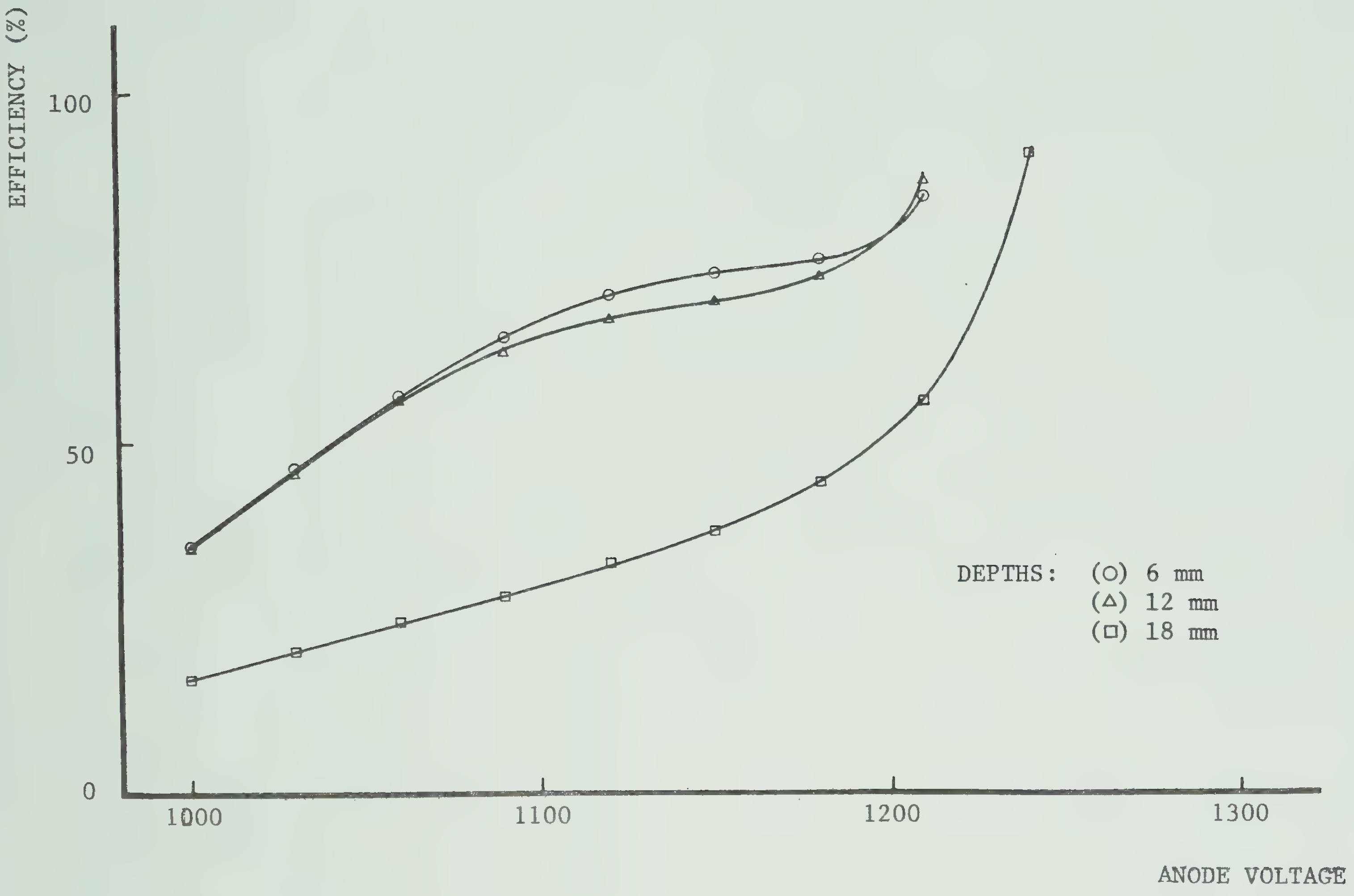

FIG. 3.3 Detection efficiency of ^{14}C for a 3 mm wide counter.

point were maintained at about the 1% level by adjusting the counting time.

In addition to good detection efficiency, it was desirable to construct a counter whose detection uniformity across its entrance window would be optimal. Measurements were performed employing counters 4 mm wide and depths of 6, 12, and 18 mm with central anode and placing an external ^{14}C source of half mm in diameter against each counter window. The source was produced by screening a wide ^{14}C spot with a copper strip supplied with a 0.5 mm circular aperture. The activity of the source through the aperture was estimated at 0.01 microcuries. The three straight lines, a, b and c in Fig. 3.4, represent the best detection efficiencies for counter depths of 6, 12 and 18 mm respectively with the source on the window at the centre of each counter. The operating voltage for these measurements was fixed at 1220 volts, which falls in the middle of the counting plateau. For simplicity, we assigned the efficiency of 100% to the 6 mm deep counter. The graph shows a marked drop in detection efficiency as the source is moved from the centre towards the edges, and becomes progressively worse with increasing counter depth. The error bars in Fig. 3.4 rapresent the percentage error which ranges from 1.1% to 1.5%. With the 3 mm wide counters, the drop-off at the two ends should be comparable in size because β-particles are confined in a narrower region about the anode.

To determine the usable central region of the counter,

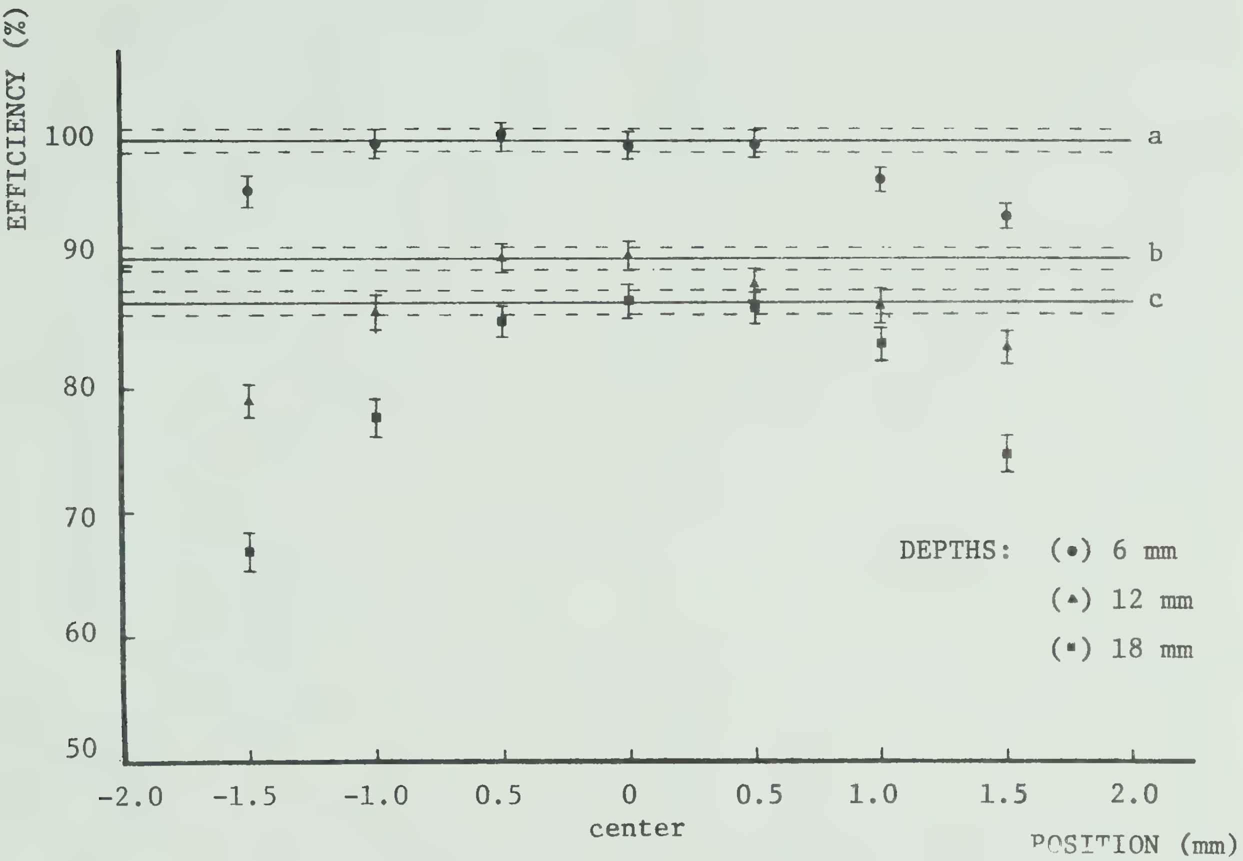

FIG. 3.4 Detection efficiency of ^{14}C across the counter window for a 4 mm wide counter. The dashed lines mark the 1% limits.

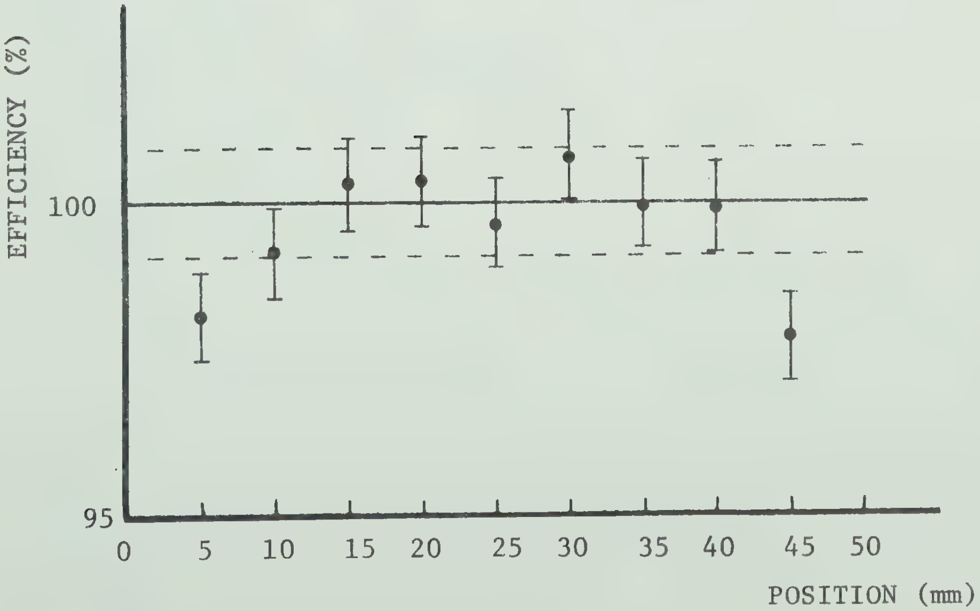

FIG. 3.5 Detection efficiency of ^{14}C for a 3 mm wide and 6 mm deep counter in the longitudinal direction.

we measured the dependence of the detection efficiency on longitudinal position using a counter 3 mm x 6 mm in dimension. In this case the source was moved parallel to the anode wire from one end to the other of the counter in steps of 5 mm. In Fig. 3.5 the straight line represents the best detection efficiency, set conveniently at 100%, while the dashed lines enclose the upper and lower limits of 1% error. Departure from such limits occurs at 5 mm from each end and can be attributed to the loss in field uniformity due to counter end-effects.

According to these preliminary tests, the 3 mm x 6 mm configuration was found suitable for the construction of the multiple counter to be described in Chapter 4. However, the lack in counting plateau size tends to discourage the use of such counters because the detection efficiency would unfavourably depend on voltage fluctuation with time. Nevertheless, given a stable power supply, the change in efficiency can be confined within acceptable limits (less than 0.1%); this is true in our case where a FLUKE Model 408B is used which has a stability of ±0.02% per day after warmup. A compromise between plateau size and spatial resolution has to be accepted in axonal transport measurements. This is achieved by using a smaller counter width, thereby increasing spatial resolution and compensating, to a certain extent, for the smaller counting plateau.

With the multiple detector the depth of the individual

counter was increased to 20 mm to ease construction problems. The optimal 3 mm x 6 mm dimensions were preserved by displacing the anode wire off centre to 3 mm from the detector window. The electrostatic study of such a counter geometry, performed in section 3.3, indicates no major change in field configuration suggesting a close similarity between the 6 mm and 20 mm deep counters.

3.3 Electrostatics of the counter

Proportional counters of rectangular cross section are preferred over cylindrical ones when an external source must be viewed using a side window configuration; in addition, large sensitive volumes are easily achieved with a single or with an array of such rectangular counters. Inherent disadvantages are that the field distribution is not isotropic and that equipotential lines become increasingly distorted with increasing distance from the anode, therefore affecting the avalanche formation.

The electrostatic problem in two dimensions for the rectangular counter was dealt with in detail by Tomitani[62]. The potential is written in analytical form using a conformal transformation of the Jacobian elliptic function. The method, however, is particular to an anode placed symmetrically in the chamber. Urbanczyk and Walisorski[63] approached the problem using the principle of finite difference approximation. This technique is a lengthy one, and in addition, the error in the approximation is affected

by various factors.

For the rectangular counter considered here it was found more convenient to use the technique based on the integral representation of potential. This method was used by Symm[65] to find equipotential contours for semicircular cross section and pill-box type detectors. In this representation there are no restrictions on the shape of the cathode and location of the anode. The numerical solution to the system of linear integral equations is easily obtained and contour plotted using a computer. Lines of equal field strength are obtained by numerical differentiation of the potential function. Details of this technique are contained in Appendix A.

This numerical method was applied to a square counter with an anode of 20 micrometres diameter placed at the centre. Both equipotential lines and lines of equal field strength were obtained and plotted (Figs. 3.6a and 3.6b). The equipotential lines (Fig. 3.6a) are plotted for potentials from 5% to 60% of the anode, in increments of 5%; the potential decreases with increased distance from the anode. It is obvious from the plot that there is some similarity with the circular case. The distortion near the corners is obviously due to the geometry of the counter. This corner effect shows up more clearly in Fig. 3.6b. The field strength drops more rapidly from anode to corner than it does from anode to side of counter. The field strength difference between the closely spaced lines in the corner is

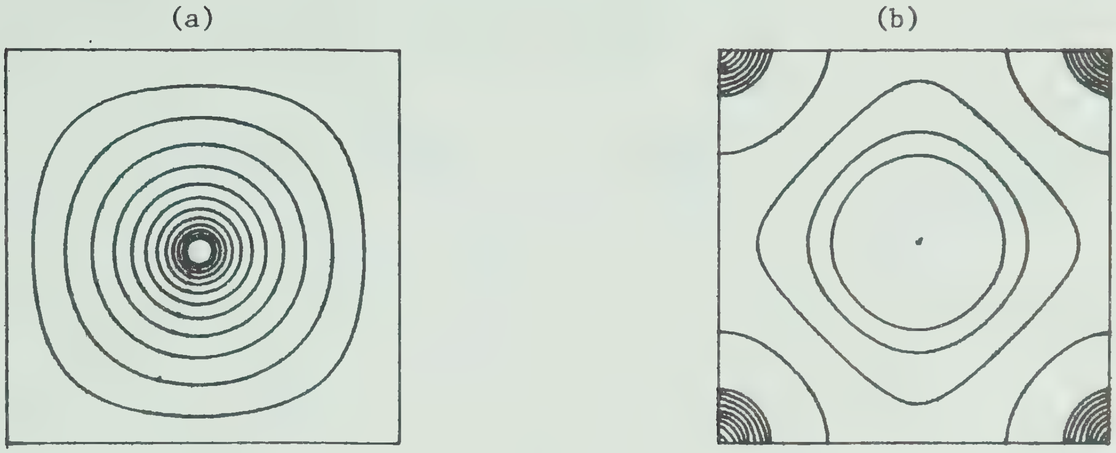

FIG. 3.6 Square counter with central anode
a) equipotential lines; b) magnitude field lines.
Refer to text for additional details.

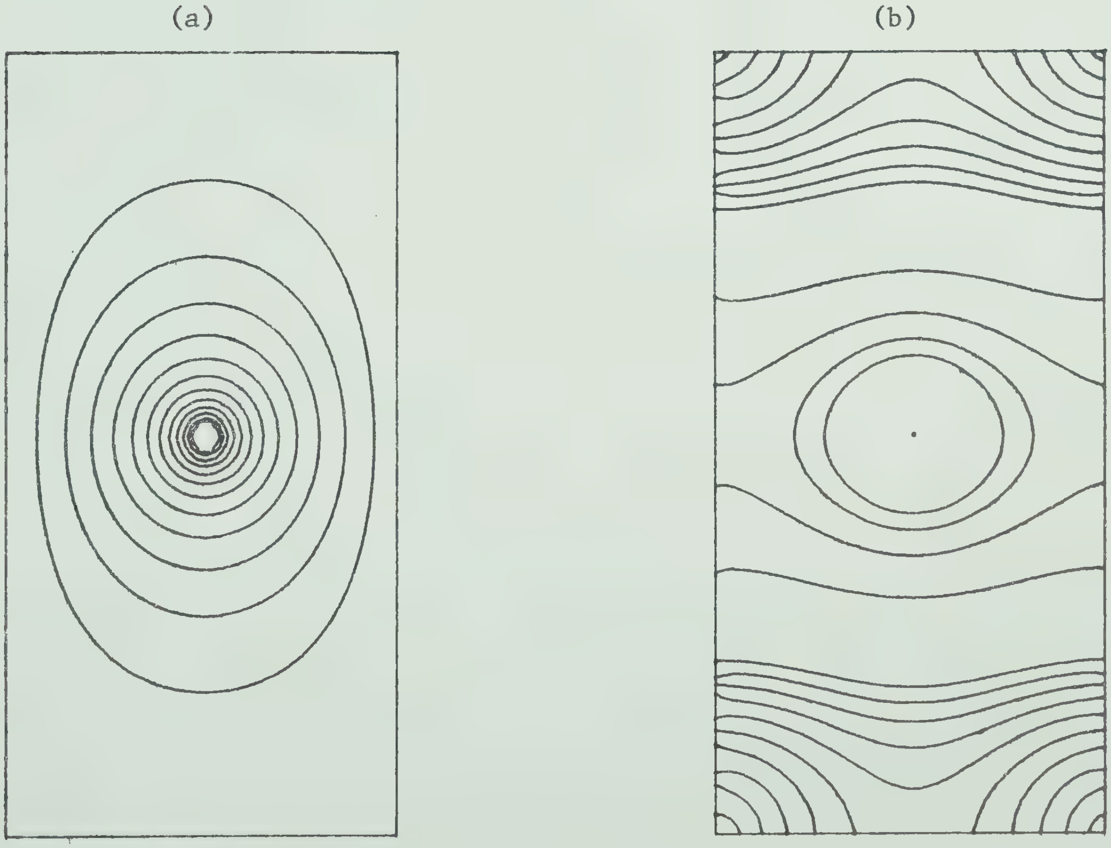

FIG. 3.7 Rectangular counter with central anode and
2:1 length:width ratio a) equipotential lines;
b) magnitude field lines.

10% of that between the wider spaced lines closer to the anode.

A similar analysis was applied to a rectangular counter. Once again, the anode is located symmetrically in the chamber. The results for a counter whose height to width ratio is 2:1 are illustrated in Figs. 3.7a and 3.7b. The equipotential again exibits a smooth decline with distance from the anode. However, as in Fig. 3.6b, Fig. 3.7b shows clearly the anisotropy of the field strength. Results for a counter whose ratio of dimensions is 4:1 are illustrated in Figs. 3.8a and 3.8b. A disconcerting aspect of the anisotropy of the field is the weakness of the field at the corners. Ion pairs produced in these regions of the counter have relatively long drift times, therefore enhancing the probability of recombination. Another important consideration to be made is that electrons liberated in these regions are more likely to be captured by electronegative impurities present in the detector than if they were released in regions of higher field intensity.

To preserve the field strength towards the upper end of the counter which holds the entrance window, the anode was displaced off centre. This particular configuration was necessary for the construction of the multiple detector and described in the following chapter. Figs. 3.9a and 3.9b are the result for a counter with sides of 2:1 ratio and anode displaced 3/4 of the height. In the upper quarter of the counter the equipotential and absolute field resemble the

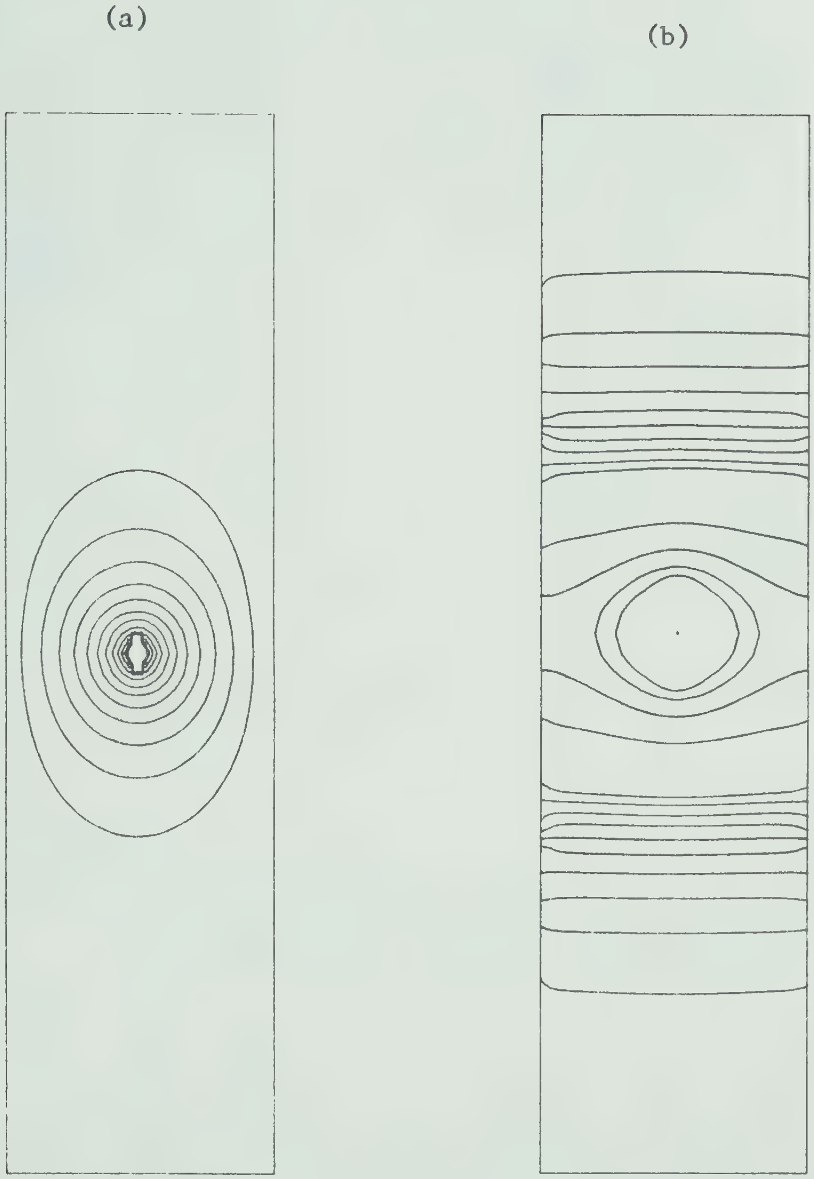

FIG. 3.8 Rectangular counter with central anode and 4:1 length to width ratio a) equipotential lines; b) magnitude field lines.

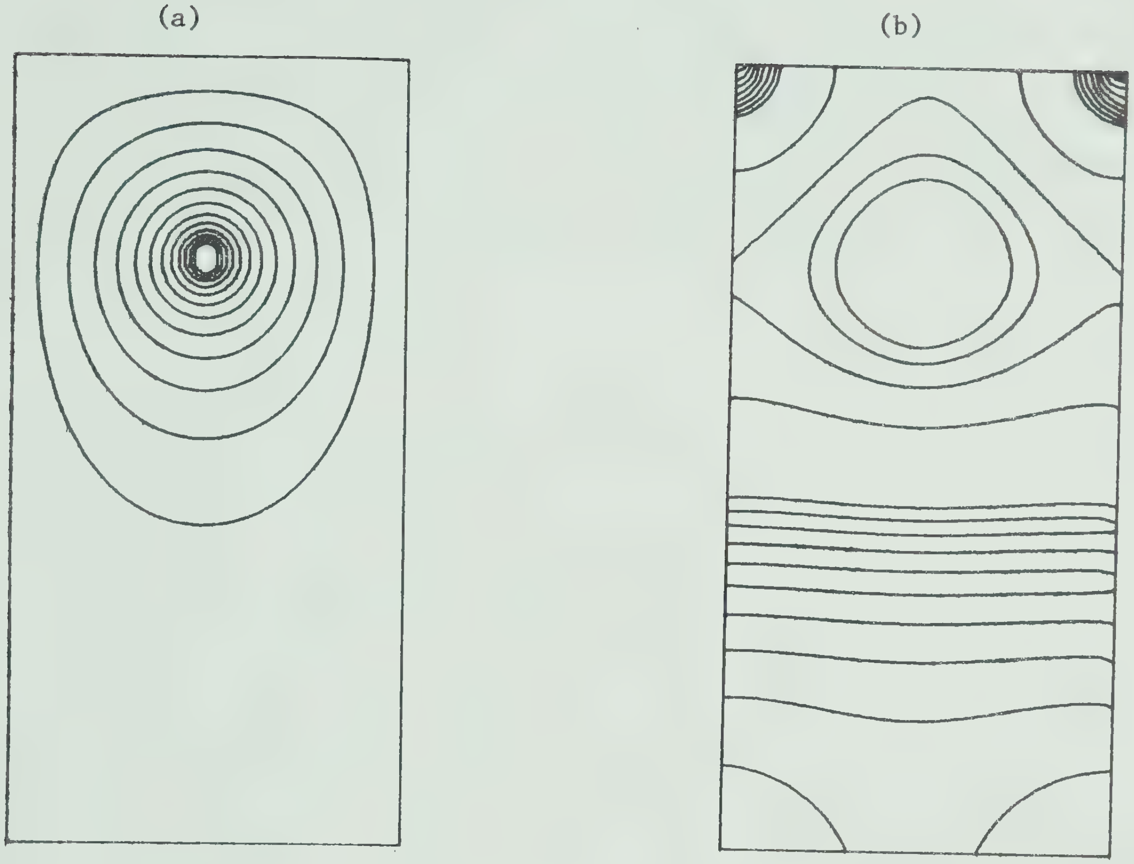

FIG. 3.9 Rectangular counter with off-set anode.
a) equipotential lines; b) magnitude field lines.

square counter with centrally located anode. The lower part is similar to the rectangular counter (See Fig. 3.9a and Fig. 3.8a). This almost field free region can be extended without significantly affecting the upper active region of the counter as is shown in Figs. 3.10a and 3.10b where the sides are in 4:1 ratio and the anode located at 3/4 of its height.

3.4 Off-set anode: single counter

The electrostatic study of a counter with off-set anode showed that the equipotential contours towards the window were little affected as the counter depth was increased, provided the anode location remained unchanged. It was reasonable to assume that the detection characteristics of the 3 x 6 mm² counter with central anode could be preserved if the height was increased to 20 mm, keeping the other parameters unaltered. Using a counter of dimensions 3 mm by 20 mm (width-depth respectively), with the anode 3 mm from the window, we determined the detection efficiency as described in section 3.2. Fig. 3.11 shows the efficiency of β-particle detection versus anode voltage. The size of the counting plateau remains at about 60 volts with an efficiency ranging from 65% to 72% between the lower and upper ends of the plateau.

The relative detection efficiency across the counter window was again determined adopting the procedure used with the different 4 mm wide counters (See section 3.2). In

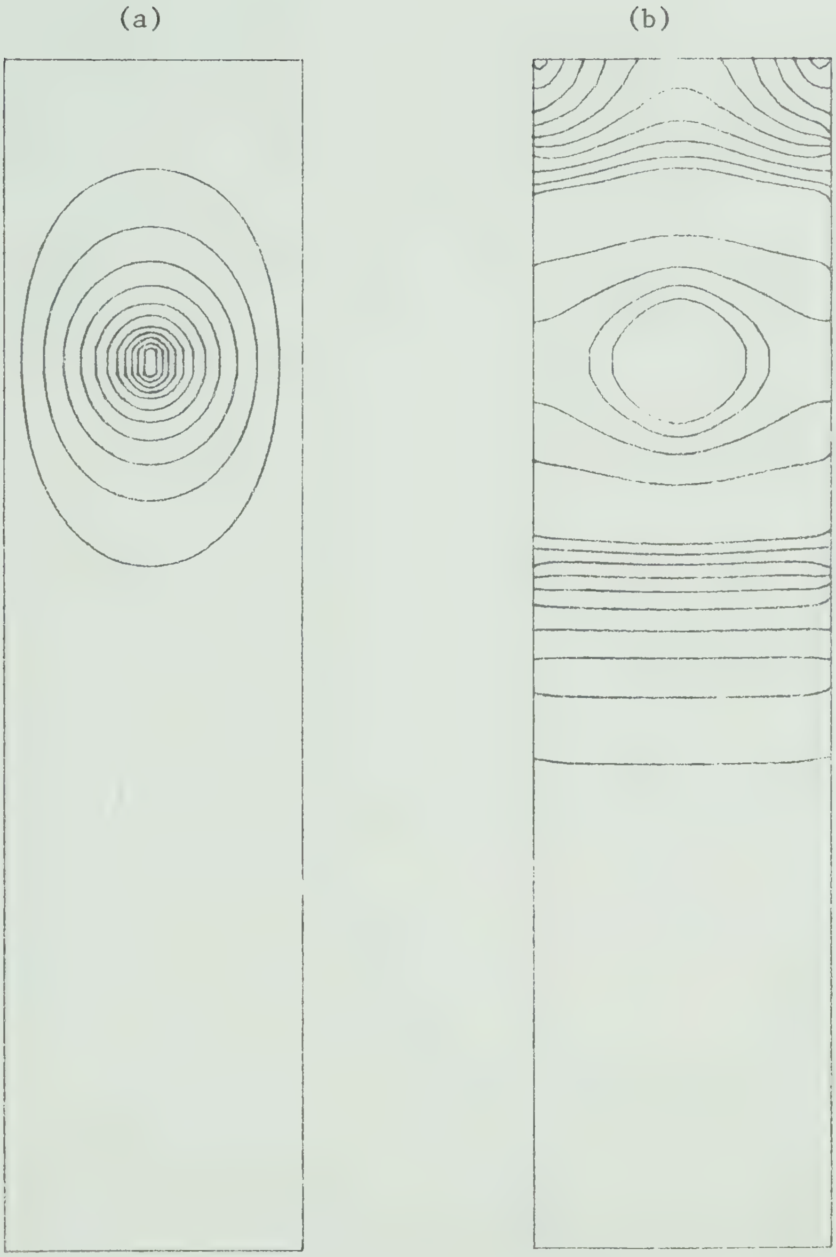

FIG. 3.10 Rectangular counter with off-set anode and 4:1 lenth:width ratio. a) equipotential lines; b) absolute field line.

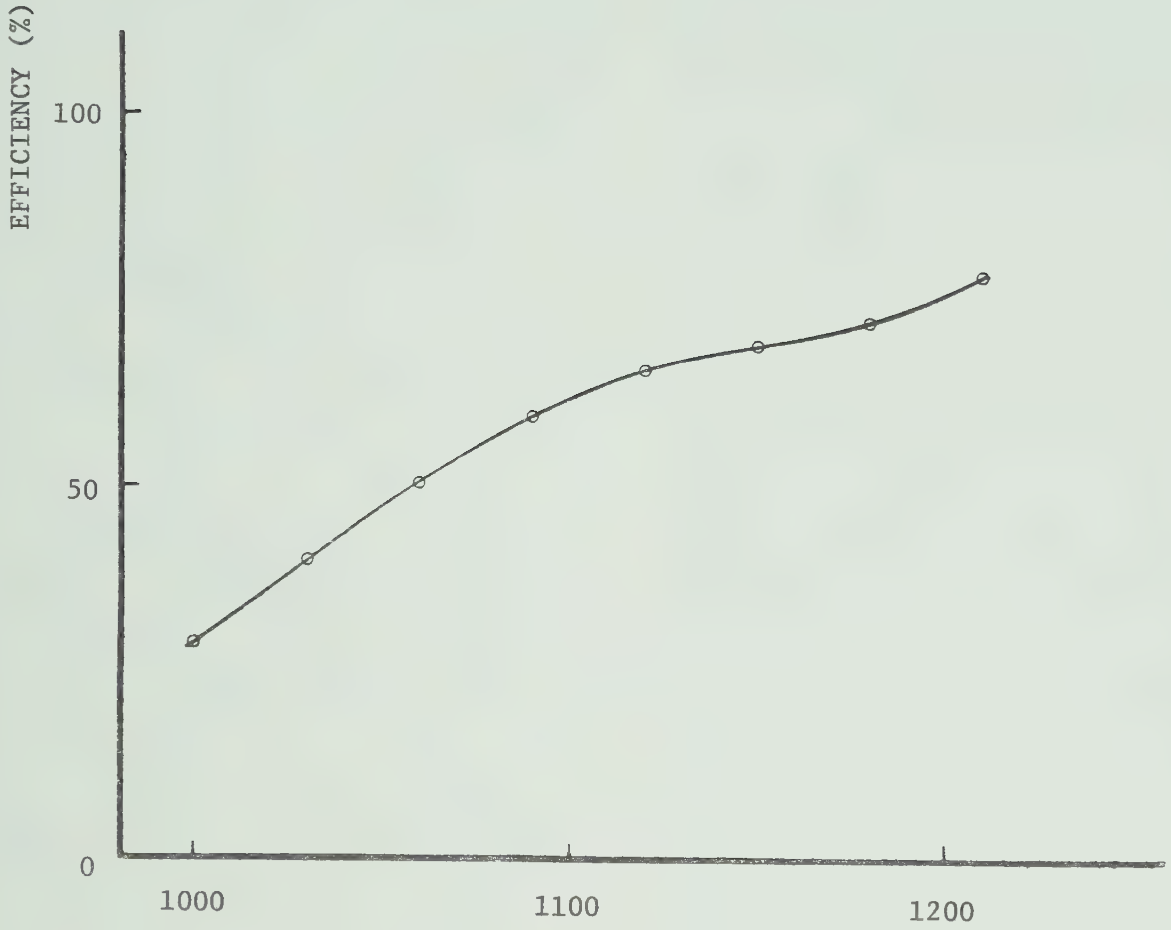

FIG. 3.11 Detection efficiency of ^{14}C for a 3 mm by 20 mm counter with off-set anode.

Fig. 3.12 the straight line represents the optimal detection efficiency, set once more for simplicity at 100%, and corresponding to anode voltage of 1150 v. The magnitude of the error bars accounts for the fractional error, which ranges from 1.6 to 1.8%.

A typical β-spectrum of an external ^{14}C source obtained with the 3 mm by 20 mm counter is shown in Fig. 3.13. The amplified pulses were, in this case, fed into an ORTEC 6240 MCA for pulse height analysis. The spectrum shown was obtained at the plateau voltage of 1150 V. The system was calibrated using the 5.9 KeV Mn K x-ray of ^{55}Fe and assuming a linear relation between channel number and energy. The spectrum itself represents the response of the counter to the distribution in energy deposition within the gas volume.

3.5 Background

In axoplasmic transport studies, the activity to be measured depends on the uptake of labelled amino-acid precursor by the nerve soma and the amount of active material which is actually transported down the nerve. Indications are that only 50-200 ppm of the original activity is transported into the axons. Due to the geometry of the experiment, only a small fraction of this activity (0.2 - 2%) will actually be detected by the counter. As an example, for nerves incubated with 0.5 mCi of ^{14}C or ^{35}S in a 2.5 ml of Ringer's solution, the expected counting rate will be of the order of a few counts per second. This

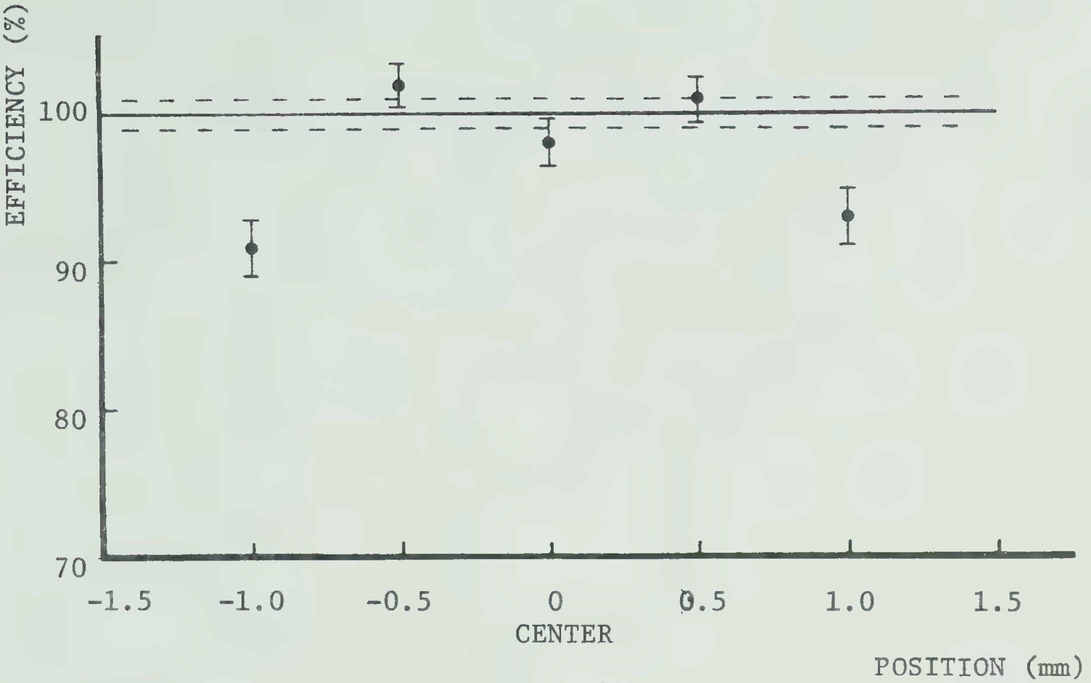

FIG. 3.12 Detection efficiency of ^{14}C across the counter window (3 mm by 20 mm).

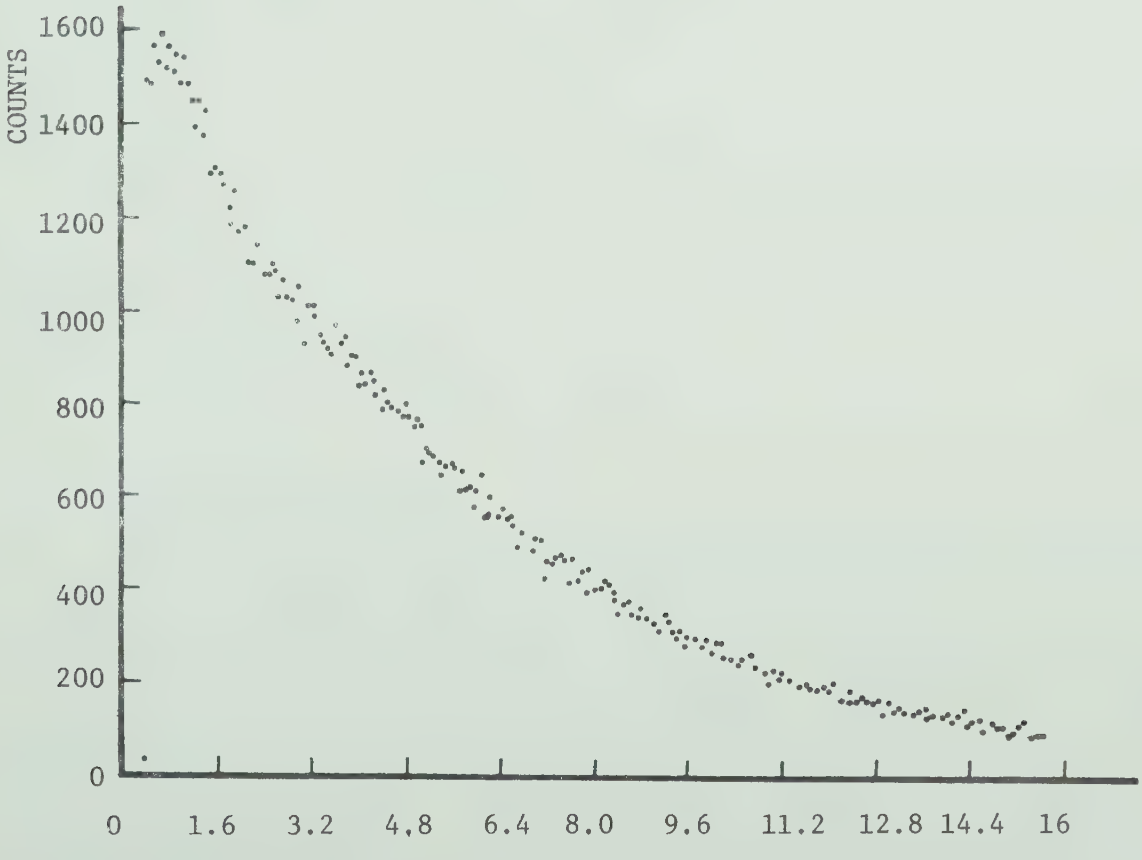

FIG. 3.13 Typical ^{14}C β-spectrum (3 mm by 20 mm counter).

necessitates a low background counting rate.

The background arising from isotopes of the counter material and gas, such as ^{26}Al and ^{14}C, are negligible . Background due to cosmic radiation should be negligible mainly because of the small counter volume; measurements of background performed with and without lead shielding showed a difference of 4%, attributable in part to cosmic radiation. Fig. 3.14 shows the background spectrum of a 3 mm wide and 20 mm deep counter (without lead shielding) taken over a period of 4000 sec. The electronic noise pick-up is indicated by the sharp rise at the lower end of the spectrum and is normally reduced by raising the lower level discriminator. Threshold adjustment is needed whenever the noise level is of the same order of magnitude as or greater than the actual activity under measurement . In our case the threshold level was kept as low as possible to minimize the loss of β-spectrum at the lower energy end. Operating under typical conditions, a background counting rate of 6-8 cpm for a 3x20 mm^2 counter was observed.

3.6 Gas amplification

One important aspect of proportional counter operation is the signal amplification resulting from the ionization of the gas mixture by the primary radiation and the following formation of the avalanche at the collecting electrode. The charge constituting the avalanche depends in general on the gas mixture and on the physical characteristics of the

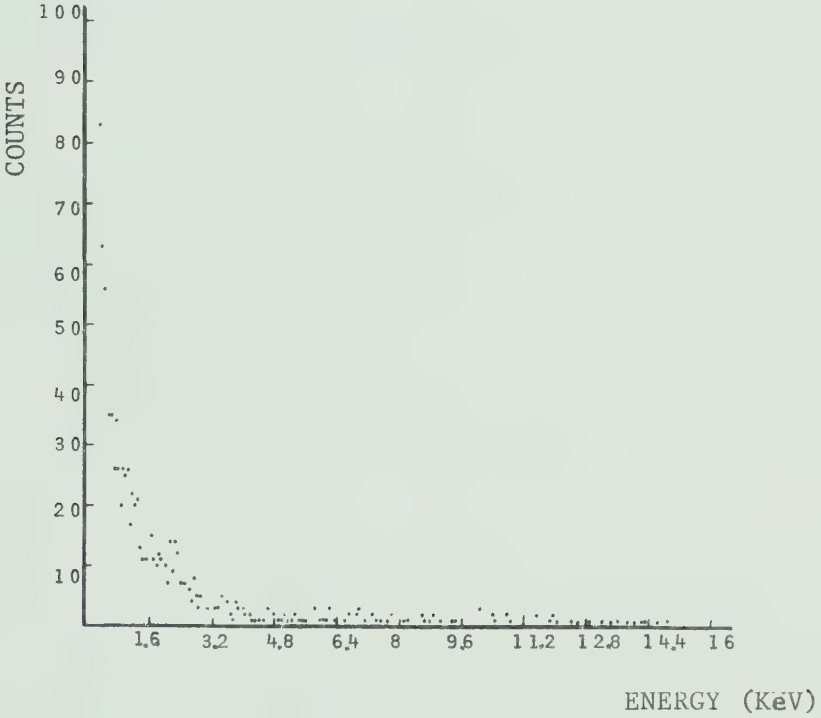

FIG. 3.14 Background spectrum for a 3 mm by 20 mm counter.

counter. With reference to our particular counters, of interest is the effect that the anode-cathode spacing has on gas amplification. Mixtures of argon and carbon dioxide are often used as the interacting gas medium in proportional counters. The gas adopted in our work had a composition of 93% argon and 7% carbon dioxide, and was obtained from Matheson Co. Inc.

The counters used for gas gain measurements had rectangular cross sections with depths of 6, 12 and 18 mm, and widths of 3 and 4 mm. The anode in all cases was located at the centre of the counter. Gas flow was maintained constant throughout a measurement using a single stage high pressure regulator. The flow rate was monitored with a Matheson tube flow meter. Each detector was first purged by a fast flow of gas and then allowed to stabilize at a low rate. The equilibrium condition was checked using a collimated ^{55}Fe source by noting the shift in peak position, using a multichannel analyser (ORTEC 6240A). The anode potential was provided by a FLUKE high voltage power supply (Model 408B) with an accuracy of 0.25%.

The counter pulses were fed through a charge sensitive preamplifier (ORTEC 109A) into a Tennelec TC-205 linear amplifier having a shaping constant of 3 microseconds. The signal was then analyzed using the MCA. To calibrate the system, voltage pulses with a rise time of 20 nanoseconds and a decay time of 200 microseconds were fed through a known capacitor into the amplifying system and the pulse

height analysed by the MCA. A series of calibration curves showing the relationship of charge to channel number for various amplifier gains was obtained.

A collimated ^{55}Fe source emitting 5.9 keV Mn K x-rays was placed against the counter window. The charge resulting from the absorption of the photons at different anode voltages was fed through the amplifying system. The location of the photo-peak permitted the determination of the total charge produced by the N_i ion pairs where $N_i = (5900\ \text{eV})/W$. For our particular gas mixture the average ionization energy, W, (26.6 eV) was computed using the approximate relation suggested by Meyers[66]:

$$\frac{1}{W} = \sum_i \frac{P_i}{W_i}$$

In the above expression P is the relative partial pressure for the i-th gas component and W_i the corresponding ionization energy for the pure gas, obtained from Whyte[11].

This technique of comparing a known amount of charge to the total charge generated in the detector has been used by other investigators[19,68,69]. Its inadequacies stem from the fact that the rise time of the charge pulses from the precision pulser-capacitor, and the detector may be significantly different, in which case the pulse-shaping networks in the preamplifier and main amplifier will respond differently. Thus, two identical quantities of charge derived from the two devices will produce pulses which are

different at the output of the main amplifier. In absolute gas gain measurements the attenuation produced by the shaping networks must be taken into account. Otherwise, the calibration procedure is quite acceptable in cases such as ours where aproximate gains are required, as in demonstrating the dependence of gas gain on counter size.

Fig. 3.15 is the graphical representation of the number of electrons produced by an ion pair versus anode voltages for a number of counter sizes. In the voltage ranges considered the results obtained compare favourably with values reported in the literature[56]. The gas gain-voltage characteristics for the three counters of 3 x 6 mm^2, 3 x 12 mm^2 and 3 x 18 mm^2 (width x depth) are presented in Fig. 3.15a. The gas amplification for the first two of these are almost identical to one another, as indicated by the overlap of the two lines. The gain for the 18 mm counter is, however, consistently lower. Similar results were obtained with 4 mm wide counters and are illustrated in Fig. 3.15b. In this case, there is again a consistent decrease in gain with increasing counter depth. The dependence of gain on counter width is demonstrated in Fig. 3.16. Line (a) shows the gain in a 3 x 6 mm^2 counter while line (b) is obtained for a 4 x 6 mm^2 counter. The drop in gain with increased width for fixed anode voltage may be attributed to the reduction in capacitance per unit length in the wider counter.

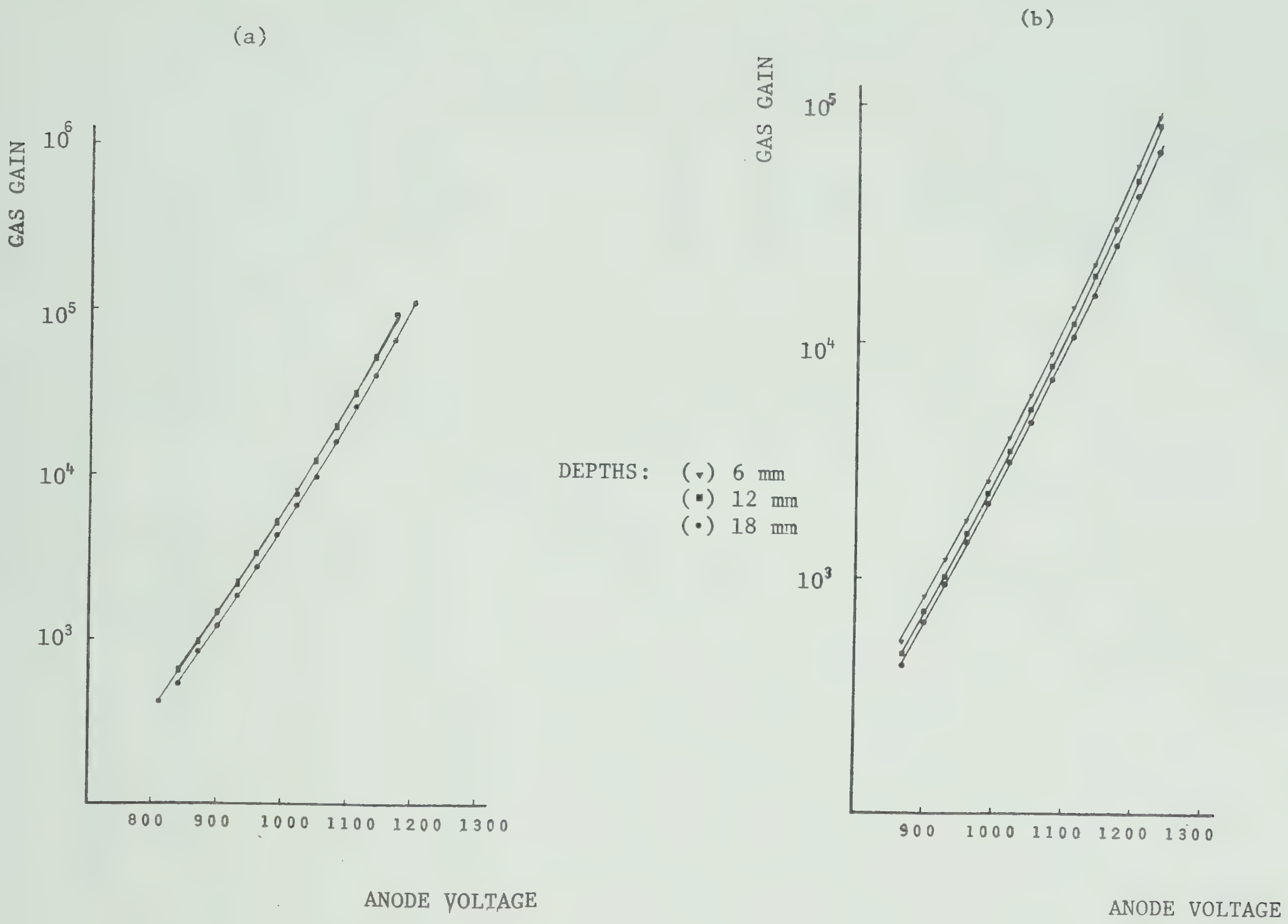

FIG. 3.15 Gas amplification for a) 3 mm and b) 4 mm wide counters.

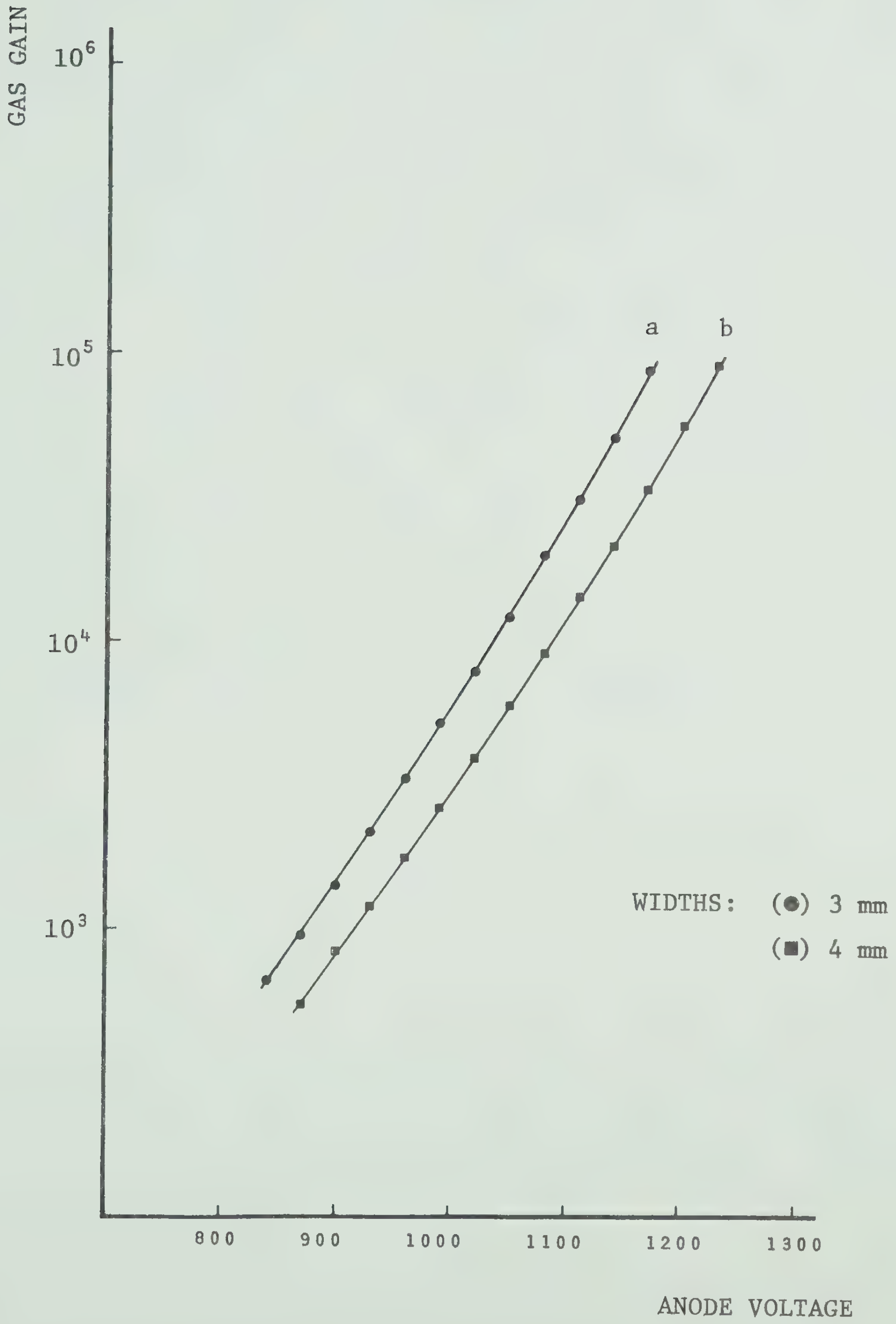

FIG. 3.16 Gas amplification for 6 mm deep counters.

3.7 Discussion

The objective of the study described in the present chapter was to test various counter sizes of rectangular cross section and to establish the optimal dimensions with regard to detection efficiency and background. Such a counter would represent one unit in a larger position sensitive detector applied to axoplasmic transport measurements. The detection characteristics of the rectangular counter were compared to the position sensitive detector, a MWPC, employed in the axoplasmic transport measurements of Snyder et al.[8]. Adopting a counter size of 3 x 20 mm^2 for the multiple detector (see Chapter 4), the spatial resolution was improved by a factor of 2 as compared to the previous system. The average detection efficiency, that is, the average efficiency at any point of the active counter region including the collimator, was increased from 48% to 60% with the new detector size. The results of the gas gain measurements indicated that the counters were in fact operating in the proportional region, and that no significant increase in gas gain could be anticipated prior to entering into the Geiger or discharge regions. In addition, the new counter had the advantage of a slightly lower background.

CHAPTER 4

MULTIPLE DETECTOR

4.1 Description of the system

A multiple detector was constructed based on the results obtained from the single counter studies. Some single counter features were modified to overcome multiple counter construction difficulties. Improvements were introduced, with particular regard to discharge phenomena. The multiple counter is composed of a linear array of 16 single chambers separated from one another by thin walls, referred to as "fins". A major effort was directed to the assembly of the various counter parts. In particular, the counter fins and wire plane were mounted in a manner which allowed for ease of replacement. For the continuous gas flow, we provided the counter with two manifolds (inlet and outlet) while allowing for separate gas apertures to each counter.

After considering various readout systems, the "one amplifier per wire" approach was chosen. The amplifier used is similar to that described by Tarlé *et al.*[69], with some changes introduced, mainly in the logic circuitry. It yields a non linear amplification with output of adjustable width and fixed height. Boards which contain 16 such amplifiers and associated logic circuitry were made available to us by the TRIUMF group of the NRC at the U. of A.

After amplification, each counter signal is assigned a

binary code so that data from each counter can be stored in a fixed location of a multichannel analyzer (MCA) memory. The data stored in the MCA is regularly dumped onto paper tape for subsequent analysis.

The multiple counter of 16 channels plus amplifiers and encoding system represents a basic unit which can be easily expanded.

4.2 Counter construction

The multiple detector consists of 16 compartments disposed in a linear array. The individual chambers are 3 x 20 x 50 mm^3 (width x depth x length) and are arranged side by side. The compartments are separated from one another by thin metal walls. Each chamber is a proportional counter with an anode wire located at width median and at a distance of 3 mm from the counter window. The multiple counter has an outer aluminum structure which provides a gas tight compartment, and in addition, electrostatic shielding.

Inside the main metallic frame is a system of four planes which hold the fins and maintain the wires in the same plane. Fig. 4.1 shows the four planes which are made of Nema G-10 glass epoxy board. Plane (a) has centre spaced vertical grooves as shown. They provide spacing and support for the fins, which are inserted from the top. The top horizontal channels surround the anode wires, which run along the centre of the counters. The function of the horizontal channels is to increase the dielectric surface

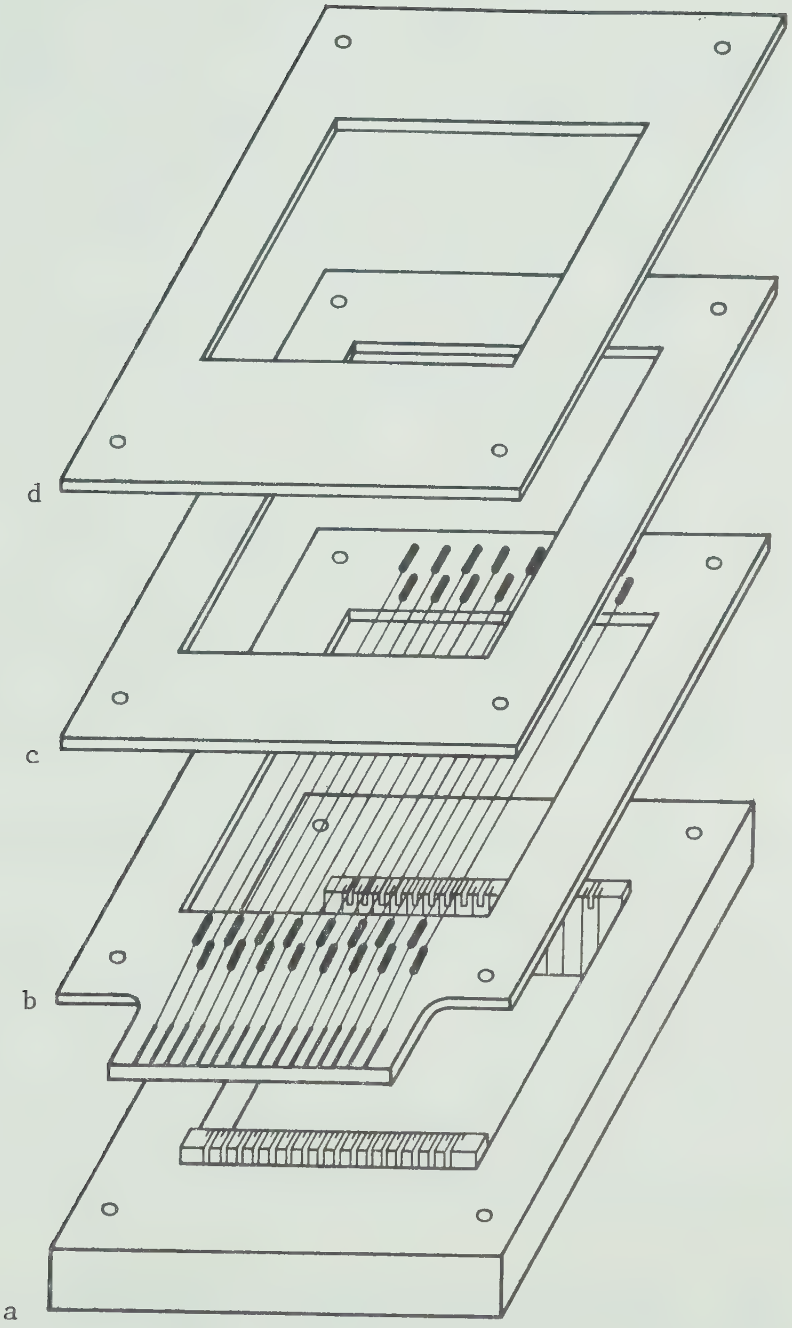

FIG. 4.1 Multiple detector: interior planes.

path length to ground, thus reducing surface leakage. The 16 20 micrometres gold plated tungsten anode wires are mounted under slight tension (about 15 gms) on plane (b). Plane (b) and the spacing plane (c) fit around the elevated parts of plane (a) as illustrated in Fig. 4.1. Plane (d), with the upper face copper plated and kept at ground potential, provides the final spacing in the counter and helps to maintain the window at ground potential by simple contact. Those non metallic surfaces enclosed in the active regions of the counter which required machining were coated with Eccobond 24 epoxy resin. This procedure helps to maintain clean and smooth surfaces, preventing leakage of gaseous impurities into the counter and reducing discharge at sharp points.

The four planes are fixed to a metallic frame, shown as section (a) in Fig. 4.2. The elevated part of section (a) has equally spaced slits for the counter fins, and in addition, small apertures at each end for continuous gas flow. These apertures are connected to the main ducts indicated by the tube fittings on each side of the counter base.

The mid section in Fig. 4.2 is provided on each side with suitable channels for the housing of O-rings. The front end contains a Vero edge connector (part no. 2231-1) which provides the contact between the wire plane and the high voltage power supply. The connector, made of Diallyl Phthalate, has a capacitance between adjacent contacts of 1

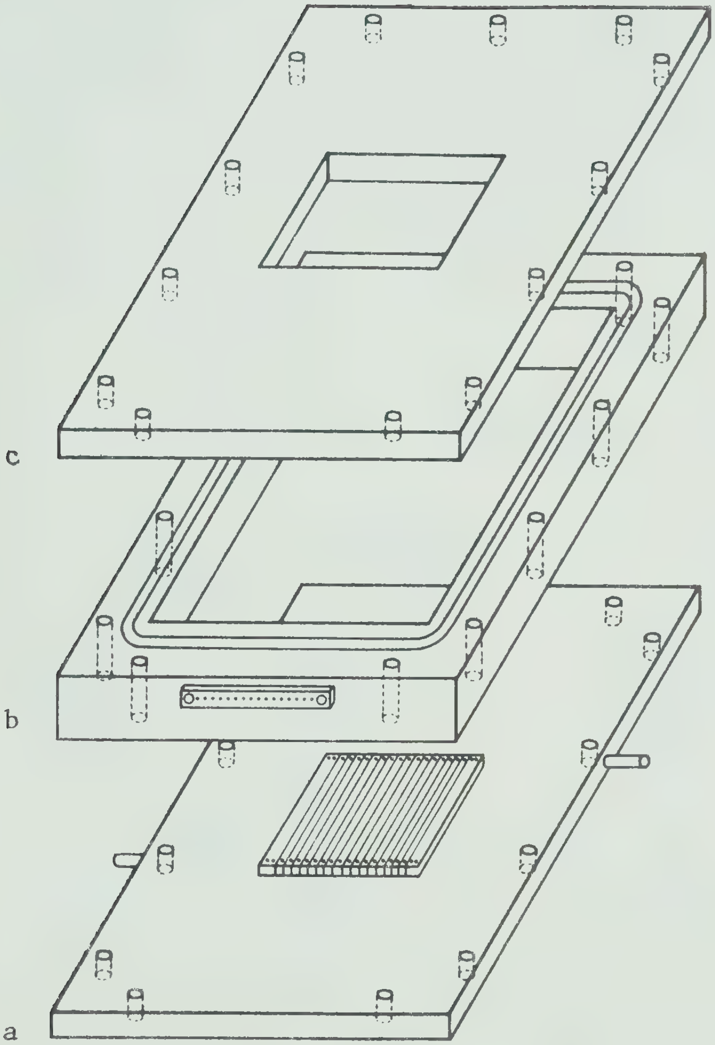

FIG. 4.2 Multiple detector: metallic frame.

pF; the proof voltage D.C. at sea level is given at 1,350V. The connector is attached to a high voltage network located in an isolated compartment of the unit housing the amplifier board and the encoding circuitry. Each anode wire is coupled through a 10 M-ohm resistor to a common power supply, as shown in Fig. 4.3. The 16 outputs, decoupled through 0.05 microfarad capacitors, C , are connected to the inputs of their respective amplifiers.

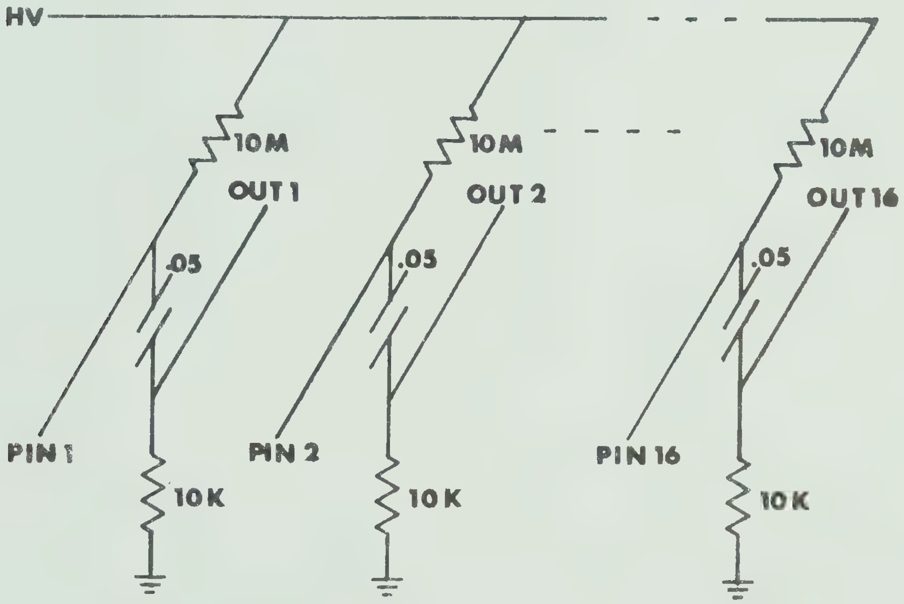

FIG. 4.3 High voltage network for the multiple detector.

The top section, (c), has a rectangular aperture for the 20 micrometres aluminized mylar counter window. The window is glued to the frame with Eccobond 60-L conductive adhesive to provide ground connection.

When the counter is assembled, the three sections are bolted together to achieve a gas tight compartment. The

metallic case is kept at ground potential and provides electrostatic shielding for the counter anode wires.

4.2.1 Fin characteristics

The main function of the fins is to delimit each counter volume and to prevent the ionizing radiation from penetrating more than one counter. They are metal strips of predetermined thickness, grounded by simple contact to the metallic case at the base of the counter which holds them in place. The fin thickness is determined by the energy of the radioactive source used in axoplasmic transport experiments, in our particular case, β-emitters whose maximum energy, E_m, varies from 0.154 MeV for ^{14}C to 1.71 MeV for ^{32}P. Nevertheless, their thickness must be kept as small as possible to prevent excessive screening of the nerve from the detector.

The absolute range of beta particles in a given absorber is not a well defined quantity. The experimental determination of range is not easily performed because the measurements are made at practically zero intensities. To estimate the maximum range, R_m, of some common β-sources, we used the empirical energy range relation obtained by Katz and Penfold[70],

$$R_m = 412\, E_m^2 \quad \mathrm{mg/cm^2} \qquad 4\text{-}2.1$$

where n = 1.265 - 0.0954 ln E_m. The maximum energy, E_m, is expressed in MeV, and the range is independent of the type of absorber. The above equation is valid for both monoenergetic electrons and continuous β-emitters, and holds true for energies between 0.01 - 2.5 MeV.

Table 4.1 gives the thickness in cm x 10^{-3} for various metal absorbers and different β-sources. The maximum range is obtained from equation 4-2.1 using the known E_m values for four common β-sources used in axoplasmic transport studies. It is obvious from the table that for sources with ranges less than or equal to that of ^{45}Ca, an Al fin of thickness 0.5mm would provide effective shielding between neighbouring wires. In addition, since the counter was devised with easily removable fins, it is possible to use the same detectors with a ^{32}P source merely by replacing the aluminum fins with tungsten fins of the same thickness.

4.2.2 Gas flow

One important aspect of the multiple counter which must be dealt with in detail is the gas flow. In detectors of the continuous flow type, the gas mixture must move uniformly throughout the counter. This allows for a proper washout of electronegative impurities such as O_2 , and maintains a uniform detection efficiency throughout the counter's active volume. The rate of flow of the gas mixture in each chamber should be such that even with a slight change in the flow rate, the detection effeciciency should remain unaltered.

TABLE 1

β^- source	Em (MeV)	Rm (mg/cm^2)	ABSORBER THICKNESS (cm x 10^{-3})							
			Al 2.702	Cr 7.20	Fe 7.86	Ni 3.90	Cu 8.92	Zn 7.14	W 19.35	Pb 11.34
^{14}C	0.154	27.68	10.2	3.84	3.52	3.11	3.10	3.88	1.43	2.44
^{35}S	0.167	31.54	11.7	4.38	4.01	3.54	3.54	4.42	1.63	2.78
^{45}C	0.254	60.84	22.5	0.45	7.74	6.84	6.82	8.52	3.14	5.37
^{32}P	1.71	790.2	292	110	101	88.8	88.6	111	40.8	69.6

Range of common β^--emitters in different metals. (Densities of the elements are given below their chemical symbols.)

The counter consists mainly of 16 compartments, each provided with an aperture at each end connected to the main gas lines. One line leads to a pressurized gas cylinder, containing the gas mixture of 93% argon and 7% carbon dioxide, via a single stage high pressure regulator and a flow meter. The second line is open to the atmosphere through a long narrow exhaust tube, which keeps the counter at a slightly elevated pressure, and causes a slight bulging of the thin counter window. The pressure gradient between the two ends of the long tube maintains an outflow of gas which in turn prevents an inflow of gas impurities.

The optimum flow rate of the gas through the multiple detector was determined by measuring the counting rate with respect to the total gas flow. The supporting electronics consisted of a Hamner NB-11 preamplifier and a Tennelec TC-205 amplifier with a total gain of about 1000. The amplified signal was fed into an ORTEC digital ratemeter (Model 434) through a Camberra SCA (Model 1431) with the upper window set to cover the whole spectrum. This arrangement of the recording system was used throughout in this section. Prior to any measurement, the detector was outgassed for several hours at a rate of 10 cc/min. Following each change in the flow rate, enough time was allowed for the flow to stabilize. Fig. 4.4 was obtained by placing a small ^{14}C source (about 1 mm in diameter) against the counter window, centered with respect to one particular channel. Each data point was obtained from a set of 5

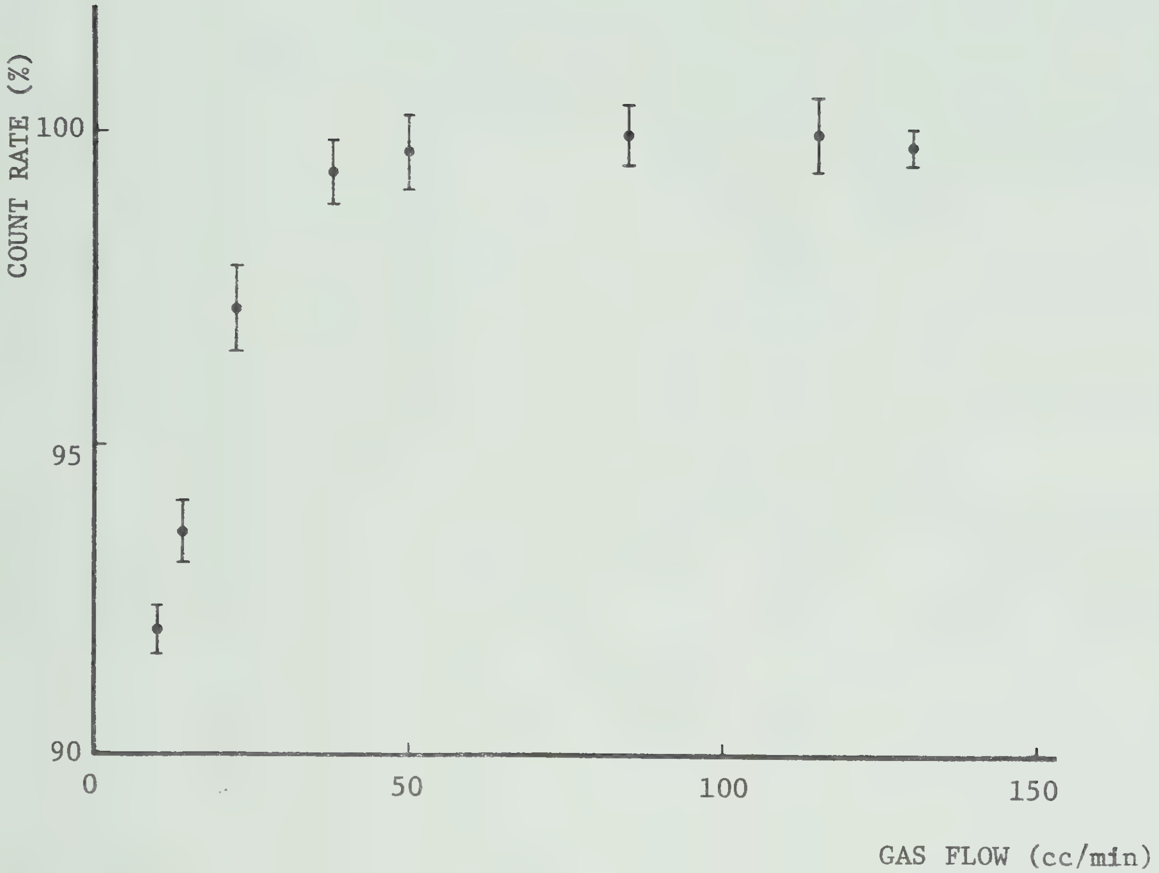

FIG. 4.4 Dependence of count rate with rate of gas flow.

independent measurements. The 100% level was set to correspond to the maximum mean count rate obtained from the group of measurements. The error bar associated with each data point gives the percentage standard deviation. Such deviations range from ±0.3% to ±0.7%.

Fixing the flow rate at the value of 80 cc/min, the ^{14}C source was moved along the axis of one single counter, thereby determining the detection uniformity in the longitudinal direction. Fig. 4.5 shows the dependence of the count rate on the position of the source with respect to the two gas apertures. The mean of the set of measurements was set at 100%. The dashed lines above and below the mean value mark 1% deviation from the mean.

The response of each of the 16 counters in the multiple detector to the β-source is shown in Fig. 4.6. Once again, the total gas flow rate was kept at 80 cc/min. The source was placed in contact with the window at the centre of each counter. Additional measurements were made at 5 mm from each end of the 16 counters. It was found that changes in count rate were within ±1% of the mean. As in Fig. 4.5, the dashed lines in Fig. 4.6 represent 1% deviation about the mean.

From the results shown in Fig. 4.5 and 4.6, one can conclude that the variation in detection due to gas flow is within an acceptable limit.

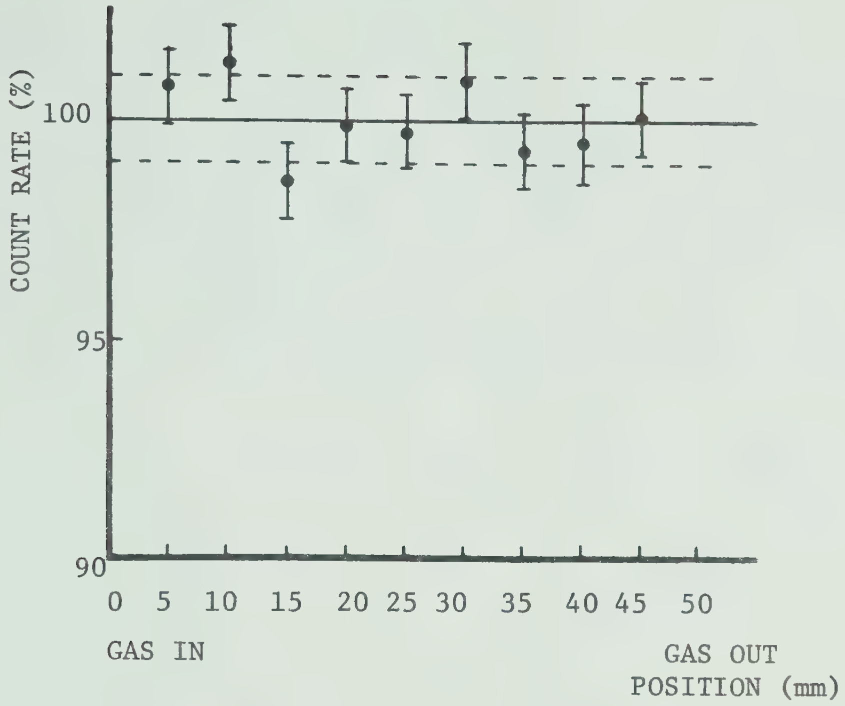

FIG. 4.5 Longitudinal variation in count rate

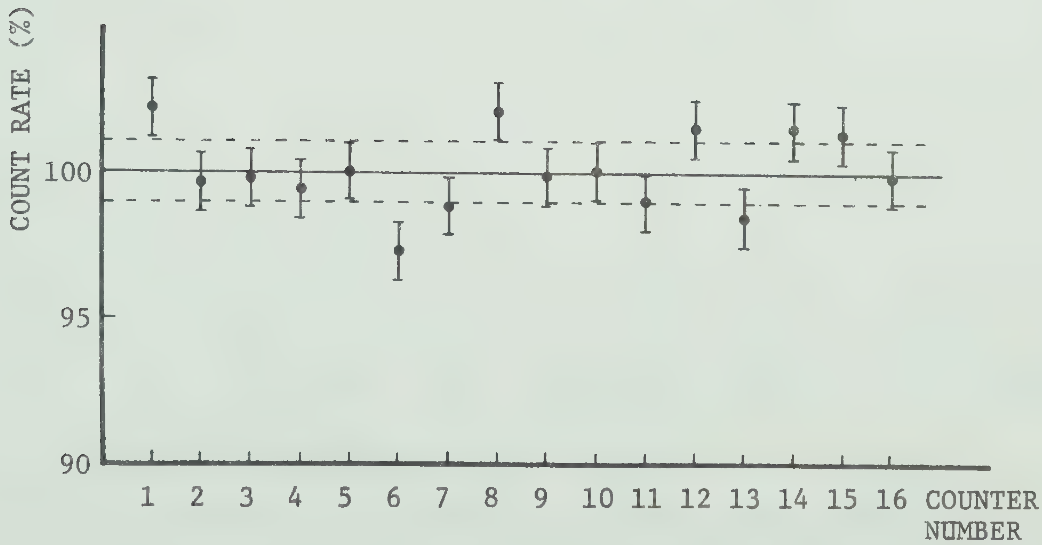

FIG 4.6 Response of the 16 counters to a ^{14}C source.

4.3 Read-out system

The most critical aspect of the read-out system is related to the low detection threshold. In detecting weakly ionizing radiation, such as β-particles, this threshold may correspond to no more than a few ion pairs. With good gas amplification, this would amount to only a few hundreds of microvolts.

Following the development of MWPC's Charpak et al.[71] described methods which could lead to simple and inexpensive read-out systems. Two of the techniques described by the authors are noteworthy because of the simplicity of the principle of operation which leads the way to more sophisticated methods: the lumped delay-line technique and the pulse division method. In the first of these, the wires are separated by inductances. The time difference between the arrival of the pulse at the opposite ends determines the wire carrying the signal. The pulse division method uses a purely resistive separation to produce a detectable pulse attenuation while preserving the pulse shape. To remove the effect of the spread in the initial pulse heights, the location of the wire is determined by the ratio of the pulses appearing at the opposing ends.

More recently, a method of reading the position of an ionizing event making use of commercially available delay lines was developed by Rindi et al.[72] and Grove et al.[73] The principle of operation is very much similar to the lumped delay line technique suggested by Charpak. The construction

and characteristics of an improved version of a delay-line has been given by Grove et al.[74]. In general, the positioning accuracy which can be achieved with these delay lines depends on the amplitide of the pulse above electronic noise and the polarity and spacing of the wire plane which is read-out. For the electron collecting plane the accuracy amounts to half the anode wire spacing. A negative aspect which makes the use of delay lines with our detecting system less attractive is the attenuation produced by the capacitative coupling between the wire plane and the delay line. For good delay lines a coupling efficiency of 18% has been reported[75].

In our read-out system we adopted the one amplifier per wire method; the amplifier, trigger and memory are described by Tarlé et al.[69]. One important reason for choosing this particular circuitry is the low voltage threshold of the amplifier and trigger, normally .5mV as reported by the authors. One practical aspect of the amplifier, trigger and memory circuit, in addition to the low cost, is that it amplifies the counter signal to a level which permits the handling and interpreting of the information with minimal additional electronics.

4.3.1 The amplifier

The amplifier used with our read-out system was originally designed by Tarlé et al. . It utilizes a Motorola MC 1035, an active element which contains three differential

amplifiers with emitter follower outputs. Fig. 4.7 gives the schematic diagram of the amplifier and logic circuitry. Boards containing 16 such units were obtained from the NRC of the U. of A. The logic circuitry had to be slightly modified to suit our needs. Minor changes were also introduced to the amplifier circuit to adjust the detection threshold above noise level and to reduce crosstalk between neighbouring units.

The first two stages of the active element (a,b) have a gain of approximately 72 and are connected as a preamplifier to the trigger circuit which makes use of the third stage (c). The trigger sensitivity can be adjusted by varying the standing current in the diode T_1 by altering R_{10}. To eliminate cross talk between neighbouring units, the diode current was set at 1.9 mA reducing the overall sensitivity of the amplifier to about 1 mV.

Associated with each amplifier and trigger we have a gate G(a) which, in its normal state is low, and a bistable memory M(b,c). The additional gate (d) is maintained open in our application. Such a gate could be implemented to read the state of the memory M by a pulse from the read-out logic along with the strobe and reset signal. The trigger output is differentiated and inverted by the transistor T_2. The pulse crosses gate G changing the state of the memory M. The outputs of the 16 bistables are "OR" tied in the encoder, which provides the strobe and reset pulses.

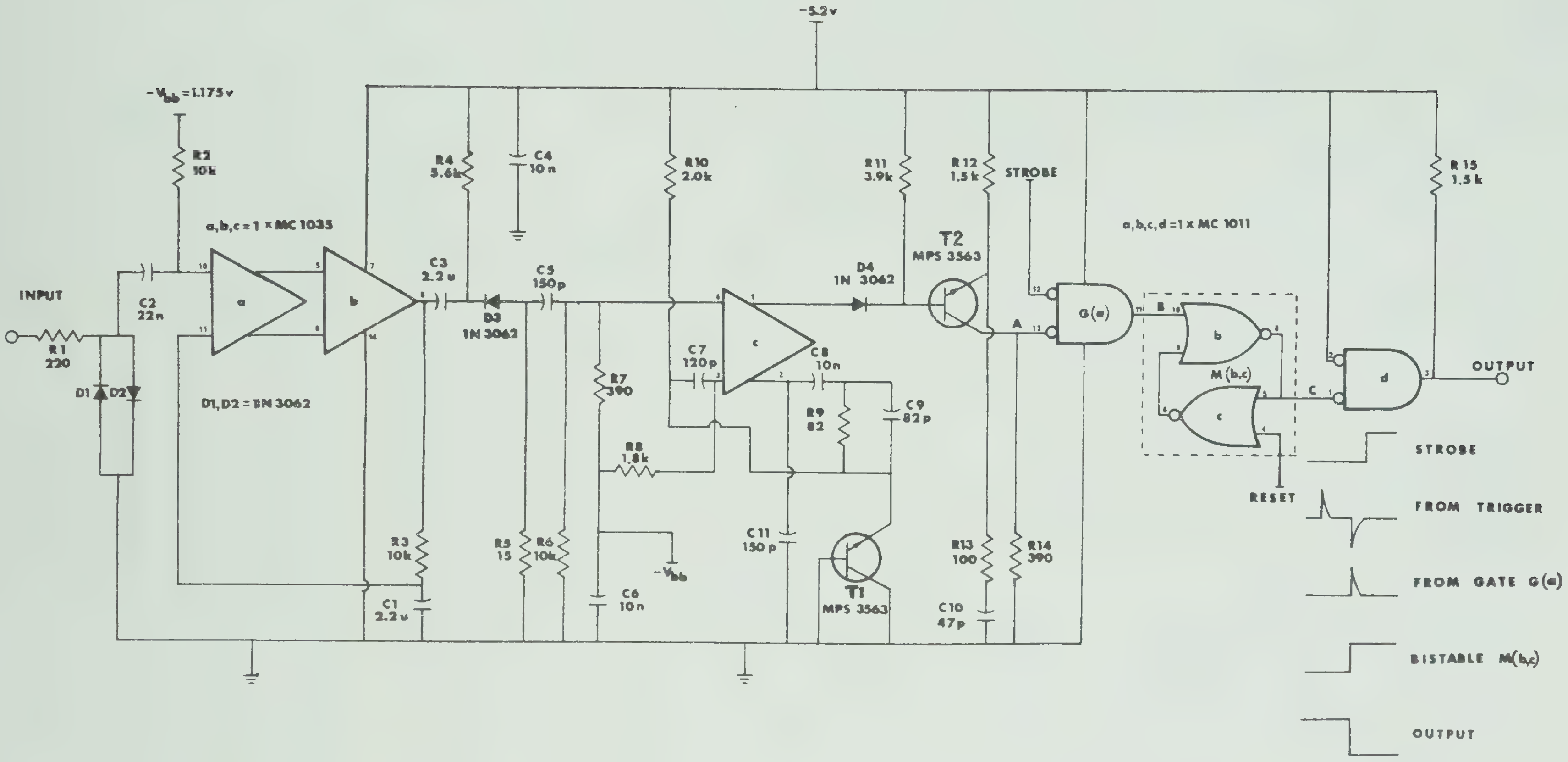

FIG. 4.7 Amplifier, trigger and memory. (After Tarle et.al.[69])

4.3.2 Encoding

The output of the logic circuitry associated with each amplifier is fed via an ECL-to-TTL level translator (MC 10125) into a Fairchild 9318 8-input priority encoder, to generate the address of the active input (Fig. 4.8). The priority encoder has eight active low inputs (I_0 - I_7) with highest priority assigned to I_7. The output ($A_0 A_1 A_2$) is a linearly weighted code representing the active element with highest priority. Thus, whenever more than one input is low, only the highest priority signal is encoded and the others neglected. The inputs are "OR" tied together to yield a group signal (GS) which indicates the presence of an active input. An enable input (EI) controls the state of all the inputs and overrides them. Whenever EI is high, all inputs are forced high, otherwise they can change state. The enable output EO stays high when EI is high or because one of the inputs is active low. The proper connection of EO - EI allows series or parallel expansion to larger systems. Fig. 4.8 shows a series expanded encoder as described in the Fairchild semiconductor application handbook[76] and used for the 16-wire chamber.

The time sequence of the signals which controls the MCA memory cycle and the outputs of the 16 logic circuits on the amplifier board is shown in Fig. 4.9. The sequence begins with the differentiated trigger output (DTO) at point A in Fig. 4.7. The strobe and reset signals are generated in the encoding circuit following the detection of an event. As

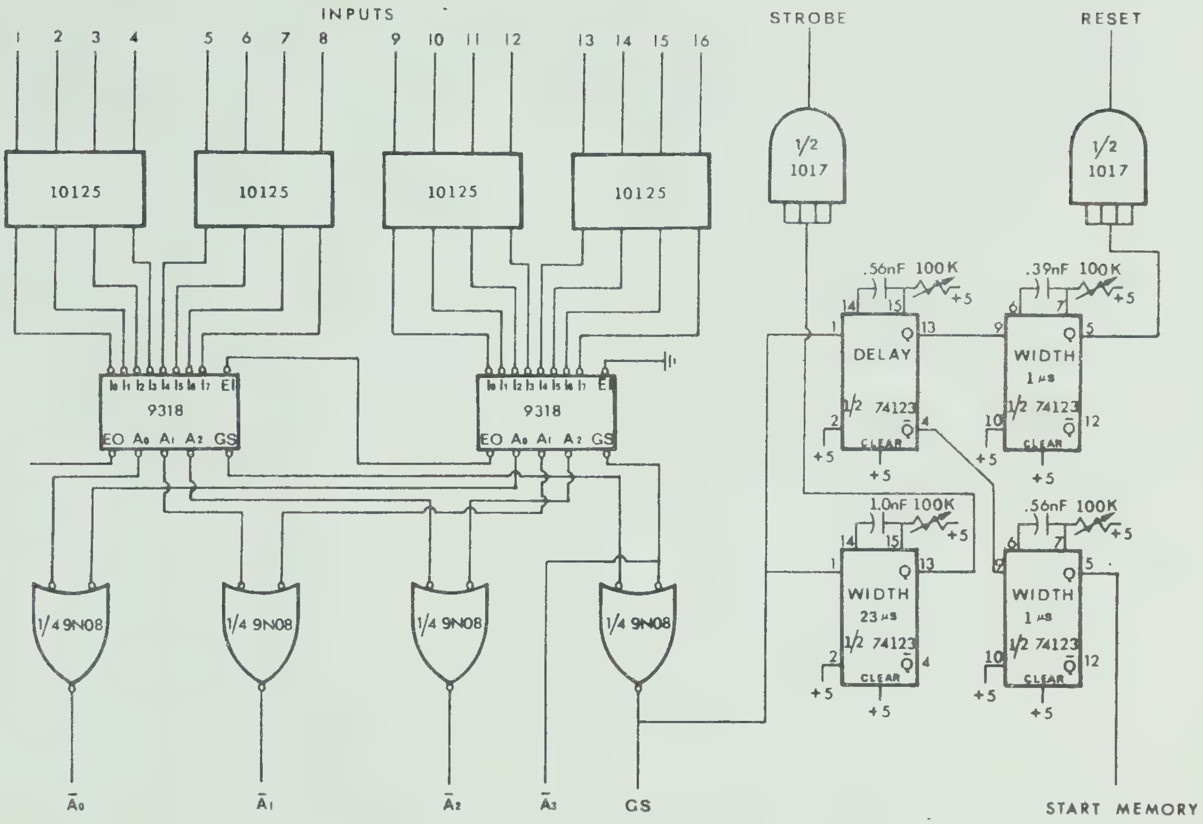

FIG. 4.8 Encoder with strobe, reset and start memory signals.

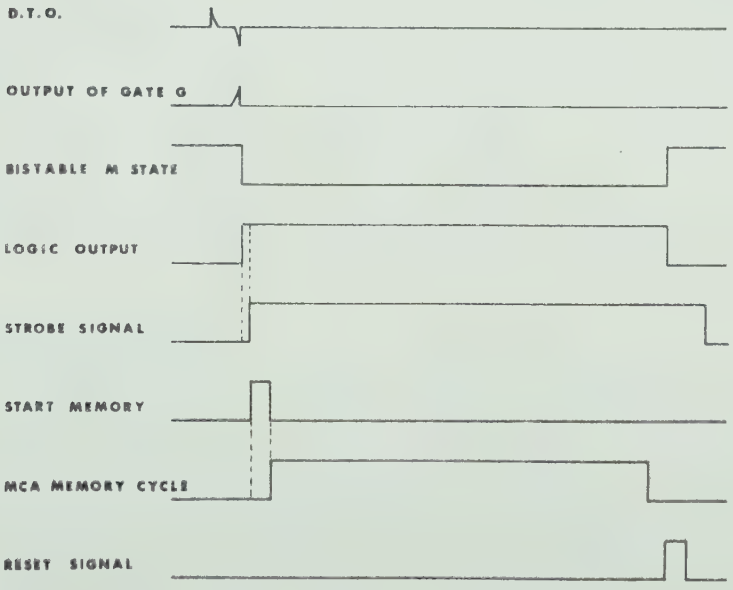

FIG. 4.9 Timing sequence of events.

shown in the schematics of Fig. 4.8, the encoder group signal (GS) is fed into a monostable multivibrator (1/2 of SN74123). The output of one yields the Strobe Signal which serves to block additional wires from being encoded until the initial event has been stored in the memory. The output $\overline{Q}$ of the second triggers the Start Memory command, while Q triggers the Reset Signal. The width of the Strobe Signal (24 microseconds) represents the dead time of the system; it is due mainly to the timing of the memory cycle. Translation from saturated logic to emitter coupled logic for both reset and strobe signal is accomplished with a MC 1017 as shown in Fig. 4.8.

The encoding system has the apparent disadvantage of a non linear response due to the priority scheme of its inputs, since given two simultaneous active inputs, only the one with the highest priority will be encoded. However, this non linearity may be seen to be negligible when the time spread between two simultaneous pulses, about 30 nanoseconds, is compared to the dead time of the system.

4.3.3 Data collection

The encoded signal is stored directly in the memory of an ORTEC 6240 MCA using the 5-bit word (GS $A_0 A_1 A_2 A_3$) . The GS bit, which is active for any input, is added to the encoded 4-bit word ($A_0 A_1 A_2 A_3$) to provide 16 odd numbered addresses from 1- to 31 in order that the 0 channel is reserved for timing purposes. The memory cycle is initiated

by the Start Memory Signal which is made available along with the encoded signal. The cycle itself lasts 20 microseconds: a read signal counts the level previously stored in the particular address, adds one count, then writes the revised count back into the memory. After the event has been recorded the system is ready to store the next event. The data collection capability is better than 40-K counts per second. The system was tested by simulating the counter pulse using a pulse generator which fed pulses into the input of the amplifier board at a repetition rate of about 35-K counts per second. The maximum error observed in the number of stored events over repeated measurements was less than 0.2%. Such rates, are very seldom achieved in the detection of labelled proteins movement along the nerve. However, the system could be used for other measurements such as thin layer chromatography, in which case such counting rates could be observed.

CHAPTER 5

RESULTS AND DISCUSSION

5.1 Experimental results

To demonstrate the intended applications of the system, two types of measurement were performed. In the first, the detector was used to record the activity distribution along the sciatic nerve of a frog (*Xenopus laevis*); in the second type of measurement, it was employed to determine the radiochemical purity of a [^{35}S]-Methionine source. Fixing the gas flow at 80 cc/min and the operating voltage at 1150 volts, the system was tested for counting efficiency and background. A ^{14}C source was placed against the detector window at the center of each of the 16 counters, after which the count rate was compared with the known activity of the same source. The average value of the efficiency measured in such a way was approximately 70%, with a maximum deviation of 5%. Background measurements for the 16 channels were slightly higher than expected and ranged between 4 - 8 cpm/channel.

In the first type of measurement, the nerve preparation (as described section 1.3) was incubated with 275 microcuries of [^{35}S]-Methionine and 2.5 ml of Ringer's solution placed in the spinal cord compartment (refer to Fig. 1.2). After an incubation period of approximately 18 hours, the nerve was severed 15-20 mm distal to the spinal

cord and immersed in fresh Ringer's solution in order to remove any soluble radioactive material which might have leaked from the spinal cord housing into the nerve compartment. The nerve was then laid in a tray containing Ringer's solution and gently pressed down, by coarse gauze stretched across a lightweight plastic frame, against 10 micrometre thick aluminized mylar. The tray was finally positioned on the detector. After the measurements, consisting of a set of three 2000-second runs, the nerve was removed from the tray and cut in small sections to correspond with each counter location. One additional measurement with the tray and Ringer's solution alone yielded the data for background correction. The nerve sections, placed in separate vials, were each dissolved in 1 ml of Protosol. Following the addition of 10 ml of Econofluor, the vials were dark adapted for several hours and counted in a Nuclear Chicago Mark I liquid scintillation counter. Quenching was uniform among the sections.

The histograms in Fig. 5.1 illustrate the activity distribution along the nerve as measured with the β-detector (Fig. 5.1a), obtained by using the last 30 minute run, and the analogous distribution obtained by liquid scintillation counting (Fig. 5.1b). The overall shape of the two histograms is similar, with the odd displacement in configuration from one channel to a neighbouring one. In the process of moving the nerve and sectioning it, there is some room for error. It is almost impossible to duplicate the

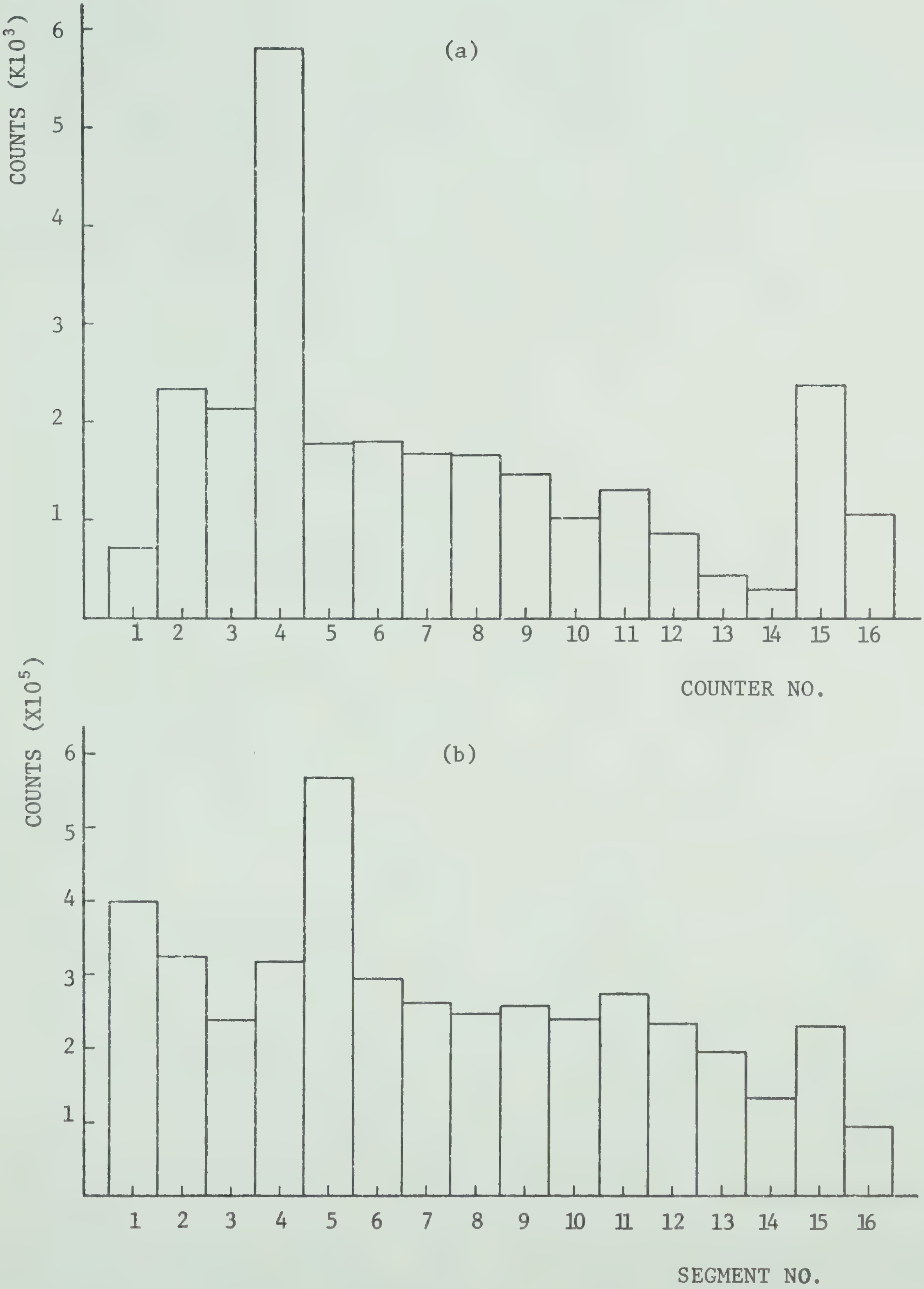

FIG. 5.1 Activity distribution in the nerve obtained with a) β -detector, (b) liquid scintillation counter. The total activity in (a) amounts to0.6% of (b).

relative position of the segments with respect to the multiple detector when the nerve is removed and segmented. This means that in some cases, liquid scintillation counting is being performed on a segment whose length has been changed (hence change in activity) or on one that does not correspond identically to its position in the detector. Therefore, the position of the nerve seen by any given channel may not be the same as seen in liquid scintillation counting. This would account for the displacement in the major peak of the two histograms in Fig. 5.1.

In the second type of measurement performed with the system, we tested the radiochemical purity of the β-emitter used in the nerve experiment, [^{35}S]-Methionine. A chromatographic separation was used which allows identification and quantification of the radiochemical inpurities present in the labelled amino acid. The principle employed in chromatography is based on the different migration velocities of the components of the sample in the mobile phase which is provided by the solvent. The stationary phase consists of an absorbent. Measurements were performed using a 10-cm strip of ITLC-SG chromatographic paper in a Seprachrom chamber both of which were manufactured by Gelman Instrument Company, together with a solvent whose composition of n-Butanol:NH_4OH:H_2O (30:1:2) achieved optimum separation of the radiochemicals. The chromatographic strip was first spotted with 1 microlitre of [^{35}S]-Methionine and then placed inside the Seprachrom

chamber containing the solvent. As the solvent rises through the medium by absorption and capillary action, the various chemical components will rise with different velocities. Methods of assaying the radioactivity distribution in the paper strip makes use of visual observation employing chromogenic compounds and of commercial radiochromatogram scanners.

Our system offers an alternate method for determining the activity distribution, which is achieved by placing the chromatographic strip against the detector window for any length of time. Fig. 5.2 shows a distribution in activity measured with the present detector. Point A in Fig. 5.2 denotes the origin, while D indicates the location of the solvent front. The peaks at B and C represent the impurity of Methionine sulfoxide and the Methionine respectively. The percentage of radiochemical purity (%RP) can be determined from the number of counts in peak B and peak C from the simple relation

$$\% \text{ RP} = 100 \times \frac{\text{counts peak C}}{\text{counts peak C} + \text{counts peak B}}$$

In the example shown, the radiochemical purity is 74%.

5.2 Discussion

The detection system described in chapter 4 was devised mainly for the study of axonal transport. It has been shown that the system can also be used in chromatographic

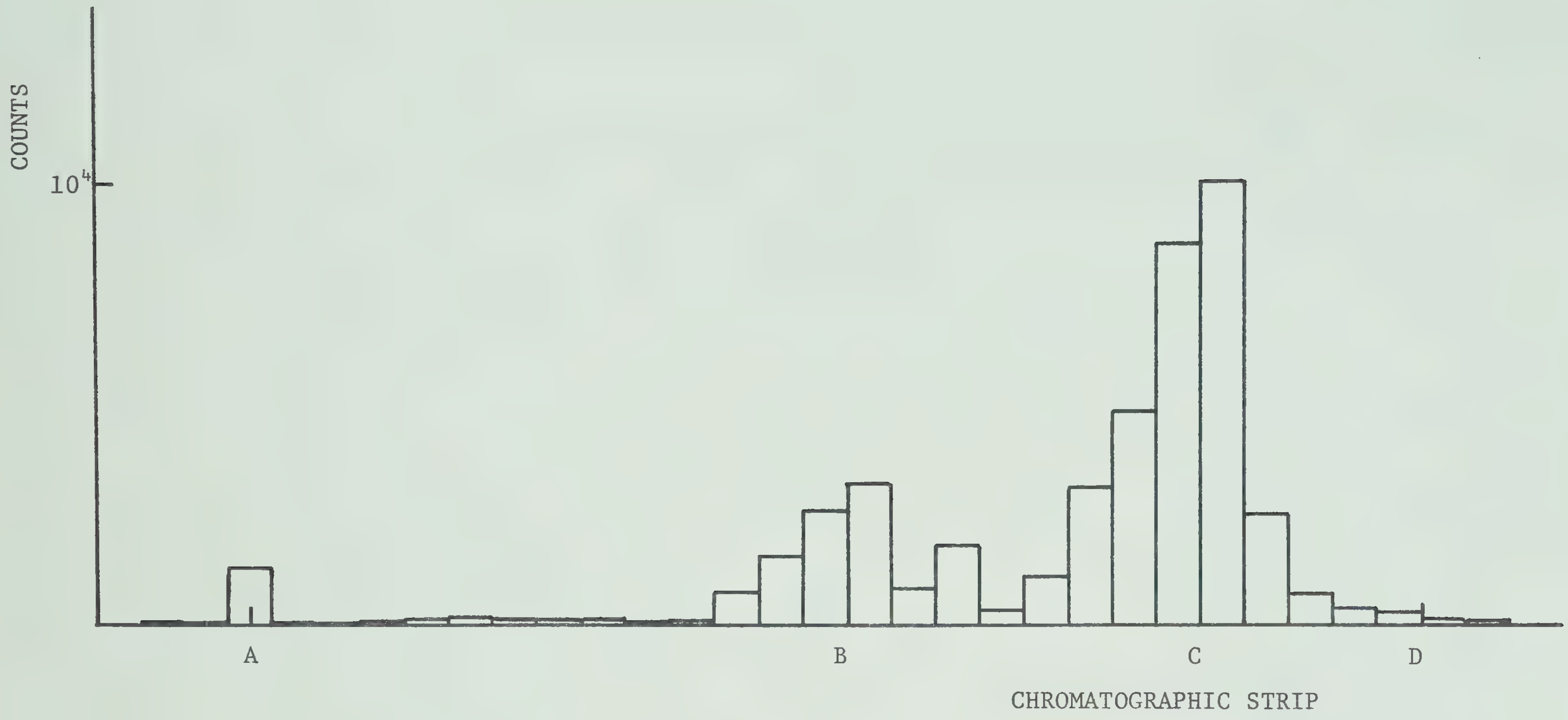

FIG. 5.2 Activity distribution in the chromatographic strip
The chromatographic strip was cut into two parts; the histogram is a composite picture.

determination of the radiochemical purity of labelled compounds. The detector can be easily assembled and allows for quick replacement of any part. The read-out system, adopting the one amplifier per wire and priority encoder, offers a simple method of extracting the information.

Because of the fact that the system is still in its development stage, there are still certain inherent difficulties that have to be dealt with, before the construction of a larger unit. Most significant of these is crosstalk, which originates in the amplifier and trigger circuit and in the connector used between the counter and the high voltage network. In the latter case, a connector with smaller capacitance between pins would suffice to eliminate such crosstalk. More troublesome, however, is that occurring between neighbouring units in the amplifier, trigger and memory board. Indications are that this crosstalk occurs at the trigger stage because of poor grounding between units. With the present system this source of crosstalk was greatly reduced by lowering the sensitivity of the trigger circuit; however, this was accompanied by a loss in detection efficiency. The crosstalk level between the 16 amplifier units, although reduced, remains at about 4-8%.

BIBLIOGRAPHY

1. P. Weiss and H.B. Hiscoe. J. Exptl. Zool. 107 p. 315, 1948.

2. B. Droz and C.P. LeBlond. J. Comp. Neurol. 121 p. 325, 1963.

3. L. Lubinska, Progr. Brain Res. 13 p. 1, 1964.

4. R.J. Lasek, Intern. Rev. Neurobiol. 13 p. 289, 1970.

5. A. Edstrom and H. Mattsson, J. Neurochem. 19 p. 205, 1972.

6. S. Ochs, Science 176 p. 252, 1972.

7. A.Edstrom and Hanson, Brain Research 58 p.345, 1973

8. R.E.Snyder, R.A. Reynolds, R.S. Smith and W.S. Kendal, Can. J. Physiol. Pharmac. 54, no.3, p. 238, 1976

9. A.P. Jeavons, G. Charpak and R.J. Stobbs. Nucl. Inst. and Meth. 124 p. 491, 1975.

10. J.M. Valentine and S.C. Curran. Average Energy expenditure per ion pair in gases and gas mixtures. Repts. Progr. in Phys. 21 p. 1, 1958.

11. G.N. Whyte. Radiat. Research 18 p. 265, 1963.

12. D.H. Wilkinson. Ionization chambers and counters. Cambridge University Press 1950

13. E. Rutherford and H. Geiger. Proc. Roy. Soc. 81 p. 141, 1908.

14. H. Geiger and O. Klemperer. Zeitz. F. Physik. 49 p. 753, 1928.

15. M.E. Rose and S.A. Korff. Phys. Rev. 59 p. 850, 1941.

16. R.W. Kiser. Appl. Sci. Res. 8 p. 183, 1960.

17. A. Zastawny. J. Sci. Instrum. 43 p. 179, 1966.

18. A. Williams and R.I. Sara. Int. J. Appl. Radit. Isotopes 13 p. 229, 1962.

19. M.W. Charles. J. Phys. E:Sci. Inst. 5 p. 95, 1972.

20. G. Charpak, R. Bouclier, T. Bressani, J. Favier and C. Zupancic. Nucl. Inst. and Meth. 62 p. 262, 1968

21. B. Rossi and H. Staub. Ionization Chambers and Counters, McGraw Hill, New York, p. 130, 1949.

22. P.J. Campion. Int. J. Appl. Radiat. Isotopes 19 p. 219, 1968.

23. P.J. Campion and M.W.J. Kingham. Int. J. Appl. Radiat. Isotopes 20 p. 479, 1969.

24. P.J. Campion. Nucl. Inst. and Meth. 112 p. 75, 1973.

25. M.W. Charles and B.A. Cooke. Nucl. Inst. and Meth. 61 p. 31, 1968.

26. J. Byrne, F. Shaikh, J. Kyles. Nucl. Inst. and Meth. 79 p. 286, 1970.

27. Harald Genz. Nucl. Inst. and Meth. 112 p. 83, 1973.

28. R. Bouchlier, G. Charpak, Z. Dimcovski, G. Fischer, R. Sauli, G. Coignet and G. Flugge. Nucl. Inst. and Meth. 88 p. 149, 1970.

29. R.G. Markham and R.G.H. Robertson. Nucl. Inst. and Meth. 129 p. 131, 1975

30. D. Jeanne, P. Lazeyras, I. Lehraus, R. Matthenson, W. Tejessy and M. Aderholz. Nucl. Inst. and Meth. 111 p. 287, 1973.

31. E. Beardsworth, J. Fischer, S. Iwata, M.J. Levine, V. Radeka and C.E. Thorn. Nucl. Inst. and Meth. 127 p. 29, 1975.

32. P. Deurdoth, R.J. Ellison, R.E.H. Jones, D. Mercer, B.V. Cake and D. Clarke. Nucl. Inst. and Meth. 129 p. 461, 1975.

33. L.J. Koester Jr., U. Koetz and S. Segler. Nucl. Inst. and Meth. 82 p. 67, 1970.

34. R.J. Semper, C. R. Guarnieri and J.C. Walker. Nucl. Inst. and Meth. 129 p. 447, 1975.

35. I. Lehraus and R. Matthenson. Nucl. Inst. and Meth. 97 p. 187, 1971.

36. C.J. Borkowski and M.K. Koop. IEEE Trans. Nucl. Sci. NS-17 no.1, p. 340, 1970.

37. S.N. Kaplan, L. Kaufman, V. Perez-Hendez and K. Valentine. Nucl. Inst. and Meth. 106 p. 397, 1973.

38. R.A.Reynolds, R.E. Snyder, T.R. Overton. Phys. Med. Biol. 20 p. 136, 1975.

39. C.B. Lim, D. Chu, L. Kaufman, V. Perez-Hendez, R. Hattner and D.C. Price. Lawrence Berkeley Lab. Report CBL-3617 University of California.

40. T. Tomitani and E. Tanaka. Health Phys. 18 p. 195, 1970.

41. D. Ramsden. Health Phys. 16 p. 145, 1969.

42. B. Taylor. Health Phys. 17 p. 59, 1969.

43. H. Tananbaum and E.M. Kellogg. IEEE. Trans. Nucl. Sci. NS-17 No. 1, p. 97, 1970.

44. J. Plch, J. Zderadicka and L. Kokta, Int. J. Appl. Radiat. Isotopes 24 p. 65, 1973.

45. H.S. Snyder. Phys. Rev. 72 p. 181, 1947.

46. S.C. Curran, A.L. Cockroft and J. Angus. Phil. Mag. 40 p. 929, 1949.

47. J.Byrne. Proc. Roy. Soc. Edinburgh 66A p. 33, 1962.

48. J.L. Cookson and T.J. Lewis. Brit. J. Appl. Phys. 17 p. 1473, 1966.

49. J. Byrne. Nucl. Inst. and Meth. 74 p. 291, 1969.

50. G.D. Alkhazov. Nucl Inst. and Meth. 89 p. 155, 1970.

51. H. Genz. Nucl. Inst. and Meth. 112 p. 83, 1973.

52. V. Fano. Phys. Rev. 72 p. 26, 1947.

53. G.D. Alkhazov, A.P. Komar and A.A. Vorobev. Nucl. Inst. and Meth. 48 p. 1, 1967.

54. G. Charpak, D. Rahm and A. Steiner. Nucl. Inst. and Meth. 80 p. 13, 1970.

55. C. Bemporad, W. Beusch, A.C. Melissinos, E. Schuller, P. Astbury and J.G. Lee. Nucl. Inst. and Meth. 80 p. 205, 1970.

56. G. Charpak. Ann. Rev. Nucl. Sci. 20 p. 195, 1970.

57. G. Charpak, G. Fischer, A. Minten, L. Naumann, F. Sauli, G. Flugge, C.H. Gottfried and R. Tirler. Nucl. Inst. and Meth. 97 p. 377, 1971.

58. J.L. Lacy and R.S. Lindsey. Nucl. Inst. and Meth. 119 p. 483, 1974.

59. C. Grunberg, L. Cohen and L. Mathieu. Nucl. Inst. and Meth. 78 p. 102, 1970.

60. T. Trippe. CERN NP Internal Report, 69-18, 1969.

61. Z. Dimcovski. CERN NP Internal Report 70-16, 1970.

62. T. Tomitani. Nucl. Inst. and Meth. 100 p. 179, 1972.

63. K.M. Urbanczyk and M.P.R. Waligorski. Nucl. Inst. and Meth. 124 p. 413, 1975.

64. M.A. Jaswon. Proc. Roy. Soc.(A) 275 p.23, 1963.

65. G.T. Symm. Nucl. Inst. and Meth. 118 p. 605, 1974.

66. I.T. Myers. Rad. Dosimetry Second Edition, Vol. 1, p. 317, Frank H. Attix, W.C. Roesch.

67. R.Gott and M.W. Charles. Nucl. Inst. and Meth. 72 p. 157, 1969.

68. C.D. Kemshall, K.G. Beauchamp and P.W. Benjamin. Nucl. Inst. and Meth. 68 p. 153, 1969.

69. J.C. Tarle and H. Verweij. Nucl. Inst. and Meth. 78 p. 93, 1970.

70. L. Katz and A.S. Penfold. Rev. Modern Phys. 22 p. 36, 1950.

71. G. Charpak, R. Bouclier, T. Bressani, J. Favier and C. Zupancic. Nucl. Inst. and Meth. 65 p. 217, 1968.

72. A. Rindi, V. Perez-Mendez and R.I. Wallace. Nucl. Inst. and Meth. 77 p. 325, 1970.

73. R. Grove, K. Lee, V. Perez-Mendez and J. Speridine. Nucl. Inst. and Meth. 89 p. 257, 1970.

74. R. Grove, I. Ko, B. Leskovar, V. Perez-Mendez. Nucl. Inst. and Meth. 99 p. 381, 1972.

75. V. Perez-Mendez and S.I. Parker. IEEE Trans. Nucl. Sci. NS-21 No. 1, p. 45, 1974.

76. Fairchild Semiconductor, The TTL Application Handbook, p. 4-3, 1973.

APPENDIX A

A.1 Introduction

The proportional counter of rectangular geometry consists simply of a central electrode of circular cross section enclosed in a long hollow rectangular metal box usually kept at ground potential. The counter cross section is assumed to be small compared to the counter length so that the potential satisfies Laplace's equations in two dimension.

The analytical solution has been given by Tomitani[62] using the method of conformal transformation by means of elliptic sine functions. With such a technique one obtains the solution to the electrostatic problem both for a single anode and for a series of anodes placed periodically within the cathode, and is applicable to those problems which have periodicity in two directions.

For anode-cathode arrangements which are not symmetrical, a numerical approach is advantageous as compared to this type of analytical approach. This permits application to more complex anode-cathode configurations. One such numerical method makes use of Fredholm's first integral equation to solve the boundary value problem[64].

A.2 Method

The axial symmetry of the counter reduces the electrostatic problems to a two-dimensional one. Assume the

following:

L is the outer boundary delimited by the counter,

R is the radius of the anode wire,

D is the domain bounded externally by the counter (cathode) and internally by the anode, and

V is the potential on the anode.

In addition, it is assumed that R is small compared to the counter dimensions . In such a counter, the electrostatic potential, ϕ , in D satisfies the two-dimensional Laplace equation

$$\nabla^2 \phi \equiv \frac{\partial^2\phi}{\partial x} + \frac{\partial^2\phi}{\partial y} = 0 \qquad \text{A.1}$$

with the boundary conditions

$$\phi(x,y) = \begin{cases} 0 & \text{on L} \\ V_a & \text{on the anode surface} \end{cases}$$

Equation A.1 may be rewritten in integral form as[65]

$$\phi(\vec{P}) = \int_L \phi(\vec{q}) \log \left|\vec{q} - \vec{p}\right| dq + A \log \left|\vec{P} - \vec{W}\right| , \qquad \text{A.2}$$

where the integral is taken over the boundary L, $\vec{p}$ is the position vector of a point within D, $\vec{q}$ is the position vector of a point on L, and $\vec{w}$ is the position vector of the centre of the anode. The problem is solved by determining

$\sigma(\vec{q})$, the charge density on L , and the constant A. Imposing the boundary condition on L, i.e.

$$\phi(\vec{p}) = 0$$

equation A.2 yields

$$\int_L \sigma(\vec{q}) \log \left|\vec{q} - \vec{p}\right| dq + A \log \left|\vec{p} - \vec{w}\right| = 0 \qquad \text{A.3}$$

for $\vec{p}$ on the boundary L. The second boundary condition, on the anode surface, becomes

$$\int_L \sigma(\vec{q}) \log \left|\vec{p} - \vec{w}\right| dq + A \log R = V_a = 1 \qquad \text{A.4}$$

The replacement $V_a = 1$ is to simplify the calculations. Equations A.3 and A.4 have to be solved simultaneously for $\sigma(\vec{q})$ and A.

Consider now a rectangular counter as in Fig A.1. The boundary L is defined by the path OABCO; L is divided into n segments, each having a charge distribution σj (j=1,...,n). If the segments are small enough, it may be assumed that σ_j is constant on each segment. The integral over L (in equation A.3) can then be replaced by a sum of terms,

$$\sum_{j=1}^{n} \sigma_j \int_j \log \left|\vec{q} - \vec{q}_i\right| dq + A \log \left|\vec{q}_i - \vec{w}\right| = 0 \qquad \text{A.5}$$

for i=1,...,n. For n intervals (or segments), there will be n linear equations.

On the anode surface (equation A.4), a similar approach yields the following

$$\sum_{j=1}^{n} \sigma_j \int_j \log \left|\vec{q} - \vec{w}\right| dq + A \log R = 1 \qquad \text{A.6}$$

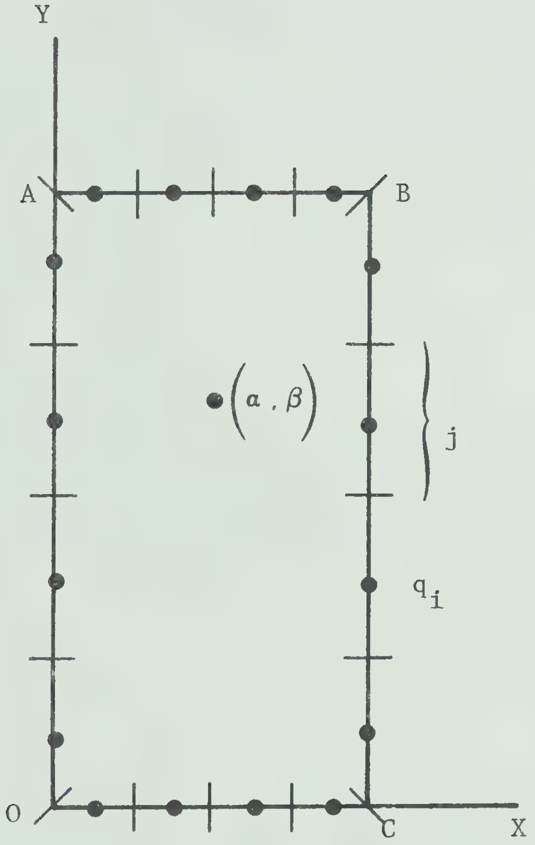

FIG. A.1 Rectangular counter with anode at (α, β).

Equations A.5 and A.6 form a set of (n + 1) simultaneous equations in the (n + 1) unknowns σj and A. The solution to the Laplace equation then becomes

$$\phi^n (\vec{p}) = \sum_{j=1}^{n} \sigma_j \int_j \log \left| \vec{q} - \vec{p} \right| dq + A \log \left| \vec{p} - \vec{w} \right| , \quad A.7$$

where n indicates the number of segments. The approximation of ϕ (p) (Equation A.2) by ϕ^n(p) becomes more reliable with increasing n.

A.3 Results

The potential $\phi^n(\vec{p})$ is obtained by first solving equations (A.5) and (A.6) simultaneously. The solutions σj and A are then substituted into equation (A.7) to yield $\phi^n(\vec{p})$. This whole procedure is done utilizing the computer program MAT. The solutions $\phi^n(\vec{p})$ are then plotted as equipotentials, varying from 5% to 60% of anode voltage, in increments of 5% (or, with Va = 1, from 0.05 to 0.6 in increments of 0.05). The computing was done on the University of Alterta Amdahl 470-V6 computing facility. The numerical values for $\phi^n(\vec{p})$ were contour plotted using the Calcompq plotter. A listing of the entire computer program follows in the next section.

Results from two counter configurations were obtained. These particular configurations were chosen so as to enable comparison with the results of Tomitani. The equipotentials obtained in this manner, for a square counter, are shown in

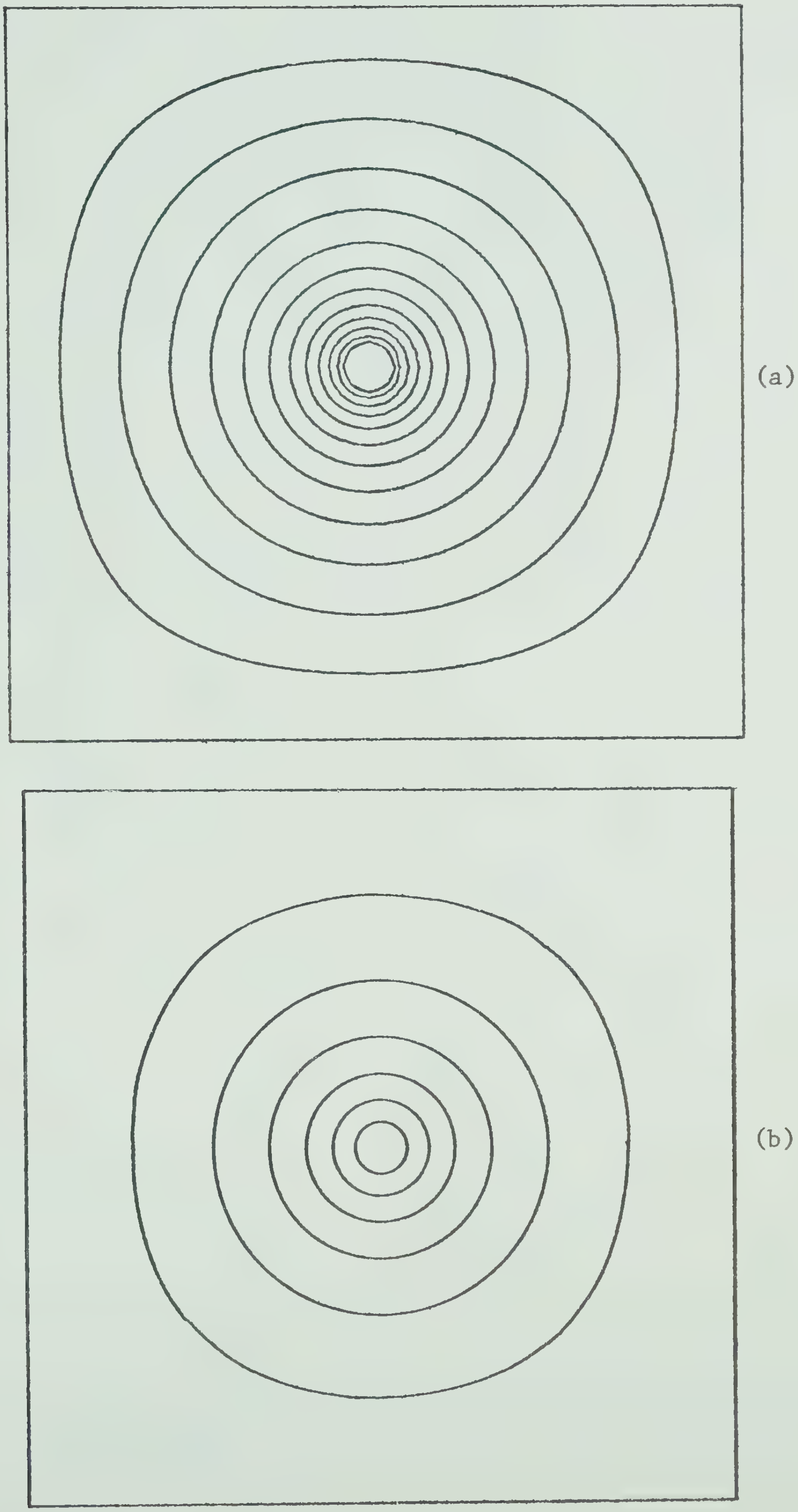

FIG. A.2 Square counter. Equiportential lines obtained a) with numerical technique b) with exact solution up to 30% of anode voltage.

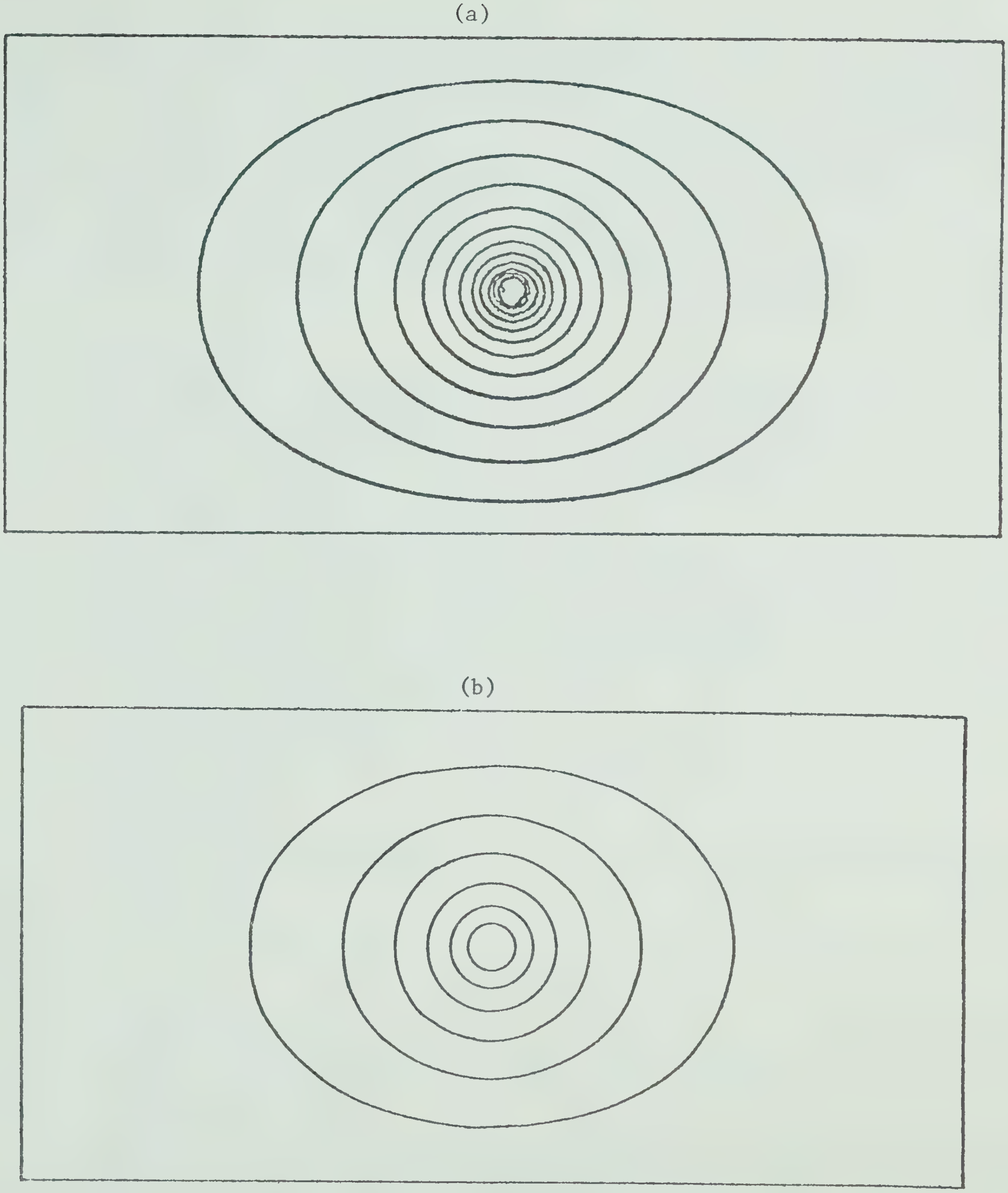

FIG. A.3 Rectangular counter. Equipotential lines obtained a) with numerical technique b) with exact solution up to 30% of anode voltage.

Fig. A.2, along with analogous results using the exact analytical method. A similar comparison for a rectangular counter is demonstrated in Fig. A.3. These results show that the differences between equipotential lines, in the two techniques, become smaller near the cathode.

A.4 Program "MAT"

```
       DIMENSION A1(20,20),A2(20,20),A3(20,20),B1(20,20)
      DIMENSION DD1(21,21),DD2(21,21),DD3(21,21),ADD1(21,21)
      DIMENSION ADD2(21,21),ADD3(21,21),ADD4(21,21)
      DIMENSION AD1(21,21),AD2(21,21),AD3(21,21)
      DIMENSION AD4(21,21),D1(21,21),D2(21,21),D3(21,21)
      DIMENSION D4(21),D5(21),DD5(21)
      DIMENSION C1(20,20),C2(20,20),C3(20,20),AA1(20,20)
      DIMENSION AA2(20,20),BB2(20,20),CC2(20,20),AA3(20,20)
      DIMENSION AB(81,81),B2(20,20),B3(20,20),BB1(20,20)
      DIMENSION CC1(20,20),BB3(20,20),CC3(20,20)
      DIMENSION A4(20),B4(20),C4(20),A5(20),B5(20),C5(20)
      DIMENSION AA5(20),BB5(20),CC5(20)
      DIMENSION VR(65),MA(65,65)
      DIMENSION CM(50,50),CVAL(12),IOP(7),VOP(7)
      DATA CVAL/12*0.0/,IOP/7*0/,CM/2500*0.0/
      REAL L,LL,MA
      WRITE(6,10)
10    FORMAT('ENTER VALUES OF L,LL,RX,RY(=LOCATION OF ANODE)'
      READ(5,20) L,LL,RX,RY
20    FORMAT(F6.4)
C
C     ANODE RADIUS
C
      R=0.01016
      WRITE(6,30)
30    FORMAT('ENTER VALUES OF N,JR, N=16 JR=1')
      READ(5,40) N,JR
40    FORMAT(2I3)
      M=JR*N
      NN=N+1
      DO 100 I=1,NN
      DO 200 K=1,N
      J=I-1
      A=FLOAT(J)*L/FLOAT(N)-FLOAT(2*K-1)*L/FLOAT(2*N)
200   A1(K,I)=A*ALOG(ABS(A))-A
100   CONTINUE
      MM=M+1
      DO 110 I=1,MM
      DO 210 K=1,N
      J=I-1
```

```
      B=L-FLOAT(2*K-1)*L/FLOAT(2*N)
      C=FLOAT(J)*LL/FLOAT(M)
210   B1(K,I)=C/2*ALOG(B**2+C**2)-C+B*ATAN(C/B)
110    CONTINUE
      NN=N+1
      DO 120 I2=1,NN
      I=NN+1-I2
      DO 220 K=1,N
      J=I-1
      D=FLOAT(J)*L/FLOAT(N)-FLOAT(2*K-1)*L/FLOAT(2*N)
220   C1(K,I)=D/2.0*ALOG(D**2+LL**2)-D+LL*ATAN(D/LL)
120   CONTINUE
      MM=M+1
      DO 1006 I2=1,MM
      I=MM+1-I2
      DO 1007 K=1,N
      J=I-1
      A=FLOAT(J)*LL/FLOAT(M)
      B=FLOAT(2*K-1)*L/FLOAT(2*N)
1007  D1(K,I)=A/2*ALOG(B**2+A**2)-A+B*ATAN(A/B)
1006  CONTINUE
      NN=N+1
      DO 300 I=1,NN
      DO 400 K=1,M
      J=I-1
      A=FLOAT(J)*L/FLOAT(N)-L
      B=FLOAT(2*K-1)*LL/FLOAT(2*M)
400   A2(K,I)=A/2.0*ALOG(A**2+B**2)-A+B*ATAN(A/B)
300   CONTINUE
      MM=M+1
      DO 310 I=1,MM
      DO 410 K=1,M
      J=I-1
      A=FLOAT(J)*LL/FLOAT(M)-FLOAT(2*K-1)*LL/FLOAT(2*M)
410   B2(K,I)=A*ALOG(ABS(A))-A
310   CONTINUE
      NN=N+1
      DO 320 I2=1,NN
      I=NN+1-I2
      DO 420 K=1,M
      J=I-1
      A=FLOAT(J)*L/FLOAT(N)-L
      B=LL-FLOAT(2*K-1)*LL/FLOAT(2*M)
420   C2(K,I)=A/2.0*ALOG(A**2+B**2)-A+B*ATAN(A/B)
320   CONTINUE
      MM=M+1
      DO 1008 I2=1,MM
      I=MM+1-I2
      DO 1009 K=1,M
      J=I-1
      A=FLOAT(J)*LL/FLOAT(M)-FLOAT(2*K-1)*LL/FLOAT(2*M)
1009  D2(K,I)=A/2*ALOG(A**2+L**2)-A+L*ATAN(A/L)
1008  CONTINUE
```

```
      NN=N+1
      DO 500 I=1,NN
      DO 600 K2=1,N
      K=N+1-K2
      J=I-1
      D=FLOAT(J)*L/FLOAT(N)-FLOAT(2*K-1)*L/FLOAT(2*N)
600   A3(K,I)=D/2.0*ALOG(D**2+LL**2)-D+LL*ATAN(D/LL)
500   CONTINUE
      MM=M+1
      DO 510 I=1,MM
      DO 610 K2=1,N
      K=N+1-K2
      J=I-1
      A=FLOAT(J)*LL/FLOAT(M)-LL
      B=L-FLOAT(2*K-1)*L/FLOAT(2*N)
610   B3(K,I)=A/2.0*ALOG(A**2+B**2)-A+B*ATAN(A/B)
510   CONTINUE
      NN=N+1
      DO 520 I2=1,NN
      I=NN+1-I2
      DO 620 K2=1,N
      K=N+1-K2
      J=I-1
      A=FLOAT(J)*L/FLOAT(N)-FLOAT(2*K-1)*L/FLOAT(2*N)
620   C3(K,I)=A*ALOG(ABS(A))-A
520   CONTINUE
      MM=M+1
      DO 1010 I2=1,MM
      I=MM+1-I2
      DO 1011 K2=1,N
      K=N+1-K2
      J=I-1
      A=FLOAT(J)*LL/FLOAT(M)-LL
      B=FLOAT(2*K-1)*L/FLOAT(2*N)
1011  D3(K,I)=A/2*ALOG(A**2+B**2)-A+B*ATAN(A/B)
1010  CONTINUE
      NN=N+1
      DO 1012 I=1,NN
      DO 1013 K2=1,M
      J=I-1
      K=M+1-K2
      A=FLOAT(J)*L/FLOAT(N)
      B=FLOAT(2*K-1)*LL/FLOAT(2*M)
1013  AD1(K,I)=A/2*ALOG(A**2+B**2)-A+B*ATAN(A/B)
1012  CONTINUE
      MM=M+1
      DO 1014 I=1,MM
      DO 1015 K2=1,M
      J=I-1
      K=M+1-K2
      A=FLOAT(J)*LL/FLOAT(M)
      B=FLOAT(2*K-1)*LL/FLOAT(2*M)
      ZEN=ATAN((A-B)/L)
```

```
1015   AD2(K,I)=(A-B)/2*ALOG(L**2+(A-B)**2)-(A-B)+L*ZEN
1014   CONTINUE
       NN=N+1
       DO 1016 I2=1,NN
       I=NN+1-I2
       DO 1017 K2=1,M
       K=M+1-K2
       J=I-1
       A=FLOAT(J)*L/FLOAT(N)
       B=LL-FLOAT(2*K-1)*LL/FLOAT(2*M)
1017   AD3(K,I)=A/2*ALOG(A**2+B**2)-A+B*ATAN(A/B)
1016   CONTINUE
       MM=M+1
       DO 1018 I2=1,MM
       I=MM+1-I2
       DO 1019 K2=1,M
       K=M+1-K2
       J=I-1
       A=FLOAT(J)*LL/FLOAT(M)
       B=FLOAT(2*K-1)*LL/FLOAT(2*M)
1019   AD4(K,I)=(A-B)*ALOG(ABS(A-B))-(A-B)
1018   CONTINUE
       DO 201 K=1,N
       DO 101 I=1,N
       J=I+1
       AA1(K,I)=A1(K,J)-A1(K,I)
101    CONTINUE
201    CONTINUE
       DO 811 I=1,N
       DO 812 J=1,N
812    CONTINUE
811    CONTINUE
       DO 211 K=1,N
       DO 111 I=1,M
       J=I+1
111    BB1(K,I)=B1(K,J)-B1(K,I)
211    CONTINUE
       DO 221 K=1,N
       DO 121 I=1,N
       J=N+2-I
       JJ=N+1-I
121    CC1(K,I)=C1(K,J)-C1(K,JJ)
221    CONTINUE
       DO 1020 K=1,N
       DO 1021 I=1,M
       J=M+2-I
       JJ=M+1-I
1021   DD1(K,I)=D1(K,J)-D1(K,JJ)
1020   CONTINUE
       DO 401 K=1,M
       DO 301 I=1,N
       J=I+1
       AA2(K,I)=A2(K,J)-A2(K,I)
```

```
301    CONTINUE
401    CONTINUE
       DO 411 K=1,M
       DO 311 I=1,M
       J=I+1
311    BB2(K,I)=B2(K,J)-B2(K,I)
411    CONTINUE
       DO 421 K=1,M
       DO 321 I=1,N
       J=N+2-I
       JJ=N+1-I
321    CC2(K,I)=C2(K,J)-C2(K,JJ)
421    CONTINUE
       DO 1022 K=1,M
       DO 1023 I=1,M
       J=M+2-I
       JJ=M+1-I
1023   DD2(K,I)=D2(K,J)-D2(K,JJ)
1022   CONTINUE
       DO 601 K=1,N
       KK=N+1-K
       DO 501 I=1,N
       J=I+1
501    AA3(K,I)=A3(KK,J)-A3(KK,I)
601    CONTINUE
       DO 611 K=1,N
       KK=N+1-K
       DO 511 I=1,M
       J=I+1
511    BB3(K,I)=B3(KK,J)-B3(KK,I)
611    CONTINUE
       DO 621 K=1,N
       KK=N+1-K
       DO 521 I=1,N
       J=N+2-I
       JJ=N+1-I
521    CC3(K,I)=C3(KK,J)-C3(KK,JJ)
621    CONTINUE
       DO 1024 K=1,N
       J=N+1-K
       DO 1025 I=1,M
       JJ=M+2-I
       JJJ=M+1-I
1025   DD3(K,I)=D3(J,JJ)-D3(J,JJJ)
1024   CONTINUE
       DO 1026 K=1,M
       J=M+1-K
       DO 1027 I=1,N
       JJ=I+1
1027   ADD1(K,I)=AD1(J,JJ)-AD1(J,I)
1026   CONTINUE
       DO 1028 K=1,M
       J=M+1-K
```

```
      DO 1029 I=1,M
      JJ=I+1
1029  ADD2(K,I)=AD2(J,JJ)-AD2(J,I)
1028  CONTINUE
      DO 1030 K=1,M
      J=M+1-K
      DO 1031 I=1,N
      JJ=N+2-I
      JJJ=N+1-I
1031  ADD3(K,I)=AD3(J,JJ)-AD3(J,JJJ)
1030  CONTINUE
      DO 1032 K=1,M
      J=M+1-K
      DO 1033 I=1,M
      JJ=M+2-I
      JJJ=M+1-I
1033  ADD4(K,I)=AD4(J,JJ)-AD4(J,JJJ)
1032  CONTINUE
      DO 250 I=1,N
      DO 251 J=1,N
251   AB(I,J)=AA1(I,J)
      DO 252 J=1,M
252   AB(I,J+N)=BB1(I,J)
      DO 253 J=1,N
253   AB(I,J+N+M)=CC1(I,J)
      DO 1035 J=1,M
1035  AB(I,J+N+M+N)=DD1(I,J)
250   CONTINUE
      DO 260 I=1,M
      DO 261 J=1,N
261   AB(N+I,J)=AA2(I,J)
      DO 262 J=1,M
262   AB(N+I,J+N)=BB2(I,J)
      DO 263 J=1,N
263   AB(N+I,J+N+M)=CC2(I,J)
      DO 1034 J=1,M
1034  AB(N+I,J+N+M+N)=DD2(I,J)
260   CONTINUE
      DO 270 I=1,N
      DO 271 J=1,N
271   AB(N+M+I,J)=AA3(I,J)
      DO 272 J=1,M
272   AB(N+M+I,J+N)=BB3(I,J)
      DO 273 J=1,N
273   AB(N+M+I,J+N+M)=CC3(I,J)
      DO 1036 J=1,M
1036  AB(N+M+I,J+N+M+N)=DD3(I,J)
270   CONTINUE
      DO 1037 I=1,M
      DO 1038 J=1,N
1038  AB(N+M+N+I,J)=ADD1(I,J)
      DO 1039 J=1,M
1039  AB(N+M+N+I,N+J)=ADD2(I,J)
```

```
      DO 1040 J=1,N
1040  AB(N+M+N+I,N+M+J)=ADD3(I,J)
      DO 1041 J=1,M
1041  AB(N+M+N+I,N+M+N+J)=ADD4(I,J)
1037  CONTINUE
      AL=RX*L
      ALL=RY*LL
      DO 777 I=1,N
      A=FLOAT(2*I-1)*L/FLOAT(2*N)
777   A4(I)=0.5*ALOG((A-AL)**2+ALL**2)
      DO 888 I=1,M
      A=FLOAT(2*I-1)*LL/FLOAT(2*M)-ALL
888   B4(I)=0.5*ALOG((L-AL)**2+A**2)
      DO 999 I=1,N
      J=N+1-I
      A=FLOAT(2*J-1)*L/FLOAT(2*N)
999   C4(I)=0.5*ALOG((A-AL)**2+(LL-ALL)**2)
      DO 1001 I=1,M
      J=M+1-I
      A=FLOAT(2*J-1)*LL/FLOAT(2*M)-ALL
1001  D4(I)=0.5*ALOG(AL**2+A**2)
      NN=N+1
      DO 778 I=1,NN
      J=I-1
      A=FLOAT(J)*L/FLOAT(N)-AL
      A5(I)=(A/2.0)*ALOG(A**2+ALL**2)-A+ALL*ATAN(A/ALL)
778   CONTINUE
      MM=M+1
      DO 779 I=1,MM
      J=I-1
      A=FLOAT(J)*LL/FLOAT(M)-ALL
779   B5(I)=A/2.0*ALOG((L-AL)**2+A**2)-A+(L-AL)*ATAN(A/(L-AL)
      NN=N+1
      DO 780 I=1,NN
      J=NN-I
      A=FLOAT(J)*L/FLOAT(N)-AL
      ZEN1=ATAN=(A/(LL-ALL))
780   C5(I)=A/2.0*ALOG(A**2+(LL-ALL)**2)-A+(LL-ALL)*ZEN1
      MM=M+1
      DO 1002 I=1,MM
      J=MM-I
      A=FLOAT(J)*LL/FLOAT(M)-ALL
1002  D5(I)=A/2*ALOG(AL**2+A**2)-A+AL*ATAN(A/AL)
      DO 889 I=1,N
      J=I+1
889   AA5(I)=A5(J)-A5(I)
      DO 890 I=1,M
      J=I+1
890   BB5(I)=B5(J)-B5(I)
      DO 891 I=1,N
      J=I+1
891   CC5(I)=C5(I)-C5(J)
      DO 1003 I=1,M
```

```
      J=I+1
1003  DD5(I)=D5(I)-D5(J)
      N1=N+M+N+M
      DO892 J=1,N
892   AB(N1+1,J)=AA5(J)
      DO 893 J=1,M
893   AB(N1+1,N+J)=BB5(J)
      DO 894 J=1,N
894   AB(N1+1,N+M+J)=CC5(J)
       DO 1004 J=1,M
1004  AB(N1+1,N+M+N+J)=DD5(J)
      DO 895 I=1,N
895   AB(I,N1+1)=A4(I)
      DO 896 I=1,M
896   AB(N+I,N1+1)=B4(I)
      DO897 I=1,N
 897  AB(N+M+I,N1+1)=C4(I)
      DO 1005 I=1,M
1005  AB(N+M+N+I,N1+1)=D4(I)
      N2=N1+1
      AB(N2,N2)=ALOG(R)
C
C     COMPUTATION OF THE VALUES OF SIGMA AND A
C
      WRITE(6,1)
1      FORMAT('ENTER VALUES FOR GELG IM,IN,IESP')
      IM=2*M+2*N+1
      IN=1
      IESP=1000000
      DO 3 J=1,N2
      DO 4 I=1,N2
      MA(I,J)=AB(I,J)
4     CONTINUE
3     CONTINUE
      WRITE(6,5)
 5    FORMAT('ENTER VALUES OF VECTOR VR')
      N3=N2-1
      DO 9 I=1,N3
9     VR(I)=0.0
      VR(N2)=1.0
      CALL GELG(VR,MA,IM,IN,IESP,IER)
      WRITE(6,7)
7     FORMAT('SOLUTION OF LINEAR EQTS.')
      WRITE(6,8)(VR(I),I=1,IM)
8     FORMAT(' ',1X,8E15.7)
      WRITE(6,25)
25    FORMAT('ENTER NO. OF GRID LINES IN X AND Y  II,JJ,II=JJ
      READ(5,26)II,JJ
26    FORMAT(2I3)
       DX=0.0
      DY=0.0
      DO 444 K1=1,JJ
      DY=LL/FLOAT(JJ)*FLOAT(K1)
```

```
      DO 445 K2=1,II
      E1=0
      DX=L/FLOAT(II)*FLOAT(K2)
      DO 333 J=1,N
      A=FLOAT(J)*L/FLOAT(N)-DX
      B=FLOAT(J-1)*L/FLOAT(N)-DX
      IF(DY.EQ.0.0)GO TO 448
      C=A/2*ALOG(A**2+DY**2)-A-DY*ATAN(A/(-DY))
      D=B/2*ALOG(B**2+DY**2)-B-DY*ATAN(B/(-DY))
      GO TO 409
448   IF(A.EQ.0.0) GO TO 447
      C=A/2*ALOG(A**2)-A
446   IF(B.EQ.0.0) GO TO 449
      D=B/2*ALOG(B**2)-B
      GO TO 409
447   C=0.0
      GO TO 446
449   D=0.0
409   E=VR(J)*(C-D)
333   E1=E1+E
      E2=0
      DO 334 J=1,M
      A=FLOAT(J)*LL/FLOAT(M)-DY
      B=FLOAT(J-1)*LL/FLOAT(M)-DY
      IF((L-DX).EQ.0.0) GO TO 404
      C=A/2*ALOG((L-DX)**2+A**2)-A+(L-DX)*ATAN(A/(L-DX))
      D=B/2*ALOG((L-DX)**2+B**2)-B+(L-DX)*ATAN(B/(L-DX))
      GO TO 408
404   IF(A.EQ.0.0) GO TO 405
      C=A/2*ALOG(A**2)-A
406   IF(B.EQ.0.0) GO TO 407
      D=B/2*ALOG(B**2)-B
      GO TO 408
405   C=0.0
      GO TO 406
407   D=0.0
408   E=VR(N+J)*(C-D)
334   E2=E2+E
      E3=0
      DO 335 J=1,N
      A=FLOAT(N+1-J)*L/FLOAT(N)-DX
      B=FLOAT(N-J)*L/FLOAT(N)-DX
      IF((LL-DY).EQ.0.0) GO TO 503
      C=A/2*ALOG(A**2+(LL-DY)**2)-A+(LL-DY)*ATAN(A/(LL-DY))
      D=B/2*ALOG(B**2+(LL-DY)**2)-B+(LL-DY)*ATAN(B/(LL-DY))
      GO TO 509
503   IF(A.EQ.0.0) GO TO 504
      C=A/2*ALOG(A**2)-A
505   IF(B.EQ.0.0) GO TO 506
      D=B/2*ALOG(B**2)-B
      GO TO 509
504   C=0.0
      GO TO 505
```

```
506   D=0.0
509   E=VR(N+M+J)*(C-D)
335   E3=E3+E
      E4=0.0
      DO 1055 J=1,M
      A=FLOAT(M+1-J)*LL/FLOAT(M)-DY
      B=FLOAT(M-J)*LL/FLOAT(M)-DY
      IF(DX.EQ.0.0) GO TO 1046
      C=A/2*ALOG(DX**2+A**2)-A-DX*ATAN(A/(-DX))
      D=B/2*ALOG(DX**2+B**2)-B-DX*ATAN(B/(-DX))
      GO TO 1045
1046  IF(A.EQ.0.0)GO TO 1047
      C=A/2*ALOG(A**2)-A
1048  IF(B.EQ.0.0) GO TO 1049
      D=B/2*ATAN(B**2)-B
      GO TO 1045
1047  C=0.0
      GO TO 1048
1049  D=0.0
1045  E=VR(N+M+N+J)*(C-D)
1055  E4=E4+E
      E01=E1+E2+E3+E4
      CM(K2,K1)=E01+VR(N2)/2*ALOG((DX-AL)**2+(DY-ALL)**2)
445   CONTINUE
444   CONTINUE
      WRITE(8,2000) ((CM(I,J),I=1,K2),J=1,K1)
2000  FORMAT(E15.7)
      CALL PLOTS
      WRITE(6,646)
646   FORMAT('ENTER VALUES OF XSIZE,YSIZE =L,LL')
      READ(5,647)XSIZE,YSIZE
647   FORMAT(F4.2)
      NC=12
      IOP(1)=1
      IOP(2)=1
      IOP(3)=0
      IOP(4)=0
      IOP(5)=0
      IOP(6)=0
      IOP(7)=1
C      VALUES OF CONTOUR LINES TO BE PLOTTED
      CSET=0.0
      DO 27 I=1,12
      CVAL(I)=CSET+0.05
      CSET=CVAL(I)
27    CONTINUE
      I1I=II
      J1J=JJ
      CALL CONTUR(XSIZE,YSIZE,CM,50,I1I,J1J,CVAL,NC,IOP,VOP)
      CALL PLOT(0.0,0.0,999)
      STOP
      END
```

B30205